SINGLE-MOLECULE SPECTROSCOPIC STUDIES OF THIN-FILM CHEMICAL GRADIENTS

by

DIPAK GIRI

B.S., Tribhuvan University, 2006
M.S., Tribhuvan University, 2010

AN ABSTRACT OF A DISSERTATION

submitted in partial fulfillment of the requirements for the degree

DOCTOR OF PHILOSOPHY

Department of Chemistry
College of Arts and Sciences

KANSAS STATE UNIVERSITY
Manhattan, Kansas

2016

Abstract

This dissertation describes the application of single molecule spectroscopy and tracking to investigations of the nanoscale properties of thin-film chemical gradients and the transport dynamics of molecules dispersed within and upon these gradients. Chemical gradients are surface bound materials that incorporate gradually changing chemical and/or physical properties. A continuous and gradual change in the properties of gradients are expected and often required for their intended applications, which range from directed growth of cell colonies to combinatorial materials science. In reality, such conditions are almost never met due to spontaneous demixing and dewetting processes that can lead to properties variations on microscopic length scales. A better understanding on the properties of chemical gradients on microscopic length scales will aid in the production of better engineered materials.

Single molecule spectroscopy (SMS) allows for gradient properties to be probed on nanometer-to-micrometer length scales. In this dissertation, quantitative measurements of gradient polarity (i.e., dielectric properties) are made along a sol-gel derived thin film that incorporates a macroscopic polarity gradient. These measurements report on the microscopic heterogeneity of the gradient film, and point to the occurrence of phase separation of the polar and nonpolar components along the gradient. Single molecule tracking (SMT) provides an important means to examine the dynamics of molecular mass transport in thin films and on surfaces. In this dissertation, SMT is employed to study mass transport in thin water films condensed over monolayer wettability gradients under ambient environments. The results show that the rate and the mechanism of molecular transport depend on the surface wettability, and on the ambient relative humidity. Finally, wettability gradients have been broadly used to drive the transport of liquid droplets. In this dissertation, these applications are extended to achieve

spontaneous stretching of DNA by the propulsion of liquid droplets along the gradient. Single molecule fluorescence imaging of DNA stretched along these gradients demonstrates that hydrophobic surfaces play an important role in DNA stretching. The study also shows the surface tension force acting at the gradient-droplet contact line (interface) to be responsible for DNA elongation and alignment. Overall, single molecule methods have been shown to be highly useful for better understanding the properties of chemical gradients as described in this dissertation.

SINGLE-MOLECULE SPECTROSCOPIC STUDIES OF THIN-FILM CHEMICAL GRADIENTS

by

DIPAK GIRI

B.S., Tribhuvan University, 2006
M.S., Tribhuvan University, 2010

A DISSERTATION

submitted in partial fulfillment of the requirements for the degree

DOCTOR OF PHILOSOPHY

Department of Chemistry
College of Arts and Sciences

KANSAS STATE UNIVERSITY
Manhattan, Kansas

2016

Approved by:

Major Professor
Dr. Daniel A. Higgins

Copyright

Abstract

This dissertation describes the application of single molecule spectroscopy and tracking to investigations of the nanoscale properties of thin-film chemical gradients and the transport dynamics of molecules dispersed within and upon these gradients. Chemical gradients are surface bound materials that incorporate gradually changing chemical and/or physical properties. A continuous and gradual change in the properties of gradients are expected and often required for their intended applications, which range from directed growth of cell colonies to combinatorial materials science. In reality, such conditions are almost never met due to spontaneous demixing and dewetting processes that can lead to properties variations on microscopic length scales. A better understanding on the properties of chemical gradients on microscopic length scales will aid in the production of better engineered materials.

Single molecule spectroscopy (SMS) allows for gradient properties to be probed on nanometer-to-micrometer length scales. In this dissertation, quantitative measurements of gradient polarity (i.e., dielectric properties) are made along a sol-gel derived thin film that incorporates a macroscopic polarity gradient. These measurements report on the microscopic heterogeneity of the gradient film, and point to the occurrence of phase separation of the polar and nonpolar components along the gradient. Single molecule tracking (SMT) provides an important means to examine the dynamics of molecular mass transport in thin films and on surfaces. In this dissertation, SMT is employed to study mass transport in thin water films condensed over monolayer wettability gradients under ambient environments. The results show that the rate and the mechanism of molecular transport depend on the surface wettability, and on the ambient relative humidity. Finally, wettability gradients have been broadly used to drive the

transport of liquid droplets. In this dissertation, these applications are extended to achieve spontaneous stretching of DNA by the propulsion of liquid droplets along the gradient. Single molecule fluorescence imaging of DNA stretched along these gradients demonstrates that hydrophobic surfaces play an important role in DNA stretching. The study also shows the surface tension force acting at the gradient-droplet contact line (interface) to be responsible for DNA elongation and alignment. Overall, single molecule methods have been shown to be highly useful for better understanding the properties of chemical gradients as described in this dissertation.

Table of Contents

List of Figures

List of Tables

Acknowledgements

First and foremost, I would like to extend my sincere thanks and deep appreciation to my advisor Dr. Daniel Higgins for providing continuous support, constant guidance and endless motivation throughout these past five years at Kansas State University. Dr. Higgins' wide range of knowledge, tireless dedication to scientific research and the willingness to allow freedom in my research efforts have all greatly inspired my graduate career. I feel fortunate to have had the opportunity to work and learn under his mentorship.

I am highly thankful to my co-advisor Dr. Maryanne Collinson (Virginia Commonwealth University) for providing critical analysis and valuable suggestions on my works. The collaboration with the Collinson group has been instrumental in advancing many of my research projects. I would like to express my gratitude to Dr. Takashi Ito, Dr. Christopher Culbertson and Dr. Keith Hohn for their contributions on my supervisory committee. I would like to thank Dr. Vinod Kumarappan to be willing to serve as a chairperson of the final examination committee.

I recognize the support from Ron Jackson, Tobe Eggers and Jim Hodgson in troubleshooting instruments and designing the key accessories required for my research. I would like to thank Dr. Khanh-Hoa Tran-Ba and Dr. Seok Chan Park for their time in important scientific discussions and help in my experiments. I am grateful to the current and past members in the Higgins group: Hao Xu, Zi Li, Zudith Batusta, Ruwandi Kumarasinghe and Kaushalya Perrera. I have enjoyed working alongside them and highly appreciate their collegiality. Thanks to the diligent undergraduate researchers Chelsea Hanks, Josh Austin and Kali Hinman for working with me. I also thank Kayesh Ashraf and present and past members of the Collinson group for the important discussions in our weekly web meeting.

I gratefully acknowledge the support by the U.S. National Science Foundation, and by the U.S. Department of Energy, Division of Chemical Sciences, Geosciences and Biosciences. I would also like to thank Dr. Takashi Ito for access to spectroscopic ellipsometry and Dr. Bruce Law for his help with the contact angle instrument.

Finally, huge thanks go to my family and friends for their continuous support and encouragement during my journey in graduate school. I would like to remember my parents, Jivan and Devi Giri, and my sisters Puja and Ganga Giri. I would like to show a deep appreciation for my wife Rukmini Puri. The experience as a graduate student would not have been that exciting and productive without all of their love, care, patience and support.

Dedication

This work is dedicated to my loving wife Rukmini, my lovely son Robin and especially my proud parents Jivan and Devi.

Acronyms and Definitions

AFM	Atomic force microscopy
APD	Avalanche photodiode
BE	Binding energy
CCD	Charge coupled device
CM	Clausius-Mossotti
CN-silane	Cyanopropyltrichlorosilane
C11OPDI	N,N'-bis(octyloxypropyl)-perylene-3,4,9,10-tetracarboxylic diimide
C8-silane	Octyltrichlorosilane
DCLP	Dichroic long pass filter
F_{in} / F_{out}	Infusion rate / Withdrawal rate
f-PALM	Fluorescence photoactivation localization microscopy
F-silane	Trichloro-[1H,1H,2H,2H-perfluoro-octyl]silane
FTIR	Fourier Transform Infrared
FWHM	Full width at half maximum
IWDC	Infusion-withdrawal dip-coating
MSD	Mean square displacement
NC / PC	Negative control / Positive control
NEXAFS	Near-edge X-ray absorption fine structure spectroscopy
ORMOSIL	Organically modified silicate
PALM	Photoactivated localization microscopy
PSF	Point spread function
PTMOS	Phenyltrimethoxysilane

RH	Relative humidity
SAM	Self-assembled monolayer
SERS	Surface enhanced Raman scattering
SMS	Single molecule spectroscopy
SMT	Single molecule tracking
STED	Stimulated emission depletion microscopy
STORM	Stochastic optical reconstruction microscopy
TIRF	Total internal reflection
VPD	Vapor-phase deposition
TMOS	Tetramethoxysilane
WCA	Water Contact Angles
WI	Water immersion objective

Chapter 1 - General Introduction

1.1 Thin-Film Chemical Gradients

Thin-film chemical gradients are surface bound materials designed to incorporate continuously changing physicochemical properties as a function of position on a substrate.[1-4] The work described in this dissertation focused on obtaining a better understanding of the nanoscale properties of these materials. Gradients can be prepared by using any one of the two general methods: (i) direct deposition and (ii) post-deposition modification. In direct deposition, gradients are prepared typically on a flat substrate by controlled and gradual deposition of the gradient precursors such as monomers, oligomers, and polymers either from solution or from the vapor phase by using any one of a number of deposition techniques. Some of these techniques include, but are not limited to, controlled immersion[5] and infusion,[6] dip coating,[7,8] contact[9] and inkjet[10] printing, electrochemical deposition,[11] vapor phase techniques,[12] and microfluidics[13].

In the case of post-deposition, a flat substrate bearing a pre-coated material (thin film, self-assembled monolayer or SAM) is progressively modified either by chemical (etching)[14] or by physical (irradiation)[15] means in a top down manner. However, the direct deposition with the bottom up approach is currently the most widely employed method of gradient fabrication. Gradient films can be prepared to be either static or dynamic. A static gradient has physicochemical properties that are fixed during its preparation and these properties do not evolve with time. However, in a dynamic gradient, the physicochemical properties change over time. Most of the methods listed above yield only static gradients. Dynamic gradients can be obtained by applying a few methods such as those based on microfluidics and electrochemistry. Chemical gradients can be prepared by using one or more of a large number of chemical precursors including organic polymers, organosilanes and alkanethiols, many of which are

commercially available. Gradients prepared from organosilanes are the focus of this dissertation. The use of organosilanes as precursors allows for the preparation of gradients in one or more of the properties such as polarity,[16] wettability,[12] charge,[17] pH, ligand density,[18] etc. They also allow gradients to be prepared on technologically useful silica substrates.

Each chemical gradient can be described in terms of its many attributes.[2] Three such important attributes are the gradient *directionality*, its *dimensionality* and its *length scale* shown in **Figure 1.1**. A gradient can be prepared so that its properties change in one direction (unidirectional), in perpendicular directions (orthogonal) or in radial directions emanating from the center toward the periphery (**Figure 1.1A**). Unidirectional gradients are the most common. When such gradients incorporate more than one functional component, the properties of the gradient can vary either in parallel (aligned) or in antiparallel (opposed) directions. Gradients can be made in one, two or even three dimensions (**Figure 1.1B**). While an isolated 1D gradient in the form of a line is rarely made, 2D gradients are commonly prepared in the forms of thin films and SAMs. A 2D gradient can be extended into a 3D gradient by a number of methods including a grafting-onto method. In this method, a 2D gradient in polymer density (concentration) is first prepared which is followed by grafting a second end functionalized polymer producing a 3D gradient. The gradient length scale is another important attribute that defines the extent of gradient continuity and smoothness. A gradient which appears to be continuous and smooth on macroscale can be actually discontinuous and discrete at microscale as shown in **Figure 1.1C**. In fact, a gradient is comprised of a collection of many individual samples each having a uniform property. Ideally, the variation in the property between these individual samples is smooth and hence the gradient is continuous. However, in reality there is an abrupt change in property between these individual samples making gradient rather discontinuous at microscopic length

scales. Therefore, examination of gradient properties at microscopic length scales can provide a better understanding of these materials.

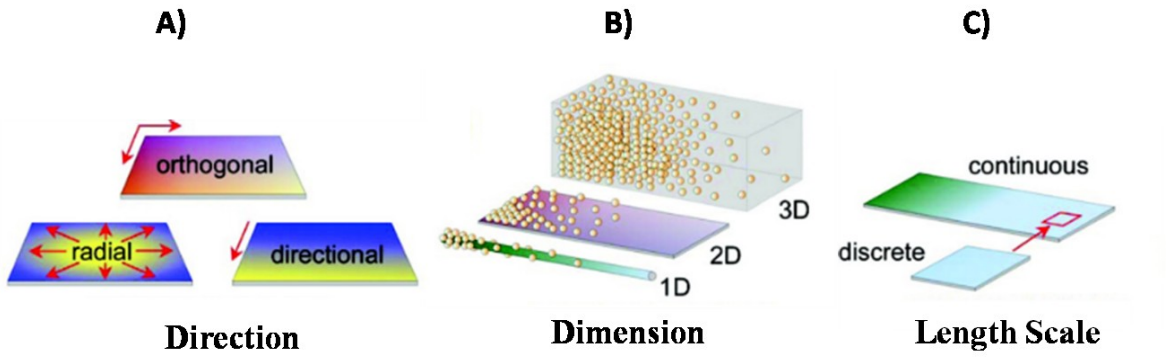

Figure 1.1 Key attributes of chemical gradients. **A)** Direction, **B)** Dimension, **C)** Length scale. Adapted with permission from Ref. (2). Copyright 2008, American Chemical Society.

A number of measurement tools have been employed to characterize the composition and the properties of chemical gradients. The chemical composition of gradient films is generally accessed by using techniques such as XPS, FTIR or Raman-scattering. While XPS[6] provides the elemental composition, FTIR[19] and Raman[20] reveal the chemical functionalities incorporated along the gradient. Water contact angle measurements[12] are useful as a means to follow the macroscopic wettability (surface energy) of the gradient surface. AFM[21] allows for the density of adsorbed species to be mapped along the gradient surface. Electrochemical methods[17] are useful in characterizing gradients incorporating charged and redox species on the surface. Bulk fluorescence spectroscopy has been applied to measure macroscopic polarity[16]. Many of the methods listed above are bulk methods that are useful only when an average property along the gradient surface is sought. Since the gradients are inherently heterogeneous materials, a complete understanding of their properties at the microscopic scale is necessary in order to better design

these materials for different applications. Toward this end, single molecule spectroscopy (SMS) allows for gradient properties to be examined on molecular length scales providing the complete distribution of the materials properties under study. As a result of its utility, SMS studies of gradient properties are emphasized in this dissertation.

1.2 Importance of Thin Film Chemical Gradients

Thin film chemical gradients are important materials due to their significant potential utility in a number of basic and applied studies. Chemical gradients can serve as a combinatorial material library along a single substrate (sample) and can aid in the development, optimization and screening of new materials. For example, Potyrailo et al. have prepared gradient polymer libraries to explore novel materials for sensing applications.[22] Jayaraman et al. have employed gradients in platinum surface coverage as a means for measuring the activity of spatially localized catalysts for elctro-oxidation reactions in an effort to discover new catalysts.[23]

Gradient surfaces are also useful in studies on the adhesion of proteins, cells and vesicles relevant to the development of biocompatible surfaces and to applications in tissue engineering.[24] For example, Harris et al. employed ligand density gradients in cell-adhesive RGD prepared from anionic polymer brushes to control the spatial attachment of fibroblasts.[25] Spencer et al. developed SAM films incorporating orthogonal gradients in charge density and net charge, and examined the adsorption of proteins having negative (bovine serum albumin, fibrinogen) and positive (lysozyme) charges.[26] This study demonstrated that adsorption is influenced mainly by electrostatic interaction and, surprisingly, even the charge-balanced zwitterion was found to adsorb.

Likewise, gradient surfaces can act as surface engines, driving the transport of liquid droplets. Chaudhary and Whitesides[12] initially demonstrated the spontaneous motion of a small droplet of water across a few millimeter distance, along a surface free energy gradient, even when the substrate was inclined at an angle. They reported that a negligible contact-angle hysteresis ($\leq 10^0$) was required to observe droplet motion along the gradient. In a similar manner, gradient surfaces have also been used to direct the motion of nanoparticles,[27,28] macromolecules,[29,30] vesicles,[31] and cells[13,32-34]. Additionally, gradient surfaces have been shown to be useful in difficult chemical separations.[35,36]

1.3 Objective and Motivation of Present Research

The work performed for this dissertation addresses two specific objectives:

I. To better understand the nanoscale polarity (dielectric properties) along organosilane gradients prepared by sol-gel deposition. To this end, quantitative SMS measurements were undertaken and were used to determine the polarity distribution and to reveal the extent of heterogeneity and phase separation as a function of position along the gradients.

II. To better understand surface wettability and the role of condensed water layers in governing molecular mass transport along gradient SAM films prepared by vapor-phase deposition of organosilanes. To this end, single molecule tracking methods were employed to explore the rate and mechanism of probe molecule diffusion on the film surface, as a function of position along the gradient and of relative humidity (RH).

Thin-film chemical gradients are inherently multi-component materials. At the molecular level, each component represents a particular chemical functionality. Gradient properties are determined by the co-operative interactions (*co-operativity*) of chemical functionalities closely

spaced within the dipole-dipole coupling distance. In addition, when a foreign molecule (analyte/reagent) comes in contact with a gradient during its application, one of the gradient components can, preferentially, interact more strongly with the foreign molecule, altering its adsorption or partition compared to those on a single-component and non-gradient thin film. Depending on the local chemical composition, solvent environment, pH and the structure of the foreign molecule, such interactions can represent H-bonding, electrostatic and dipole-dipole interactions, and π-π interactions.

Ideally, gradient components (precursors) are considered to be mixed very well so that a gradient film exhibits continuous and smooth variations in its properties down to the molecular level. In reality, however, a gradient film which appears to have continuous variations in its macroscopic property may still exhibit stepwise (discrete) variations in its nanoscopic properties. These discrete properties variations may be caused by phase separation of the gradient components owing to poor miscibility of certain precursor organosilanes (e.g. polar vs. nonpolar), different rates of their hydrolysis and condensation, and surface dewetting. Phase separation occurs due to a decrease in entropy with the corresponding increase in free energy during the transition of colloidal sols into network gel at constant temperature. In the gaps between the neighboring phase separated domains, there is a smaller chance for co-operative interactions among the gradient components which leads to an abrupt (rather than continuous) change in gradient properties. Phase separation and microscopic heterogeneity limit the utility of gradient films in many applications where gradual properties variations are expected and/or required. Understanding such microscopic to nanoscopic heterogeneity along gradient films can, therefore, lead to improvements in the design of these important materials. The ability to probe the properties of individual nanoscale environments with single molecule sensitivity, and to

follow the motion of individual molecules makes the technique of single molecule spectroscopy (SMS) an ideal tool for nanoscale characterization of gradient films.

Chapter 2 - Preparation and Characterization of Chemical Gradients

2.1 Methods of Gradient Preparation

A myriad of techniques have been employed to prepare thin film chemical gradients. Some of the common techniques employed by different research groups will be discussed here. **Figure 2.1** shows cartoons representing a few of such techniques.

2.1.1 Immersion Based Techniques

Gradient deposition from the solution phase may be accomplished by immersion based techniques. In a commonly used immersion based technique, suitable substrate is gradually exposed to a precursor solution either by slowly immersing the substrate into the solution or by infusing the solution with certain rate (**Figure 2.1A**). A gradual variation in the exposure time of the substrates to the precursor solutions lead to formation of gradients. For example, Spencer et al. used a controlled immersion[5] in order to prepare concentration gradient in methyl- or hydroxyl- terminated alkanethiol. The subsequent immersion of the first gradient into a complimentary thiol solution produced a two-component counter gradient in wettability.[37]A sol-gel dip-coating method called controlled-rate infusion (CRI)[6] was employed by the group of Collinson to produce chemical gradients from aminosilanes on silica substrates. Similarly, the Higgins group has developed a method called infusion-withdrawal dip-coating (IWDC)[16] based on similar sol-gel dip-coating that allows to gradually change the concentration of the organosilanes solutions over time, resulting in gradient deposition. The sol-gel approach used in both the techniques involves hydrolysis of organosilanes with subsequent condensations. The hydrolyzed organosilanes undergo condensation reactions with each other producing low

molecular weight oligomers and/or with the surface silanol groups depositing thin films on the surface. The IWDC method was employed for preparation of polarity gradients[8] described in **Chapter 5** of this dissertation. In IWDC method,[16] a sol of time- varying composition is generated by infusing one sol into the other with simultaneous withdrawal of the mixture sol. The concentrations of the two sols at a time are expressed by the following equations-

$$C(t) = C(t=0)\left(\frac{V_{sol}(t)}{V_{sol}(t=0)}\right)^{\frac{F_{out}}{(F_{out}-F_{in})}} \qquad (2.1)$$

Here $C(t)$ is the concentration of the sol present in dip-coating reservoir at time *t*, $C(t=0)$ is its initial concentration, $V_{sol}(t)$ and $V_{sol}(t=0)$ are sol volumes in the reservoir at time *t* and at the initial respectively, and F_{out} and F_{in} the rates of withdrawal and infusion respectively.

$$C'(t) = C'\frac{F_{in}}{F_{out}}\left(\left(\frac{V_{sol}(t)}{V_{sol}(t=0)}\right)^{\frac{F_{out}}{(F_{out}-F_{in})}}\right) \qquad (2.2)$$

Here $C'(t)$ is the concentration of the sol being infused at time *t* and C' its invariant concentration. The CRI and IWDC methods afford some control over the gradient profiles, although the gradients can be less uniform than vapor deposited ones, due to surface tension gradients, contact line pinning and other factors that arise during dip-coating of liquid sols.

2.1.2 Vapor Diffusion

The formation of wettability gradients by a diffusing vapor front of organochlorosilane dissolved in paraffin oil was first experimentally demonstrated by Whitesides.[12] The experiment can be carried out in simple set up as shown in **Figure 2.1B**. Chaudhury et al. have extensively used this method to study a number of parameters that govern droplet motion along wettability gradients.[38-40] The Genzer group has used this method in preparation of gradients in grafting density and molecular weight of polymer brushes.[18,41,42] This is also one of the techniques employed in this dissertation for making two-component gradients in wettability[43] described in **Chapter 6**. The deposition of organosilanes on silica surface depends on the chemical reactions between the organochlorosilane molecules and the hydroxy groups present on the silica surface. The water adsorbed on silica surface hydrolyzes the organochlorosilanes before they can condense with the surface hydroxy (silanol) groups. The strong siloxane (Si-O-Si) bond formed as a result of condensation attaches organosilane to the silica surface. Parameters[43-45] that affect gradient deposition by this technique are the vapor pressure of the precursor organochlorosilanes, the humidity in the deposition environment, the separation between the substrate and the silane reservoir, and the exposure time etc. Monolayer gradients obtained by this technique are more uniform and stable than alternatives prepared by solution phase methods, but it is hard to control the gradient profile or steepness.

2.1.3 Contact Printing

The contact printing technique initially developed by the Whitesides group[46] has been widely used for generating gradient SAMs. In this technique, an elastomeric stamp is first soaked with chemical (ink) and brought in contact with the surface to be printed. Choi et al. found a method to generate a gradient by varying the contact time between a silicone stamp containing

octadecyltrichlorosilane (OTS) and silicon.[47] A longer contact time printed more OTS and a gradient in OTS concentration was formed. This method affords the gradient length to be tuned from adjustments in the radius and the shape of the silicone stamp. Kraus et al. produced a chemical gradient by a method of mass-transfer microcontact printing (μCP) in which the amount of ink transported to the substrate is controlled by the thickness of the stamp as shown in **Figure 2.1C**.[9] They showed reaction-limited flux (ψ) of the ink to the surface is given by following equation-

$$\psi = S_o(1-\varepsilon)^2 \frac{h}{D}\sqrt{\frac{K_B T}{2\pi m}} \qquad (2.3)$$

Here, S_o is the initial sticking probability of ink to surface, ε is fraction of surface covered, h is stamp thickness, K_B is Boltzmann constant, T is temperature and m the mass of molecule. By using wedge-shaped PDMS stamp of varying thickness, they printed hexadecnethiol (HDT) density gradients on a gold surface. The μCP methods allow producing gradients on micrometer length scales but are limited to mostly the planar surfaces.

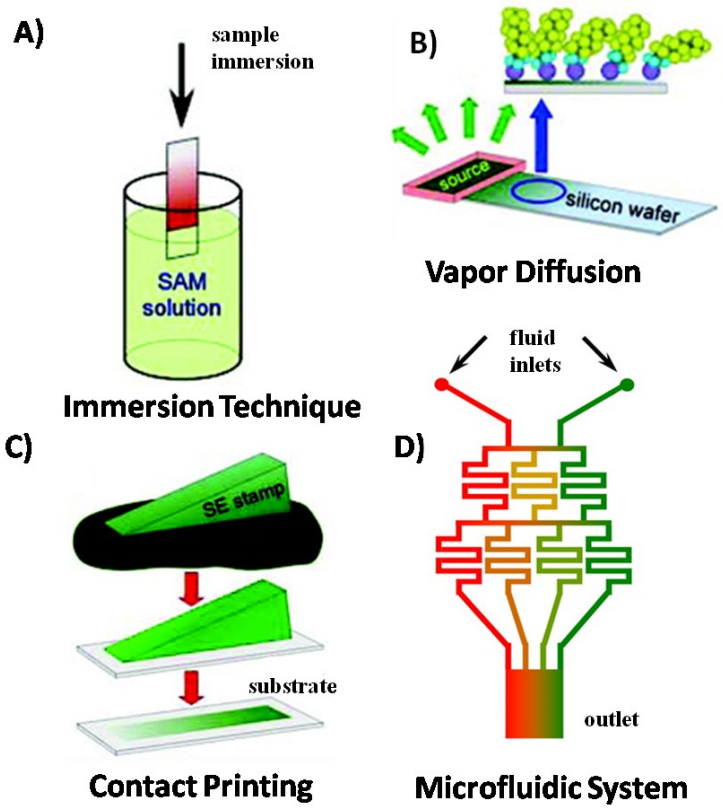

Figure 2.1 Different techniques for preparation of chemical gradients. **A)** Immersion technique, **B)** Vapor diffusion, **C)** Contact printing, and **D)** Microfluidic system. Adapted with permission from Ref. (2). Copyright 2008, American Chemical Society.

2.1.4 Microfluidic System

Microfluidic system offers a versatile way of creating chemical gradients by controlling the flow of individual solutions into a network of microchannels as shown in **Figure 2.1D**.[48] The individual solutions are split, mixed and recombined as they travel down the network. A gradient is established perpendicular to the flow direction across an outlet channel which collects all the branches of the network. The gradient in solution is then deposited on the surface. Gunawan et al. have used microfluidics to generate counter gradients of proteins laminin and collagen I on SAM coated gold substrate in order to study cell behavior in different protein environments[49].

Similarly, Shi et al. produced gradients in polydopamine on hydrophobic surface by employing microfluidic system.[50] They used this gradient to enable spatial deposition of the adhesive proteins and to control the adhesion of mesenchymal stem cells. One advantage of this system is that it allows making dynamic gradient by simply changing the flow velocity of the input solutions.

2.1.5 Electrochemical Method

Electrochemical methods of gradient generation involve either purely electrochemistry or a combination of electrochemistry along with immersion or irradiation. Purely electrochemical gradients can be obtained by applying a potential in a gradient fashion. For example, Bohn et al. created octanethiol gradients on gold substrates by the reductive desorption of thiol by using an in-plane potential gradient.[51] The octanethiol gradient was further backfilled with 3-mercpatopropionic acid to obtain a two-component gradient in surface energy. In an another experiment, by Yamada et al., a dynamically controlled wettability gradient was prepared by applying an in-plane potential gradient to an electrode modified with a redox-active monolayer of ferrocenyl alkanethiol.[52]Electrochemical methods provide a valuable means to prepare dynamic gradients on surfaces and also allow for the switching of gradient properties.

2.1.6 UV Irradiation

Modulation of the exposure of photosensitive films to UV light has offered an important means of fabricating gradients. In one method employed by Amis et al., surface energy gradients were prepared by exposing SAM films deposited from n-octyldimethychlorosilane vapor, to UV

light of varied exposure along the film.[53] In this approach, as the duration of UV exposure increases, the film gets increasingly hydrophilic due to oxidation (ozonolysis) of the hydrocarbon chain. In an another method, Roberson et al. exposed a chlorosilane SAM on silicon to a gradient intensity of UV-ozone radiation with the help of a variable density filter to make surface energy gradient.[54] Similar exposure to a gradient UV-light was applied for converting films prepared from a photosensitive polymer brush[55] and proteins[56] into gradients in polymer composition and thickness, and in protein concentration respectively.

2.2 Common Techniques of Gradient Characterization

2.2.1 Water Contact Angle (WCA) Measurements

Measurement of water contact angles represents the most straightforward approach to determining the surface wettability (free energy) along a gradient. The contact angle of a liquid represents the angle formed by a droplet at the three-phase boundary where liquid, gas and solid intersect. The contact angle of a drop of water (θ_w) on an ideally flat surface is determined by the thermodynamic equilibrium existing at three interfaces as described by Young's equation-

$$\gamma_{lv} Cos\theta_w = \gamma_{sv} - \gamma_{sl} \quad (2.4)$$

Whereγ_{lv}, γ_{sv} and γ_{sl} represent the liquid-vapor, solid-vapor, and solid-liquid interfacial tensions or energies respectively. According to **equation 2.4**, when the energy of the solid-vapor interface (γ_{sv}) is higher than that of the liquid-vapor interface (γ_{lv}) or the surface tension of the liquid, the solid surface gets completely wet by the liquid. Otherwise, the liquid only, partially,

wets the solid surface. Young's equation allows to calculate only one contact angle- the static or equilibrium contact angle for a surface. But in practice a range of contact angles are possible for a surface due to its roughness or heterogeneity. In such case both the advancing and receding contact angles can be measured by increasing and decreasing the droplet volume respectively. The difference between the two angles is called contact angle hysteresis.

WCA measurements have been widely used to access the macroscopic wetting property of a number of gradient surfaces which differ in the range of their wettability.[5,57] Wettability gradient can cause spontaneous motion of small droplet of water. However, such ability is decreased due to the presence of contact angle hysteresis. Whitesides et al. showed that the contact angle hysteresis of less than 10^o is required to observe the spontaneous motion of a water droplet along a wettability gradient.[12] Daniel et al. have applied external vibration to overcome the effect of contact angle hysteresis in droplet motion.[58] Although useful, this method can provide information only on the macroscopic properties of gradient surfaces and the measured contact angles data require adjustments for the effect of surface roughness.

2.2.2 X-ray Photoelectron Spectroscopy (XPS)

X-ray photoelectron spectroscopy (XPS) is an important surface analysis technique that provides information on chemical composition of the surface. In this technique, a surface is irradiated with X-rays of sufficient energy in order to eject core shell electron as a result of photoelectric effect. The kinetic energy (E_k) of the ejected electron is measured, and it depends upon the binding energy (E_b) of the electron and the energy of the X-ray irradiation beam ($h\upsilon$).

$$E_b = h\upsilon - E_k - \phi_{spec} \tag{2.5}$$

Here ϕ_{spec} is the work function of the spectrometer. The binding energy can therefore be calculated by using **equation 2.5** from the known values of the energy of the X-rays and the work function of the spectrometer. The binding energies (B.E) are unique for electrons residing in the particular orbital of a specific element. This enables to identify the chemical composition of the surface by comparing the measured binding energies with the reference values. The intensity of the XPS signal directly correlates to the amount of atoms present on the surface. Moreover, an atom can undergo a characteristic shift in its binding energy depending upon its chemical environment which allows to obtain detailed information on surface chemistry.

XPS has been widely used to examine the chemical composition and/or concentration along gradient surfaces. For example, Spencer and co-workers employed XPS to study chemical gradients prepared by controlled immersion of gold into solutions of either alkanethiols or their derivatives.[37,59,60] In one of such studies, XPS validated the presence of a composition gradient in methyl and carboxy groups and also determined the states of protonation and deprotonation of the carboxy group from the chemical shift in the binding energy of the carboxylic carbon (C 1s B.E ~ 289.7 eV).[37] Kannan et al. have applied XPS in order to first confirm the gradient deposition of aminosilane on silica and then to determine their profiles (steepness) while prepared by CRI method with various rates of infusion.[6] The XPS data acquired along the substrate for N 1s (399.2 eV) and Si 2p (102.9 eV) B.E showed unidirectional concentration gradients in amine groups present on silica surface. The XPS measurements further revealed the ability of CRI method in programming gradient profile at predefined positions. Recently, Ashraf et al.[61] have used XPS to examine the cooperative effects in bifunctionalized charge gradients derived from aminosilane and mercaptosilane. The results of this study showed that the extent of

amine protonation (N 1s B.E for NH_3^+ ~ 401 eV) depends on the local concentration of the sulfonate groups (S 2p B.E for SO_3^- ~168.5 eV) that were obtained after oxidation of the mercapto groups (S 2p B.E for SH ~163.5 eV), and of the surface hydroxyl groups from the silica substrate.

Although a highly surface sensitive technique, the XPS signal represents an average signal from a number of atoms. The technique requires ultra-high vacuum, the long acquisition time and can cause sample degradation.

2.2.3 FTIR and Raman Spectroscopy

FTIR and Raman scattering are vibrational spectroscopies that can be used to map the chemical functionalities in/on gradient materials. Harris et al. have used FTIR to validate the formation of gradient obtained by photopolymerization of surface attached poly(methyl methacrylate) (PMMA).[55] An increase in the IR absorption signal for the carbonyl (C=O) stretch at 1730 cm^{-1} across the surface indicated the presence of a PMMA gradient. FTIR was also employed by Cui et al. to probe the composition along a thin film gradient prepared from tetramethoxysilane (TMOS) and methyltrimethoxysilane (MTMOS) using the IWDC method.[19] The FTIR results depicted a continuous increase in Si-CH_3 absorption at 1275 cm^{-1} confirming a gradient in methyl groups. Moreover, a polarization modulated FTIR was used to demonstrate the conformational order of monolayer gradients by Spencer et al.[37] In this study, a comparison of the IR data lead to the conclusion that a monolayer gradient of methyl groups on a gold had lower conformational order compared to monolayer methyl-hydroxy and methyl-carboxyl counter gradients. In a different study, chemical composition along electrochemically generated gradients were mapped by Bohn et al. by using surface-enhanced Raman spectroscopy (SERS).[20]

The Raman scattering data revealed the existence of a one-component and an opposed two-component gradients prepared on gold from naphthalenethiol alone and along with chlorobenzenemethanethiol, respectively. Although very useful in determining the chemical functional groups, both FTIR and Raman scattering are ensemble techniques, and do not provide direct information on the molecular scale properties of the gradient films.

2.2.4 Fluorescence Spectroscopy

Fluorescence spectroscopy is a highly sensitive analytical technique. The electronic excitation of certain organic fluorophores with light (photons) of appropriate energy results in the subsequent emission of light with lower energy called fluorescence. Bulk fluorescence measurements can provide information on the average properties and dynamics associated with a range of materials including thin films. Crucial to such measurement is the choice of appropriate fluorophores. A wide range of fluorophores are now commercially available which are sensitive to the polarity, pH, and charge of the environment, as well as the presence of certain metals ions.

Fluorescence spectroscopy has been widely used to characterize a number of sol-gel derived materials including the organically modified silicates (ORMOSILS).[62-66] Zink et al. used fluorescence spectroscopy, for the first time, to monitor the chemical evolution *in situ* during thin film deposition of sol-gel derived silica by using pyranine (8-hydroxy-1,3,6-trisulfonated pyrene), which is sensitive to alcohol/water ratio, as a probe molecule.[67] A number of fluorescence studies have since examined the polarity and pH of the relatively dry and solvent filled porous environments within ORMOSIL materials, as well as the molecular mobility within these materials. The Brennan group measured fluorescence from solvatochromic dyes 7AI (7-azaindole) and PRODAN [6-Propionyl-2 dimethylamino(naphthalene)] doped in ORMOSIL

monoliths prepared by mixing tetraethoxysilane (TEOS) sols with sols of either methyltriethoxysilane (MTES) or dimethyldimethoxysilane (DMDMS).[64] In this study, the material polarity was found to be dependent on the solvent composition up to 7 days after its preparation, but on the organic functional groups covalently attached to the silica matrix afterwards, due to the loss of solvent. Interestingly, materials that incorporated more than 20% MTES or 5% DMDMS were found to undergo phase separations. Based on several other studies, the mobility of the dopant (dye, enzyme, protein, polymer) entrapped within the sol-gel matrix was found depend upon factors such as dopant-matrix interactions, the porosity of the material, and its organic content. Small dye molecules were found to be more mobile as the percent of organic moiety increased in ORMOSIL materials.

Bulk fluorescence measurements can also be extended to characterize thin film gradient materials. The Higgins group has previously acquired bulk fluorescence spectra of the polarity sensitive dye Nile Red along a thin film, prepared from tetramethoxysilane (TMOS) and methyltrimethoxysilane (MTMOS) by using IWDC, in order to confirm the presence of a polarity gradient.[16]Although very useful for macroscopic characterization, ensemble fluorescence spectroscopy provides relatively little information on either the nanoscale properties of the sol-gel materials or on material heterogeneity.

Chapter 3 - Single Molecule Methods

Single molecule (SM) methods allow for individual molecules to be detected, observed and followed. Observation at the single molecule level represents the fundamental concentration limit to analyte detection, and provides access to the complete statistical distribution of the parameter under study. Such information is not generally accessible by ensemble methods.

3.1 Importance of Single Molecule Studies

In physical sciences, measurements are often made on an ensemble of particles (atoms, molecules, functional groups) where the number of the particles is expressed in terms of the Avogadro's number (6.022×10^{23}). Such measurements, when undertaken by bulk techniques, provide only the average value of the parameter under study and little information on its true distribution. Understanding the distribution of the values taken on by the parameter becomes particularly important when the particles in the ensemble behave differently with respect to each other. In that case, the average value reported by the bulk techniques rarely represents the true value of the parameter. The realization has long driven the search for methods that can measure (examine) one particle at a time and thus can provide the full distribution of the measured parameter. Towards this end, single molecule spectroscopy (SMS) has succeeded in exploring the behaviors of individual molecules in the complex local environments of a broad range of materials.

Ensemble measurements that provide the average value of an experimental parameter still have great value, especially when relatively homogenous materials are under investigation.

However, in practice, even materials that are expected to be homogeneous, such as polymers and glasses, are often found to be heterogeneous on certain length scales. Single molecule spectroscopy has many distinct advantages over ensemble methods for the study of such materials. First, it completely removes ensemble averaging and allows for the actual distribution of values for the experimental parameter to be constructed. Undoubtedly, the distribution of parameters provides more information compared to a single average value. A close examination of the distribution profile for the presence of multiple peaks and/or changes in its shape often reflect the presence of multiple domains and/or rare behavior of the molecules in the materials. Second, the probe molecule used in single molecule studies can be chosen to be sensitive to a particular material property such as polarity, pH, charge or viscosity, and hence SMS provides an important means to measure the properties of nanoscale environments in a range of materials. Third, the direct observation of single molecule motion by SMT allows for the rate and mechanism of such motion to be quantitatively explored. From these two parameters, important new information can be gleaned as to the viscosity and rigidity of the microscopic environment of the materials, the presence of specific molecule-matrix interactions, and even the structure of the nanoscale materials.

3.2 General Background and Theory

The detection of single organic chromophores (i.e., single molecules) was reported for the first time separately by Moerner and Orrit in experiments performed under cryogenic temperatures. In 1987, Moerner et al.[68] detected the absorption of single pentacene molecules in p-terphenyl. Later in 1990, Orrit et al.[69] detected the fluorescence from the same system. In 1993, Betzig et al.[70] carried out the first single molecule experiment at room temperature by using near-

field optical microscopy. Over the past three decades room temperature single molecule spectroscopy has expanded significantly with respect to the materials being explored and the experimental techniques now available.

In a typical SM experiment, the material under study is doped with a nanomolar or sub-nanomolar concentration of certain organic dye molecules called fluorophores. The fluorophores are optically detected by exciting their fluorescence. The fluorescence process can be described with the help of a Jablonski diagram, as shown in **Figure 3.1**. The phenomenon starts with the excitation of the molecule from the electronic ground state to any one of the excited vibrational states within the first excited electronic state of the molecule. Excitation occurs in about 10^{-15} sec. The excitation is brought about by the use of suitable laser light having a photon energy equal to the energy difference between the ground and the excited states of the molecule. Once in the excited vibrational state, the molecule subsequently relaxes to the ground vibrational state of the first excited electronic state via non-radiative decay. This process is also fast occurring in about 10^{-12} sec. Fluorescence occurs when the molecule later relaxes to the ground electronic state by the emission of a photon that is usually red shifted (lower energy) with respect to the excitation photon. This allows for the fluorescence to be spectrally separated from the excitation source. Fluorescence is relatively slow, occurring on a 10^{-9} sec time scale.

Detection of fluorescence is carried out by using highly sensitive detectors such as avalanche photodiodes (APDs) or charge coupled device (CCD) cameras. A high magnification, high numerical aperture objective lens helps to both illuminate the sample and to collect the emitted photons. Such lens is required to collect as many number of emitted photons as possible. The collection efficiency of an objective lens for the emitted photons directly correlates with its

numerical aperture. A number of optics such as filters, dichroic and reflecting mirrors and polarizers are also employed in collecting and isolating the excitation and emitted light.

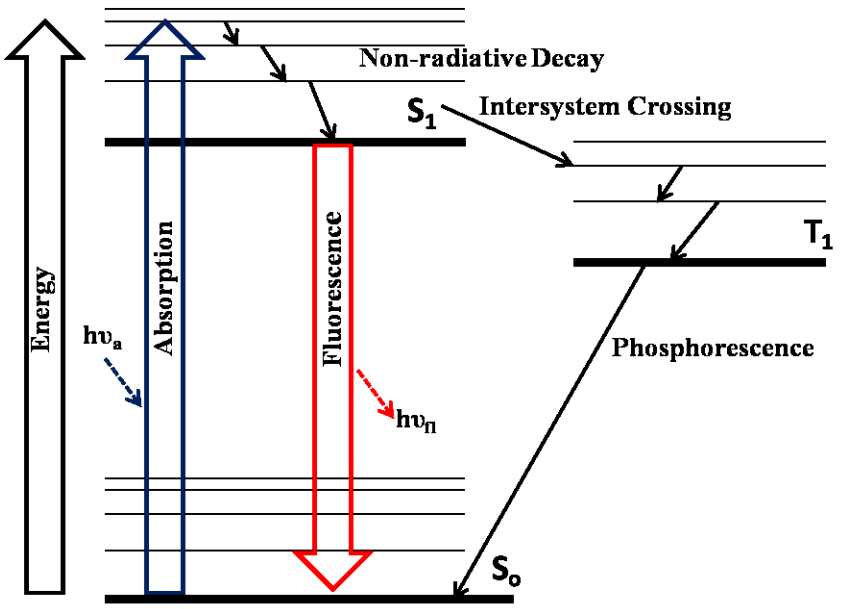

Figure 3.1 Jablonski diagram showing the principle of fluorescence. S_o - ground singlet state, S_1 first excited singlet state, T_1 - triplet state.

3.3 Experimental Techniques for SMS

A number of optical microscopy techniques have been implemented in single molecule spectroscopic experiments. These include near-field optical microscopy, confocal microscopy, and wide field fluorescence microscopy. Wide field microscopy was almost exclusively employed in the work performed for this dissertation. This is one of the most common techniques currently used to observe single molecule fluorescence. As the name implies, the sample is broadly illuminated (a region several microns in diameter) by focusing laser on the back aperture of the microscope objective. Several molecules are then simultaneously detected

through fluorescence. Wide field fluorescence imaging methods can be further implemented either in the epi-illumination or the total internal reflection modes.

3.3.1 Epi-illumination Microscopy

Figure 3.2a shows a basic set up for wide field microscope in epi-illumination mode. In this set up, the input laser beam is reflected off of a dichroic mirror so as to focus on the back aperture of the microscope objective. The fluorescence is collected by passing first through the same microscope objective and then through the dichroic mirror. The residual excitation light is separated from the fluorescence by passing through an appropriate filter. The fluorescence is finally detected by an array detector such as CCD camera. For all SMS experiments, the signal-to-noise ratio is an important parameter. One way of improving this parameter is to use a high numerical aperture (NA) microscope objective to ensure the maximum collection of emitted fluorescence. $NA = n \times \sin\theta_{max}$ depends on the refractive index (n) of the medium between the objective and the sample and on the maximum collection angle (θ_{max}) of the objective. In most of the SMS experiments, the medium is an oil (n=1.51) and an oil immersion objective is used with NA as high as 1.49. Epifluorescence microscopy is useful when the samples under study are very thin, such as thin films and monolayers where the background fluorescence is relatively small.

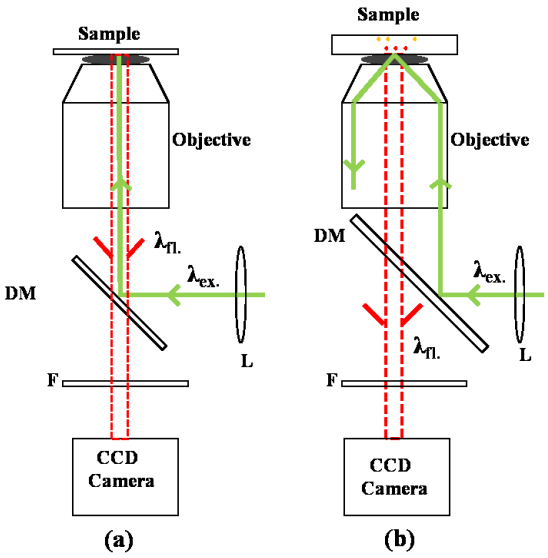

Figure 3.2 Wide field microscopy in (**a**) epi-illumination and (**b**) total internal reflection (TIRF) geometry. DM- dichroic mirror, F- filter, L-lens, $\lambda_{ex.}$ - excitation light, $\lambda_{fl.}$ - fluorescence.

3.3.2 Total Internal Reflection Fluorescence (TIRF) Microscopy

TIRF microscopy is a popular method for examining the molecules on surfaces and at interfaces in thick samples as it provides a means to minimize the background fluorescence and scattering. **Figure 3.2b** depicts a simple diagram of a wide field microscope operated in TIRF mode. This mode is achieved when the excitation laser light emerging from the microscope objective is incident at the sample surface at an angle (θ) greater than the critical angle (θ_c) so that it is totally internally reflected.

$$\theta_c = \arcsin\left(\frac{n_2}{n_1}\right) \qquad (3.1)$$

Here, $n_1$is the refractive index of the sample/substrate and n_2 that of the medium in contact with the sample (air or liquid) and $n_1 > n_2$. This produces an evanescent field that decays exponentially away from the interface.

$$I_z = I_o \times \exp\left(-\frac{z}{d}\right) \qquad (3.2)$$

Here, I_o is the intensity right at the interface at $z = 0$, and I_z is the intensity at distance z away from the interface. The parameter *d* refers to the distance from the interface at which the intensity of evanescent field decreases to $1/e$ or 37% of I_o and is also called the penetration depth and is given by-

$$d = \frac{\lambda}{4\pi\sqrt{n_1^2 sin^2\theta - n_2^2}} \qquad (3.3)$$

Here, λ is the wavelength of the excitation laser. The value of *d* ranges between 100-200 nm depending on the wavelength and refractive indexes. This means that only the molecules close to the interface will be effectively excited and hence will contribute more in the detected fluorescence. TIRF microscopy has proven very useful in the study of interfacial phenomena such as adsorption and desorption with effective elimination of the background light.

3.4 Super-Localization of Single-Molecule Emitter

A fundamental limitation on the resolution of far field microscopes for imaging with visible light is imposed by diffraction as light enters the microscope objective. This limits the

lateral resolution (r) in the x- and y-directions of the image plane to about half the wavelength (λ) of the light emitted by the molecule.

$$r = \frac{\lambda}{2NA} \qquad (3.4)$$

Here, NA is the numerical aperture of the objective currently found in the range of 1.3-1.5 for very good objectives. Resolution is commonly defined as the minimum separation between two sources of light required to fully distinguish (resolve) them from one another. It also represents the diffraction-limited radial dimension for a point source of light imaged in the microscope. For a very tiny molecule (1-2 nm size), emitting at 510 nm, and being imaged with a 1.4 NA objective, the resolution becomes ~ 182 nm. The molecule appears as diffraction limited spot of fluorescence of this size when detected with a CCD camera. This spot represents the point spread function (PSF) of the objective, which produces an Airy pattern for the distribution of the intensity. Thus two molecules separated by a distance < 182 nm would appear as a single blob of light and could not be further resolved.

Beating the diffraction limited resolution of the imaging system has long been a goal of many optical imaging research programs. Single molecule spectroscopy is one method that has allowed for this limit on resolution to be surpassed, and has already paved the way toward development of super-resolution fluorescence microscopy. The effort has been recognized by the 2014 Nobel Prize in Chemistry. Today, super-resolution single molecule microscopy represents a collection of techniques having different abbreviations such as STED,[71] PALM,[72] f-PALM,[73] STORM[74] etc. all of them allowing a spatial resolution far below that of the diffraction limit to be obtained, although each employs different method for achieving super-resolution.

One common approach for super-resolution imaging is to precisely and accurately localize the shape (PSF) of the single-molecule emitter. This involves fitting the intensity distribution of the diffraction limited fluorescent image of the molecule approximately to a 2D-Gaussian function.

$$I(x,y) = I_o exp\left[-\left(\frac{(x-x_o)^2}{2\sigma_x^2} + \frac{(y-y_o)^2}{2\sigma_y^2}\right)\right] \qquad (3.5)$$

Here I_o is the peak intensity (amplitude) of the fitting, x_o, y_o are the central x-, and y-positions of the fit, and σ_x and σ_y are the standard deviations in x- and y-positions. The position (x_o, y_o) provides the precise localization of the single-molecule emitter, while the amplitude itself provides the peak intensity of the fluorescence. Among a number of factors, the number of photons detected (*N*) mostly determines the localization precision (σ) as shown by following equation-

$$\sigma \approx \frac{r}{\sqrt{N}} \qquad (3.6)$$

Thus, in the above example, for 100 photons detected (*N*=100), the localization precision becomes ~ 18 nm or ten times better than expected from the diffraction-limited resolution. This represents super-localization, which is beyond the limit of diffraction. The super-localization of individual fluorophores doped in thin film materials allows for the local or nanoscale properties of the materials to be probed using single molecule methods.

3.5 Single Molecule (Particle) Tracking

A distinct advantage of the super-localization of single molecules is the ability to track the motion of individual molecules with high resolution, which allows for molecular mass transport to be studied in real time. In single molecule tracking (SMT), videos of single molecule motion are recorded at certain frame rates usually using wide field fluorescence microscope. Then, each molecule is super-localized in its position in all of the frames in which it appears prior to photobleaching. By linking these positions frame by frame, individual molecular trajectories are produced. For a lower particle density (sparsely isolated population), such linking can be carried out by a simple separation-based criterion such as the nearest neighbor distance. For this, the distances between the position of a molecule in a particular frame and the positions of all the molecules in the consecutive frame are calculated. The pairs of positions showing the smallest distance are regarded as the most likely occurrence of the same molecule in successive frames, and the positions in the corresponding frames are linked.

The most common approach for further analysis of molecular trajectories involves calculation of the mean square displacement (MSD), which describes the average of the squares of the frame-to-frame displacements (step sizes) for all time lags (t) of certain duration within the trajectory. The dependence of the MSD on t determines the type of motion the molecule exhibits. For example, a linear variation of MSD with t indicates a Brownian motion in 2D.

$$\mathrm{MSD} = 4Dt \qquad (3.7)$$

Here, D represents the diffusion coefficient. A nonlinear variation of MSD with t, however, indicates a motion different from the Brownian motion. The value of D can further be

correlated to the viscosity (rigidity) of the local molecular environment via the Stokes-Einstein equation. Despite the importance of SMT techniques to study molecular mass transport, the quantitative interpretation of the data acquired from an SMT experiment is often tricky and sometimes challenging. A number of artifacts can be introduced due to fluorescence blinking, photobleaching, missed localization, high particle density, localization error as a result of low SNR, poor statistics in short trajectories, and transitions between different types of motion within the same trajectory. These artifacts can, however, be eliminated or minimized through the use of dedicated tools for detection and analysis.

3.6 Application of SMS to Thin-Film Chemical Gradients

Thin film chemical gradients are inherently heterogeneous materials due to the presence of two or more different chemical components. SMS techniques are well suited to studies of such materials and as means to uncover their nanoscale heterogeneity. In the past, the Higgins group has extensively employed SMS techniques to characterize the properties and dynamics associated with non-gradient thin film materials derived from sol-gel deposition. Their studies have focused on quantitatively measuring the polarity[75] and pH[76] properties of individual nanoscale environments within sol-gel derived organically modified silicate (ORMOSIL) films. To probe these properties by SMS methods, the ORMOSIL films were separately doped with nanomolar concentrations of the polarity sensitive dye Nile Red and the pH sensitive dye C-SNARF-1. The results of these studies have provided important insights on the local heterogeneity of the material properties, and the extent of phase separation between inorganic and organic rich domains. The same group also studied molecular diffusion in sol-gel derived mesoporous silica films[77] by using fluorescence correlation spectroscopy, and on a silica film

polarity gradient[19] by using SMT. In both the materials, the rates of molecular diffusion were higher compared to those in the inorganic silicate films, indicating a less viscous liquid-like environments in the ORMOSIL films produced as a result of organic modification.

Work for this dissertation was undertaken in part to extend the application of SMS techniques to characterization of thin film gradient materials. The benefits of applying SMS techniques to gradient materials are two-fold. First, the SMS technique allows for the nanoscale material properties and mass transport dynamics to be explored. Second, chemical gradients facilitate the study of materials properties for samples of different chemical compositions by combinatorial methods. The properties of materials having various chemical compositions can be investigated using a single sample, thus avoiding the tedious steps of preparing multiple samples. In this dissertation, one study is focused on determining the variation in nanoscale polarity (dielectric) properties, and on exploring the phase separation and cooperative effects between two different chemical compositions along a sol-gel derived thin film gradient in polarity. In another study, the effects of surface wettability and the relative humidity of the ambient environment on the molecular diffusion is carried out in a combinatorial manner. In the third study, the spontaneous motion of water droplet along wettability gradients was shown to be useful in molecular combing of DNA molecules, and the effect of the gradient wettability on DNA stretching was studied.

Chapter 4 - Experimental Considerations

4.1 Preparation of Samples

4.1.1 Silica Base Layer

Thin film gradients from organosilane precursors were found to best adhere to the glass and silicon substrates when deposited on a silica base layer. This base layer also affords similar surface chemistries on both substrates, helping to ensure the gradients obtained are of similar nature. Therefore, silica base layers were employed in all the experiments carried out under this dissertation.

The base layer was prepared by spin casting a sol derived from tetramethoxysilane (TMOS) onto silica and silicon substrates. TMOS (99%) was obtained from Sigma-Aldrich and was used as received. The amount of TMOS was varied to get different thicknesses of the base layer. For one study presented in **Chapter 5**, the TMOS sol was prepared by mixing TMOS, ethanol (200 proof), deionized water, and 0.1M HCl in mole ratios of 1.0:31.5:5.5:0.01 (TMOS:ethanol:H_2O:HCl) while for other studies presented in **Chapter 6** and **Chapter 7**, the mole ratios were changed to 1:125.8:22.1:0.04. In all studies, the sol was stirred for 1 h after initial mixing and was subsequently aged in a desiccator for 23 h prior to use.

Glass coverslips (FisherFinest Premium, 25 mm x 25 mm) or cut pieces (25 mm X 25 mm) of silicon wafers (University Wafer, 500 μm thickness) were employed as substrates. The glass substrate was used for characterizations that involve fluorescence studies and water contact angle measurements. The silicon substrate was used for characterizations by spectroscopic ellipsometry and by atomic force microscopy (AFM). Prior to use, each substrate was cleaned by exposure to an air plasma for 5 min. A 150 uL aliquot of a TMOS sol prepared as described

above was then spin coated (5000 rpm, 30s) onto the glass coverslip or silicon wafer. Base layer films obtained by this procedure were uniform. The base layers were desiccated for at least overnight (but not longer than two weeks) before use for gradient deposition.

4.1.2 Thin Film Polarity Gradients

All thin film polarity gradients were prepared by exposing the base layer coated-substrate to a sol of time varying composition. These sols were obtained by simultaneously mixing two separate sols while withdrawing the excess sol in a method called infusion-withdrawal dip-coating (IWDC). For **Chapter 5** the two sols were derived from nonpolar phenyltrimethoxysilane (PTMOS) and polar TMOS. Each sol was prepared using a two-step acid/base hydrolysis and condensation process. PTMOS (97%, Sigma-Aldrich) was used as received. PTMOS sols were prepared in silane:ethanol:H_2O:HCl(0.1M):NH_3(1M) mole ratios of 1.0:60.9:10.2:0.01:0.07 while TMOS sols were prepared with similar mole ratios of 1.0:59.0:9.8:0.01:0.07.

Sols were prepared by first mixing the silane, ethanol and acid. The TMOS and PTMOS sols were then stirred for 5 min and 10 min, respectively. Base (NH_3) was subsequently added to both sols. For characterization by single-molecule spectroscopy, a sufficient amount of solvatochromic Nile Red dye (**Figure 4.1**) in ethanolic solution was also added at this point so that its final concentration in both the sols was 1.0 nM. After addition of the base and dye, the sols were again stirred for 35 and 30 min, respectively, to bring the total stirring time in each case to 40 min. The TMOS and PTMOS sols were then aged for 1.5 h and 4 h, respectively, in a desiccator, prior to use.

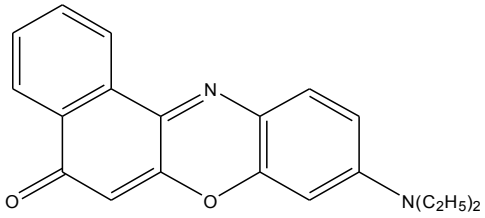

Figure 4.1 Chemical structure of 9-diethylamino-5H-benzo[alpha]phenoxazine-5-one (Nile Red).

4.1.3 Infusion-Withdrawal Dip-Coating (IWDC)

Infusion-Withdrawal Dip-Coating (IWDC) was performed in a specially designed glass reservoir. A diagram of the setup is given in **Figure 4.2a**.

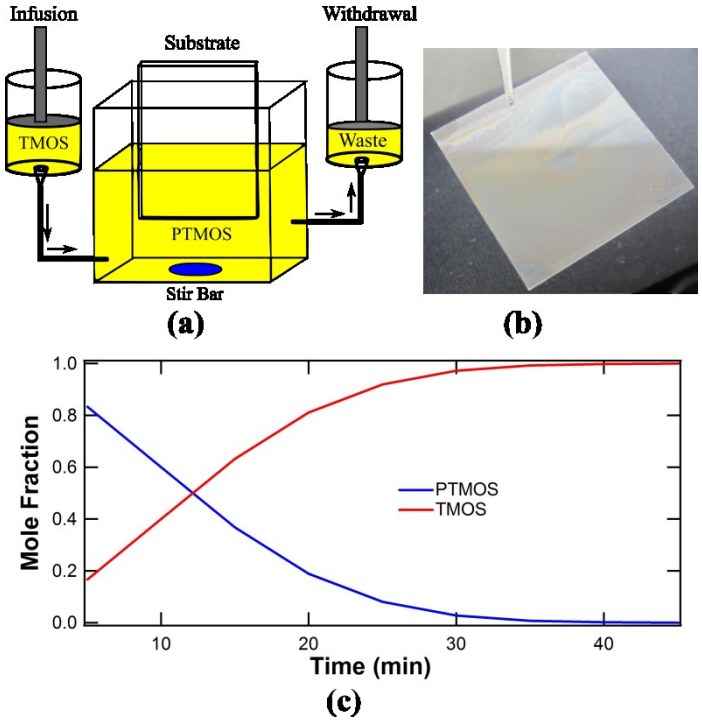

Figure 4.2 a) Schematic showing the apparatus used for infusion-withdrawal dip-coating (IWDC). The deposition reservoir incorporates two openings: a lower inlet for infusion of TMOS derived sol near the magnetic stir bar and an upper outlet for withdrawal of the mixed sols. **b)**

Photograph of a PTMOS-TMOS derived gradient prepared by IWDC, and **c)** change in sol composition during IWDC.

Films were deposited by first filling the reservoir with the PTMOS sol. The base layer-coated substrate was first cleaned in an air plasma for 2 min and then immediately suspended in this sol so that the lower ~20 mm were immersed. A syringe pump programmed to infuse the TMOS sol at a time varying rate was then started. Simultaneously, a second syringe pump programmed to withdraw the mixed sol at a rate 0.1 mL/min faster than the infusion rate was also started. **Table 4.1** shows the rates of infusion and withdrawal programmed in the syringe pumps.

This procedure produced a sol inside the glass reservoir that changes from pure PTMOS to predominantly TMOS over the course of 45 min as shown in **Figure 4.2c**. Thin film deposition took place by rapid evaporation of solvent and the increased concentration of the organosilanes, perhaps, in the form of oligomers in the receding meniscus. Film deposition was performed in a Plexiglas chamber mounted on a floating optical table. The humidity in the chamber was maintained at ~ 60% RH throughout the coating process. Nongradient (uniform) TMOS and PTMOS derived controls were also obtained by dip coating, using the same sols. In this case, the individual sols were drained from the reservoir at the same 0.1 mL/min rate as in gradient deposition by IWDC.

The resulting gradient films and nongradient controls appeared optically clear but incorporated colored interference fringes as shown in **Figure 4.2b** due to some irregular thickness variations. The gradient begins ~ 5 mm from the top edge of the coverslip, where the

PTMOS content is greatest. The initial 5 mm was left uncoated (except for the TMOS base layer) to allow for mounting in the IWDC apparatus.

Table 4.1 Rates of infusion (F_{in}) for the TMOS sol and withdrawal (F_{out}) for the waste programmed into the syringe pumps. The pumping rates changed in 5-min intervals during IWDC. V_{sol} represents the volume of the sol left in the reservoir at the end of each 5-min interval.

Time (min)	F_{in} (ml/min)	F_{out} (ml/min)	V_{sol} (ml)
5	0.3	0.4	8.5
10	0.4	0.5	8
15	0.5	0.6	7.5
20	0.6	0.7	7
25	0.7	0.8	6.5
30	0.8	0.9	6
35	0.9	1	5.5
40	1	1.1	5
45	1.1	1.2	4.5

4.1.4 Gradient Self-Assembled Monolayers (SAMs)

All SAM wettability gradients were prepared by exposure of the base layer-coated substrate to the vapor of one or more organochlorosilanes. For the study presented in **Chapter 6**, one-component and opposed two-component SAM wettability gradients were prepared by employing hydrophilic 3-cyanopropyltrichlorosilane (CN-silane) and hydrophobic octyltrichlorosilane (C8-silane). Both were obtained from Sigma-Aldrich, at 97% purity, and were used as received. For the study presented in **Chapter 7**, one-component SAM wettability gradients were prepared by using only the C8-silane. Table 4.2 provides the vapor pressures (VP) and boiling points (BP) of some of the organochlorosilanes used in this dissertation.

Table 4.2 Vapor pressures and boiling points of the organosilanes employed.

Silane	VP (mm of Hg at 25^{o} C)	BP (760 mm of HG)
C8-silane	0.0797	234.7^{o} C
CN-Silane	0.0447	237.5^{o} C

4.1.5 Vapor-Phase Deposition (VPD)

The vapor phase deposition of the organochlorosilanes was carried out under room temperature and pressure. **Figure 4.3a** shows the apparatus used to prepare two-component gradient SAMs from CN-silane and C8-silane. It consists of a substrate supported on a platform, with the substrate positioned midway between two reservoirs designed to hold the precursor organosilanes. These components were all housed inside a plexiglass box. The box allowed for VPD of gradients in the absence of air currents and under controlled humidity. The humidity inside the chamber was maintained at 60 ± 2% RH for all depositions.

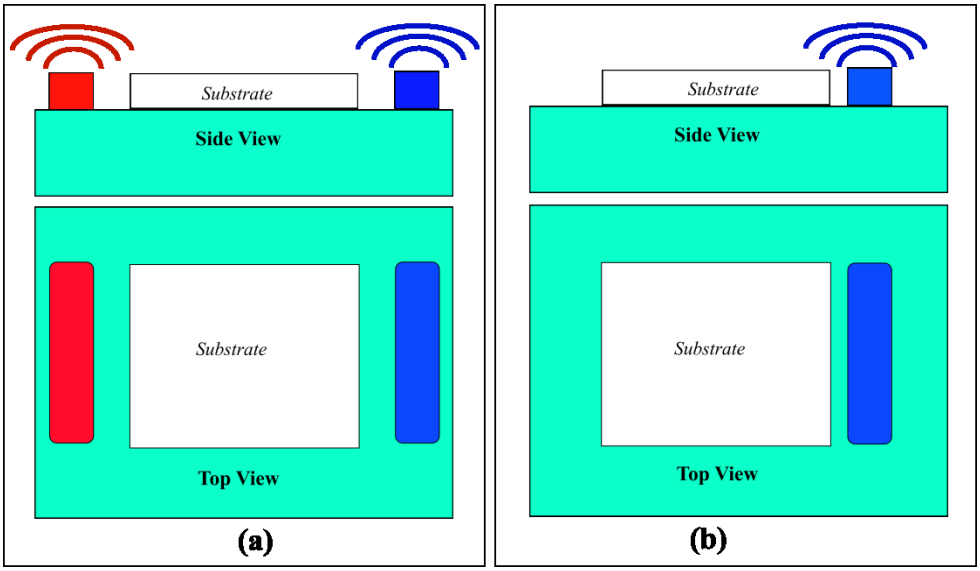

Figure 4.3 Apparatus used for vapor phase deposition of organosilanes. **a)** Top and side views of VPD apparatus used to deposit two-component gradient SAMs. Shown in the figure are two reservoirs for loading CN-silane (red) and C8-silane (blue). **b)** Top and side view of the VPD apparatus used to deposit one-component gradient SAMs. The only reservoir shown is loaded with C8-silane (blue). The entire apparatus is enclosed in a plexiglass chamber to control the humidity during deposition.

The edge-to-edge separation between each reservoir and the substrate was maintained at an experimentally optimized distance of 5 mm in all depositions. Each base-layer-coated substrate was treated in an air plasma for 2 min immediately prior to its insertion in the deposition chamber. The two reservoirs were then loaded with a mixture of paraffin oil (200 μL) and one of the two organosilanes (50 μL). The CN-silane was loaded first and was immediately followed by loading of the C8-silane. The inlets were promptly closed and the substrate was exposed to silane vapor for 5 min. This exposure time was determined to yield optimal results after extensive experimentation. The substrate was immediately removed from the chamber after film

deposition. The resulting gradient SAM films looked optically clear and clean by eye. Each film was then stored in a desiccator under static vacuum for 12 h. These were subsequently spin coated (5000 rpm, 30 s) with a 150 μL aliquot of 4 nM C_{11}OPDI dye (**Figure 4.4**) synthesized in house in HPLC grade ethanol. After coating with dye, each gradient was stored in a desiccator for an additional 48 h before characterization by SMT and other methods.

Figure 4.3b represents the apparatus used to prepare steep one-component SAM wettability gradients. The set up is similar to that used to prepare two-component gradients except for a few changes. In this set up, only one reservoir is used to load a mixture of C8-silane (20 μL) and paraffin oil (200 μL). An experimentally optimized distance of 2 mm is maintained between the substrate and the reservoir. The exposure time of the substrate to silane vapor was 4 min. Each film was stored in a desiccator for at least one hour (but not exceeding 12 h.) before its use to drive droplet motion of DNA solution for stretching of the DNA.

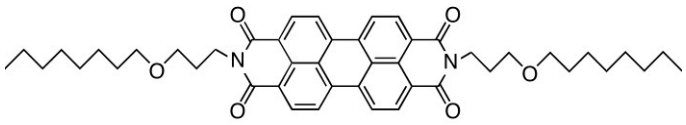

Figure 4.4 Chemical structure of N,N'-bis(octyloxypropyl)-perylene-3,4,9,10-tetracarboxylic diimide (C_{11}OPDI) used as the fluorescent probe.

4.2 Instrumentation

4.2.1 Water Contact Angle (WCA)

The macroscopic wettability along the gradient surface was initially accessed by sessile drop or static water contact angle measurements. The home built apparatus used for contact angle goniometry is shown in **Figure 4.5**. All components of this instrument are mounted on an optical table. The sample is placed on a translational stage. Droplets of high purity water (1.0 μL) are placed along the gradient film using a microliter syringe. Droplet images were acquired with a CCD camera attached to a Navitar zoom lens. A lamp and a thin filter paper (diffuser) were placed behind the droplet for illumination purposes. The filter paper served to make the droplets appear black in the images, as is necessary for measurement precision and image processing.

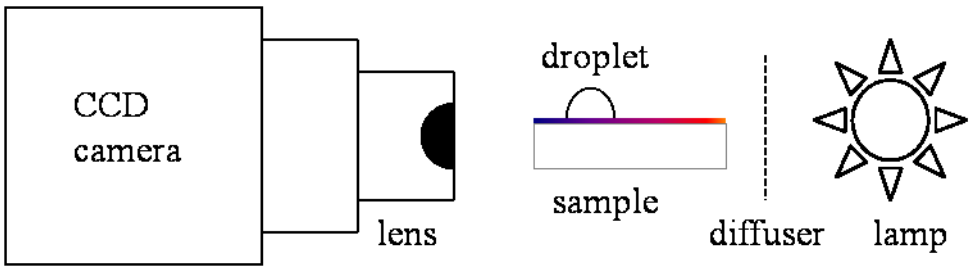

Figure 4.5 Set up used to measure static water contact angles along gradient films.

4.2.2 Spectroscopic Ellipsometry

In this dissertation, spectroscopic ellipsometry (α-SE, J.A. Woolam) was employed to measure the thickness of the silica base layer, the gradients, and the thin water layer condensed on the gradient surfaces. Ellipsometry measures a change in the polarization of light as it reflects from a material surface. The change in polarization is represented as an amplitude ratio tan(ψ) and a phase difference (Δ). Here, linearly polarized light (across all visible wavelengths) was reflected from the sample and the output polarization was measured. The output response

depends on the optical properties of the material, including its thickness. The change in polarization (ρ) is given by following equation-

$$\rho = \tan(\psi)e^{i\Delta} \qquad (4.1)$$

All ellipsometric raw data were globally fit to the "Si with Transparent Film" model available in the CompleteEASE software provided with the instrument. A single layer model was used due to the negligible difference in refractive index of the base layer and the deposited gradient film. **Figure 4.6** shows two sets of ellipsometric data for: **(a)** the base layer alone and **(b)** the base layer after vapor-phase deposition of C8-silane.

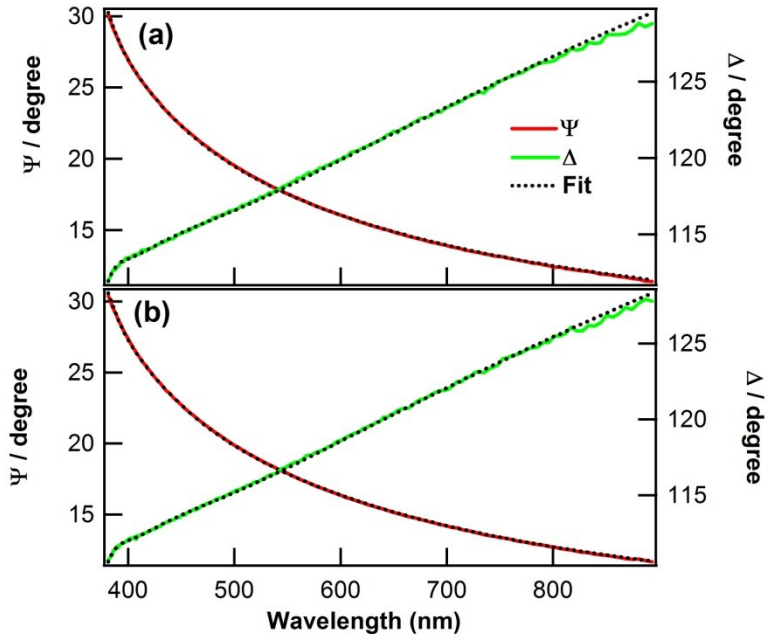

Figure 4.6 Spectroscopic ellipsometry data for **(a)** a thin base-layer coated silicon wafer, and **(b)** the same film after vapor phase deposition of C8-silane. The colored lines represent the raw data fit to a model for a single layer transparent film on silicon (black dashed lines). The Cauchy

relationship was employed to model film dispersion. The parameters obtained by global fitting of data shown in **(a)**: Cauchy A = 1.465 ± 0.0024, B = 7.0 ± 0.9 x 10^{-3} μm^2, C = - 2.3 ± 1 x 10^{-4} μm^4 , n = 1.465, thickness = 25.60 ± .035 nm, and mean square error = 1.1; in **(b):** A = 1.451 ± 0.001, B = 2.5 ± 0.7 x 10^{-3} μm^2, C = - 4.0 ± 0.8 x 10^{-4} μm^4 , n = 1.455, thickness = 26.81 ± 0.29 nm, and mean square error = 0.97. The difference between the two measured thicknesses, ~ 1.21 nm, gives the thickness of the C8-film.

All gradient samples were prepared on base-layer coated silicon substrates for thickness measurements. The thickness of gradients prepared on glass substrates were not uniform. Initially, the thickness of the base layer was measured at an interval of 1mm along each silicon substrate. The gradients were then deposited, and the thickness was again measured from similar positions, to within ±1 mm along each gradient. The difference in thickness between the two measurements gave the thickness of the gradient at each position. In addition, the thicknesses of both the base layer and the gradient films were measured under dry conditions (~ 16% RH) as water adsorbed on the surface was found to increase the observed film thickness. This method was also used to measure the thickness of thin water films adsorbed along the gradient SAM in wettability under different humidity conditions.

4.2.3 Raman Microscopy

The chemical composition of the polarity gradients was determined in Raman scattering experiments. The principle of Raman scattering is based on the inelastic scattering of incident photons by polarizable molecules. Very few (one in a million) of the incident photons can interact with a polarizable molecule and excite the molecule in its vibrational state through a

virtual state. During such transitions, the photon loses energy equivalent to the energy of the vibration probed. As a result the scattered photon has lower energy (frequency) compared to the incident photon. The loss in energy can be calculate as the energy difference between the incident and the scattered photons as shown in following equation-

$$\Delta\tilde{\upsilon}\ (cm^{-1}) = \left[\frac{1}{\lambda_{incidence}} - \frac{1}{\lambda_{scattering}}\right] \times 10^{7} \qquad (4.2)$$

Here, $\Delta\tilde{\upsilon}$ is the Raman shift, while $\lambda_{\text{ incidence}}$ and $\lambda_{\text{ scattering}}$ represent the wavelength of incidence and scattered photons in nm. The vibrational Raman spectrum serves as a finger print for many functional groups. In this dissertation, Raman scattering experiments were performed on a home-built Raman microscope as shown in **Figure 4.7a**. In this microscope, 488 nm light from a diode laser source was reflected from a dichroic mirror into the back aperture of a 1.3 numerical aperture (NA), 100 X oil immersion objective. The light was focused to a diffraction limited spot in the sample. The power was set to 0.6 mW in all experiments. Scattered light was collected from the sample by the same objective. Rayleigh scattered light was blocked by passing the collected light back through the dichroic mirror and through a 488 nm holographic notch filter (Kaiser Optical). Raman scattered photons were directed through a 0.3 m imaging spectrograph (Acton Research) and detected using a thermoelectrically-cooled CCD camera (Andor Newton). Spectra were acquired at 1 mm intervals along and across the gradients.

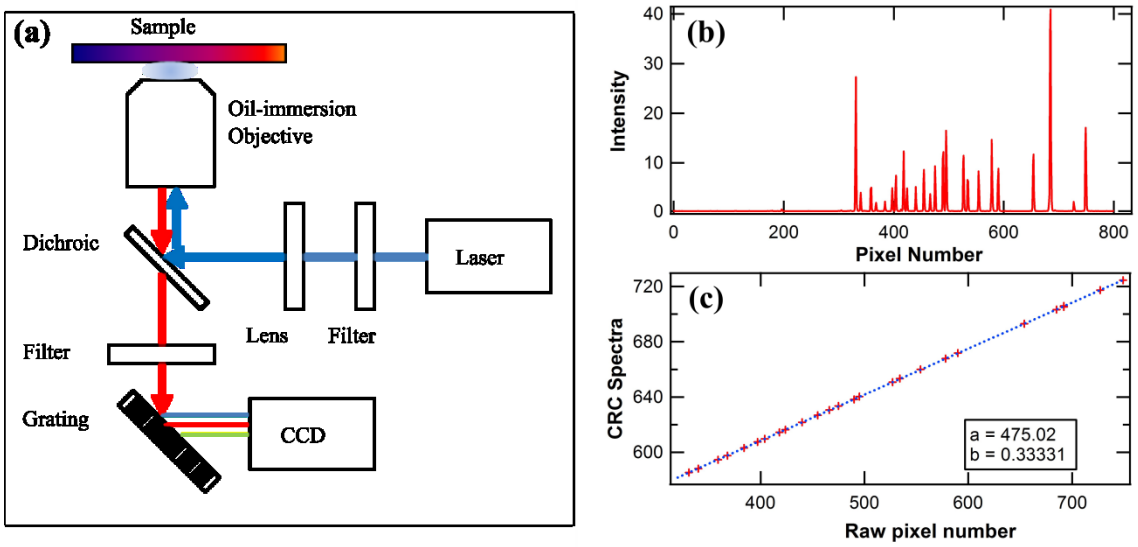

Figure 4.7 a) Optical microscope used to acquire the Raman spectra along the sol-gel derived polarity gradients, **b)** Atomic emission spectra from a neon lamp acquired on the same microscope, and **c)** Calibration of the spectrometer wavelength from the known peak wavelengths of neon emission. Red points show the data while the dashed line shows a linear fit.

The spectrograph was calibrated to determine the wavelength corresponding to each pixel. This was carried out by recording the atomic emission of a neon lamp on the microscope. The atomic emission spectrum of the neon lamp is shown in **Figure 4.7b**. The actual wavelength for neon emission (as reported in the CRC Handbook of Chemistry and Physics) was plotted against the raw pixel number as shown in **Figure 4.7c**. The data were then fit to a line. The results of the fitting were applied for calibrating the wavelength of the Raman spectra acquired from the gradient samples. According to this calibration, $\lambda_{scattering}$ is given by following equation-

$$\lambda_{scattering} = 475.02 + \lambda_0 - \lambda_0' + 0.33 \times P_x \qquad (4.3)$$

Here, λ_0 and λ_0' are the center wavelengths set in the software while acquiring spectra from the neon lamp and the sample, respectively, and P_x represents the pixel count along X-axis of the spectra. The values 475.02 and 0.33 respectively represent the intercept and slope obtained from the calibration procedure, as shown in **Figure 4.7c**.

4.2.4 Wide-Field Fluorescence Microscopy

All single-molecule experiments in this dissertation were performed on an inverted wide-field fluorescence microscope. The microscope was custom built on a floating optical table. Two separate configurations of the wide-field microscope were used for different studies.

4.2.4.1 Two-color single-molecule spectroscopy (SMS)

For this purpose, gradients doped to nanomolar levels with Nile Red were mounted atop the microscope. The primary components along the optical path are depicted in **Figure 4.8a**. Individual Nile Red molecules were excited by 532 nm laser light. The source light was passed through a spinning optical diffuser, reflected from a dichroic beam splitter (Chroma 555, DCLP) and subsequently focused into the back aperture of a 1.49 NA 100X oil immersion objective (Nikon Apo-TIRF). The illuminated area in the sample was ~15 μm in diameter. The incident power was maintained at 1-3 mW in all experiments. Nile Red fluorescence was collected by the same objective, in an epi-illumination geometry, and separated from the excitation light by passage back through the same dichroic beam splitter and a 550 nm colored-glass long-pass filter. The fluorescence was subsequently split into two spectral bands using an image splitter (Cairn Research OptoSplit II). Separation of the two bands was accomplished using a second dichroic beam splitter (Chroma 610, DCLP) and appropriate bandpass filters, which divided the

fluorescence into separate spectral bands spanning 640±20 nm and 590±20 nm. Fluorescence in these two bands was simultaneously detected by a thermoelectrically-cooled CCD camera (Andor iXon DU-897). Fluorescence videos 50-100 frames in length were acquired from each location in the sample at a rate of ~ 2 frames/sec. Videos were collected from five different locations across the gradient at each of ten positions along the gradient (i.e., on a 1 mm X 1 mm grid), for a total of 50 videos.

The videos obtained were analyzed using software written in-house, in the LabView programming environment. This software was used to select the two images depicted in each video frame (typically 100 X 120 pixel regions) and to correct for offset and any rotation of the images imparted by the optical system. Image rotation was minimal and was always less than $\pm 2^{o}$. The software was then used to automatically locate each fluorescence spot in the pairs of images. These were subsequently fit to 2D Gaussian functions to determine the location and peak signal for each spot.

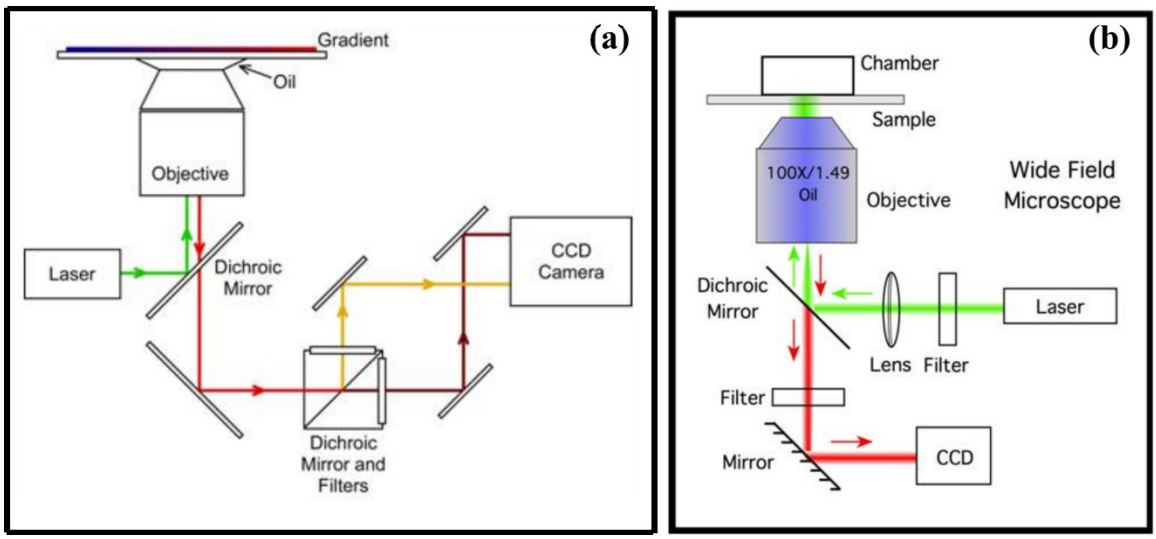

Figure 4.8 Wide-field microscope used to acquire **a)** two-color fluorescence videos of Nile Red incorporated within polarity gradients, **b)** wide-field fluorescence videos for single molecule tracking studies of C11OPDI dye molecules along the CN-C8 derived gradient SAMs.

4.2.4.2 Single molecule tracking (SMT)

All SMT experiments were performed on the same inverted wide-field fluorescence microscope used above, with a few differences in the optical path, as shown in **Figure 4.8b**. In these experiments, each sample was again mounted over a high numerical aperture (NA) oil immersion objective (Nikon Apo TIRF, 100X, 1.49 NA) that was used for both sample illumination and collection of the resulting fluorescence. An enclosed plexiglass chamber was placed over the sample and was used to control the ambient RH by purging the box with dry or humidified nitrogen gas. Blue light (488 nm) from a diode laser was used for excitation of the C_{11}OPDI dye doped into the films. Prior to incidence on the sample, the excitation light was converted to circular polarization, passed through a spinning optical diffuser, reflected off a dichroic beam splitter (Chroma, 505 DCLP) and focused into the back aperture of the objective.

The excitation power was maintained at 100-125 μW in all experiments, yielding average excitation intensities of ~56-70 W/cm^2. The relatively low excitation intensity allowed for the dye molecules to be tracked over long periods of time prior to photobleaching. The fluorescence emitted by the individual dye molecules was separated from the excitation light by passing it through the aforementioned beam splitter and through a band pass filter (Chroma, HQ 535/50). The fluorescence was detected using a CCD camera (Andor iXon DU-897). Fluorescence videos 450 frames in length were recorded for each location on the sample at a rate of 2 frames/s. Videos were acquired from a total of 70 distinct locations along each gradient at 1 mm spacings in each dimension. The data acquired spanned distances of 4 mm across each gradient and 13 mm along each gradient with a total of five videos collected across the gradient at each of 14 different positions along the gradient. The fluorescent spots produced by the single molecules in each video frame were detected, fit to 2D Gaussian intensity profiles, and linked into trajectories using a LabView-based particle-tracking program written in-house.

Chapter 5 - Single Molecule Spectroscopic Imaging Studies of Polarity Gradients Prepared by Infusion-Withdrawal Dip-Coating

5.1 Introduction

Chemical gradients are materials that are designed to exhibit continuous, gradually changing chemical or physical properties along one, two, or even three dimensions.[1,3,78] They find a wealth of possible applications in stationary-phase-gradient chemical separations[35] and high throughput screening,[79-81] and for controlling the motions of liquid droplets,[12] macromolecules,[29] vesicles,[31] nanoparticles[27] and cells.[32] Gradients have been prepared by a variety of approaches, including by self-assembly of alkanethiols[82] and organosilanes,[12] and by chemical attachment[83-85] of organic polymers on surfaces. Gradual variations in film composition in many of these were achieved by vapor diffusion,[12] solution diffusion,[82] lithographic approaches,[86] printing techniques,[9] electrochemical methods[51,85,87] or by controlled immersion[5] or infusion.[88] The full complement of methods and materials previously employed for gradient production is described in contemporary reviews.[1-4,78] Most recently, our groups have begun to explore the use of sol-gel chemistry coupled with infusion-withdrawal dip-coating (IWDC)[16,19] and controlled-rate infusion[6,17,89] methods to prepare organosilane-based gradients.

Sol-gel chemistry[90-92] has several unique attributes that make it nearly ideal for the preparation of thin film and surface gradients.[6,16,17,19,35,89] First, the chemistry of the sol-gel process is relatively simple. Sol preparation begins by dissolving one or more organoalkoxysilane precursors of general formula $R_x'Si(OR)_{4-x}$ in a suitable solvent, along with a near-stoichiometric amount of water. Here, R usually represents a methyl or ethyl group and R' a non-hydrolyzable organic group. A wide variety of precursor silanes having different R' groups are commercially available, allowing for access to a broad range of physical (e.g., wettability, polarity, charge) and chemical (e.g., acidity) gradients. Upon addition of acid or base to the sol, the alkoxy groups hydrolyze to form silanols that subsequently condense to form a gel. Their condensation with OH groups on oxide surfaces affords an efficient means for anchoring the gradient to a substrate surface. Sol-gel-based gradients can be produced by relatively simple dip-coating procedures,[16,19] or by infusion of a sol into a suitable reservoir,[6,89] capillary[17] or microfluidic device.[48] In all such cases, the presence of multiple reactive groups on the precursor silanes allows for cross-linking of the gel, making the resulting gradients mechanically robust and relatively stable. Finally, the rapid increase in sol viscosity that occurs upon gelation may allow for metastable materials compositions and morphologies to be "frozen in" to the gradients, providing access to unique non-equilibrium systems.

Given the broad interest in gradient materials and the aforementioned attributes and enormous flexibility of sol-gel approaches, it is somewhat surprising that these methods have not been more widely explored for the fabrication of gradient materials to date. The limited use of sol-gel methods in gradient production is likely due to a dearth of knowledge on their chemical and physical properties. While we have reported XPS,[6,89] FTIR,[19] fluorescence,[16] streaming potential[17] and water contact angle[16] studies of the macroscale properties of amine-[6,17,89] and

methyl-modified[16] silica gradients, only a single report on their sub-micrometer-scale properties has been published.[19] Much remains to be learned in particular about the nanoscale properties of these gradients.[93] Ideally, any such gradient would be comprised of molecularly mixed components and would exhibit gradual compositional and physical properties variations down to molecular length scales. In reality, such idyllic character is seldom observed. Gradient complexity may arise from phase separation of the gradient components during film formation, due to limited precursor miscibility. Instead of gradually varying properties, such gradients would exhibit step-wise (or discrete) properties variations on the length scale of the resulting domains. A better understanding of the compositional and physical properties variations occurring along gradients requires the implementation of new methods to probe their properties across a range of length scales from the macroscale down to molecular levels.

This chapter describes two-color single molecule spectroscopic (SMS) imaging studies[94] of two-component organosilane-based polarity gradients prepared by IWDC.[16] Gradient films are obtained by immersing a substrate in a binary sol mixture of time varying composition. In the present studies, gradients were obtained by slowly mixing a relatively nonpolar phenyltrimethoxysilane (PTMOS) sol with a polar tetramethoxysilane (TMOS) sol. The mole fraction of the former decreased while that of the latter increased in time during dip coating. Sessile drop water contact angle measurements and Raman mapping were used to verify that a one-dimensional gradient was formed, on macroscopic length scales. Extensive SMS imaging studies were performed to probe the polarity properties of the same films on length scales ranging from nanometers to millimeters. The solvatochromic dye Nile Red was used as a polarity sensitive probe. The results afforded quantitative estimates of the local film polarity,[94] via the Clausius-Mossotti factor. Ensemble data compiled from the SMS experiments depict a

continuous increase in the polarity of the film running from the high-phenyl end towards the low-phenyl end. These same data also reveal dramatic variations in the local film polarity on nanometer length scales. Two distinct classes of environment are found in some film regions, consistent with phase separation of the polar and nonpolar film components.

5.2 Experimental Considerations

5.2.1 Sample Preparation

Base layer coating of substrates. Gradient films were found to be more uniform and adhered better to the substrate surface when deposited on a silica base layer. Silica base layers were prepared from TMOS based sols. TMOS (99%) was obtained from Sigma-Aldrich and was used as received. Each sol was prepared by mixing TMOS, ethanol (200 proof), deionized water, and 0.1M HCl in mole ratios of 1.0:31.5:5.5:0.01 (TMOS:ethanol:H_2O:HCl) in a clean glass vial. The sol was subsequently stirred for 1 h and aged in a desiccator for 23 h prior to use.

Glass coverslips (FisherFinest Premium, 25 mm x 25 mm) were employed as substrates. Prior to use, each was cleaned by exposure to an air plasma for 5 min. A 150 uL aliquot of a TMOS sol prepared as described above was then spin coated onto the coverslip (5000 rpm, 30 s). Base layer films obtained by this procedure were uniform, with thicknesses of 150 ± 10 nm, as determined by spectroscopic ellipsometry.

Gradient films. All gradients were prepared by IWDC. In IWDC, the substrate surface is exposed to a sol of time varying composition. In the present studies, separate sols derived from TMOS and PTMOS were employed. Each was prepared using a two-step acid/base hydrolysis and condensation process. PTMOS (97%) was obtained from Sigma-Aldrich and was used as

received. TMOS sols were prepared in silane:ethanol:H_2O:HCl(0.1M):NH_3(1M) mole ratios of 1.0:59.0:9.8:0.01:0.07, while PTMOS sols were prepared with similar mole ratios of 1.0:60.9:10.2:0.01:0.07.

Sols were prepared by first mixing the silane, ethanol and acid. The TMOS and PTMOS sols were then stirred for 5 min and 10 min, respectively. Base (NH_3) was subsequently added to both sols. Sufficient Nile Red dye was also added at this point (in ethanolic solution) so that its final concentration in the sols was 1.0 nM. After addition of the base and dye, the sols were again stirred for 35 and 30 min, respectively, to bring the total stirring time in each case to 40 min. The TMOS and PTMOS sols were then aged for 1.5 h and 4 h, respectively, in a desiccator, prior to use.

IWDC was performed in a specially designed glass reservoir. A diagram of the setup is given in **Figure 4.2 (a)**. Films were deposited by first filling the reservoir with the PTMOS sol. The base layer coated substrate was then suspended in this sol so that the lower ~20 mm were immersed. A syringe pump programmed to infuse the TMOS sol at a time varying rate was then started. Simultaneously, a second syringe pump programmed to withdraw the mixed sol at a rate 0.1 mL/min faster than the infusion rate was also started. This procedure produced a sol of time varying composition (ranging from a pure PTMOS sol to a predominantly TMOS sol) as shown in **Figure 4.2 (c)** that slowly receded down the substrate surface over the course of 45 min. Film deposition was performed in a Plexiglas chamber mounted on a floating optical table. The humidity in the chamber was maintained at ~ 60% RH throughout the coating process. Nongradient (uniform) TMOS and PTMOS derived controls were also obtained by dip coating, using the same sols. In this case, the individual sols were drained from the reservoir at the same 0.1 mL/min rate as in gradient deposition by IWDC.

The resulting gradient films and nongradient controls appeared optically clear but incorporated colored interference fringes as shown in **Figure 4.2 (b)** due to some irregular thickness variations. As in a previous report, these variations are attributable to sticking and slipping of the sol meniscus during the coating process. The gradient begins ~ 5 mm from the top edge of the coverslip, where the PTMOS content is greatest. The initial 5 mm was left uncoated (except for the TMOS base layer) to allow for mounting in the IWDC apparatus. Hereafter, the high-phenyl end of the gradient will be referred to as the top of the gradient and will be designated as the 0 mm position on the substrate. Likewise, the low-phenyl end will be referred to as the bottom of the gradient.

5.2.2 Gradient Characterization

Water contact angle measurements. Sessile drop water contact angles were measured on a home-built instrument. Droplets of 1.0 μL were deposited along the gradient and non-gradient control surfaces using a microliter syringe. Images of the droplets were acquired using a CCD camera and were analyzed using software by First Ten Angstroms.

Raman microscopy. Raman scattering experiments were performed on a home-built Raman microscope shown in **Figure 4.7**. This microscope employed a diode laser emitting 488 nm light as the source. The source light was reflected from a dichroic mirror into the back aperture of a 1.3 numerical aperture (NA) 100 X oil immersion objective, which focused the light to a diffraction limited spot in the sample. The incident power was set to 0.6 mW in all experiments. Scattered light was collected from the sample by the same objective. Rayleigh scattered light was blocked by passing the collected light back through the dichroic mirror and through a 488 nm holographic notch filter (Kaiser Optical). Raman scattered photons were directed through a 0.3 m imaging spectrograph (Acton Research) and detected using a

thermoelectrically-cooled CCD camera (Andor Newton). Spectra were acquired at 1 mm intervals along and across the gradients.

Two-color single molecule spectroscopic (SMS) imaging. The polarity properties of individual nanoenvironments along the gradients were assessed by two-color SMS imaging.[94] For this purpose, gradients doped to nanomolar levels with Nile Red were mounted atop a wide-field fluorescence video microscope. This microscope has been described previously in detail.[95] The primary components along the optical path are depicted in **Figure 4.8a**. Individual Nile Red molecules (**Figure 4.1**) were excited by 532 nm laser light. The source light was passed through a spinning optical diffuser, reflected from a dichroic beam splitter (Chroma 555, DCLP) and subsequently focused into the back aperture of a 1.49 NA 100X oil immersion objective (Nikon Apo-TIRF). The illuminated area in the sample was ~15 μm in diameter. The incident power was maintained at 1-3 mW in all experiments. Nile Red fluorescence was collected by the same objective, in an epi-illumination geometry, and separated from the excitation light by passage back through the same dichroic beam splitter and a 550 nm colored-glass long-pass filter. The fluorescence was subsequently split into two spectral bands using an image splitter (Cairn Research OptoSplit II). Separation of the two bands was accomplished using a second dichroic beam splitter (Chroma 610, DCLP) and appropriate bandpass filters, which divided the fluorescence into separate spectral bands spanning 640±20 nm and 590±20 nm. Fluorescence in these two bands was simultaneously detected by a thermoelectrically-cooled CCD camera (Andor iXon DU-897). Fluorescence videos 50-100 frames in length were acquired from each location in the sample at a rate of ~ 2 frames/sec. Videos were collected from five different locations across the gradient at each of ten positions along the gradient (i.e., on a 1 mm X 1 mm grid), for a total of 50 videos.

The videos obtained were analyzed using software written in-house, in the LabView programming environment. This software was used to select the two images depicted in each video frame (typically 100 X 120 pixel regions) and to correct for offset and any rotation of the images imparted by the optical system. Image rotation was minimal and was always less than $\pm 2^{o}$. The software was then used to automatically locate each fluorescence spot in the pairs of images. These were subsequently fit to 2D Gaussian functions to determine the location and peak signal for each spot. Spots produced by the same molecule were subsequently linked into trajectories using methods similar to those reported in the literature.[96]

5.3 Results and Discussion

Prior to characterization of the PTMOS-TMOS derived polarity gradients, significant effort was devoted to optimization of sol compositions, sol mixing and aging times and exact film deposition conditions. This process included selecting conditions under which the precursor sols remained optically clear during film deposition, and for which gelation occurred well after deposition was complete. The experimental conditions were also adjusted to avoid dewetting of the TMOS base layer and to obtain films that appeared most uniform by eye. The exact conditions selected are defined under Experimental Considerations. The resulting gradients formed by IWDC were ~145±14 nm thick (on top of the base layer), as determined by spectroscopic ellipsometry. Several replicate gradients and nongradient controls were produced and characterized by water contact angle measurements, Raman mapping and SMS imaging, as described below. All were found to yield similar general trends. However, small but obvious variability was observed in the properties exhibited by replicate gradients. Variability in gradient properties was attributed to subtle differences in the exact conditions of film deposition, which

resulted primarily from variations in the extent of sol mixing during IWDC. Because of this film-to-film variability, all gradient results described below were obtained from a single film. To avoid contamination of the sample, single molecule experiments were performed first, followed by Raman mapping and water contact angle measurements. These results are described below in reverse order.

5.3.1 Water Contact Angle Measurements.

Water contact angle data obtained along a PTMOS-TMOS derived gradient are shown in **Figure 5.1**. These data were acquired at 2 mm intervals along the gradient, with three replicate measurements made at 2 mm intervals across the gradient in each case. The data shown depict the average and standard deviations for each position. The mean water contact angle was found to decrease, as expected, from the top (high-phenyl end) to the bottom (low-phenyl end) of the gradient. The increase in wettability towards the low-phenyl end is caused by an increase in the density of SiOH sites, along with a corresponding decrease in the density of phenyl groups. The error bars shown in **Figure 5.1** are relatively large and are attributed to gradient heterogeneity extending down to micrometer length scales,[97,98] especially in central gradient regions; the origins and impacts of this heterogeneity are addressed further, below.

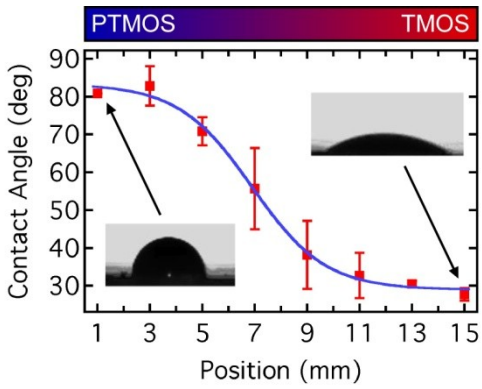

Figure 5.1 Sessile drop water contact angle data obtained along a single PTMOS-TMOS derived polarity gradient. The data points show the average contact angle measured at three different positions across the gradient at each designated position along the gradient. The error bars depict the standard deviation of the measured values. The solid blue line is a sigmoidal curve, which has been added only to better depict the trend in the data.

5.3.2 Raman Microscopy.

Figures 5.2 a) & b) show Raman spectra obtained from the same PTMOS-TMOS derived gradient and from a uniform TMOS derived control, respectively, in the C-H stretching region. These spectra have been corrected for a complex sloping baseline and are offset vertically to allow for better viewing. The Raman band peaked at ~ 3059 cm^{-1} corresponds to the expected phenyl C-H stretch.[99] The peak at ~ 2937 cm^{-1} falls in the aliphatic C-H stretching region and is attributed to the presence of residual unhydrolyzed methoxy groups; its presence is neglected in the remainder of this report. The area under the 3059 cm^{-1} peak is expected to be proportional to the phenyl content of the film. However, a small peak in this same region also appears in the TMOS derived base layer spectrum shown in **Figure 5.2b**. Its presence in the latter is believed to result from a weak contribution by the immersion oil used in the microscope. **Figure 5.2c** plots the area under the 3059 cm^{-1} peak as a function of position along the gradient, after subtraction

of the oil background. The 3059 cm^{-1} peak area exhibits a gradual decrease from the top of the gradient, towards the bottom, as expected for decreasing phenyl content. The relative density of phenyl groups is concluded to change by at least a factor of two along the length of the gradient mapped. Instrument limitations prevented access to the very top and bottom of the gradient in the Raman experiments. As a result, the length of the gradient probed in **Figure 5.2c** is shorter than in **Figure 5.1**. The error bars included in **Figure 5.2c** depict the standard deviation from five replicate measurements made at 1 mm intervals across the gradient. As with the water contact angle data, the relatively large error bars reflect a certain level of heterogeneity in the gradient. In this case, they reflect gradient heterogeneity on micrometer length scales.

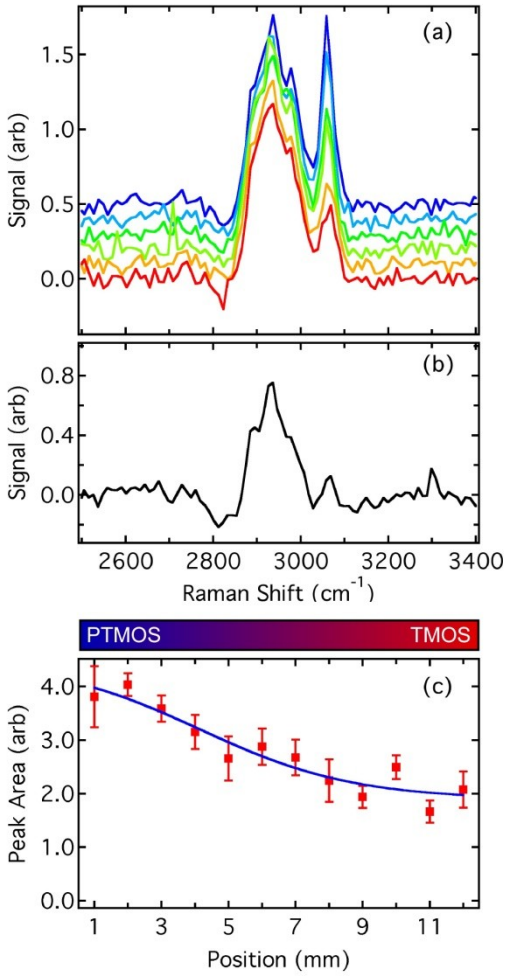

Figure 5.2 a) Raman spectra in the C-H stretching region along the PTMOS-TMOS derived gradient. The spectra shown were acquired at 2 mm intervals (starting at 1 mm) from the high-phenyl end (blue) to the low-phenyl end (red). Each represents the average of five spectra acquired across the gradient. The spectra have been baseline corrected and offset vertically to allow for better viewing. **b)** Raman spectrum from a TMOS derived base layer, plotted as the average of five replicate spectra. **c)** Average area under the peak at 3059 cm^{-1} as a function of position along the gradient, from five replicate measurements. The error bars represent the standard deviation of the five measurements. These data have been corrected for the small background peak in panel b. The solid blue line is a sigmoidal curve, which has been added only

to better depict the trend in the data. These data were collected by Chelsea Hanks, under the direction of Dipak Giri.

5.3.3 Calibration of The Nile Red Response.

Nile Red is a strongly solvatochromic dye[100,101] that is also sufficiently fluorescent to allow for its detection at the single molecule level.[102,103] It has been previously employed by our group to quantitatively assess the static and dynamic polarity properties of nongradient organic polymer[103] and sol-gel-derived silica films.[75,104] More recently, it has been used by Reid and coworkers for quantitative estimation of dielectric constants in single molecule studies of organic polymer films.[94]It is used here for a similar purpose.

Estimation of gradient polarity from Nile Red emission data requires the careful calibration of its response to environments of different dielectric constant. For this purpose, solution phase (bulk) fluorescence spectra were first acquired in a series of solvent mixtures. **Figure 5.3a** presents representative data obtained using a conventional fluorimeter. Ethanol and toluene were employed as solution-phase models for the silica and phenyl-modified silica environments in the gradients. The data in **Figure 5.3a** reveal a monotonic bathochromic shift in the emission maximum from ~ 565 nm in pure toluene to ~ 630 nm in pure ethanol. In particular, the polarity sensitivity of Nile Red is attributable to the charge-transfer character of its lowest energy electronic transition.[105,106] The fluorescence intensity was also found to decrease as the solvent polarity increased, as expected.[100,107]

The polarity of the environment surrounding each Nile Red molecule can be characterized by monitoring its fluorescence in two spectral bands near its emission maxima in polar and nonpolar media. In the present work, Nile Red emission was monitored in bands spanning 640±20 nm and 590±20 nm. Because the fluorescence microscope employed for SMS imaging

experiments exhibited different transmission characteristics than the fluorimeter employed above, calibration of the Nile Red response was actually performed on the microscope itself. For this purpose, an optical cell was constructed by drilling a small hole in a glass microscope slide. The hole was filled with the same series of Nile Red doped solvent mixtures employed above, sealed with a cover glass and placed on the optical microscope. Nile Red emission was excited at 532 nm and simultaneously detected in the aforementioned spectral bands. After proper subtraction of the detector background counts, the emission signals at 590 and 640 nm were used to determine the emission ratio, E, as given by **equation 5.1**.

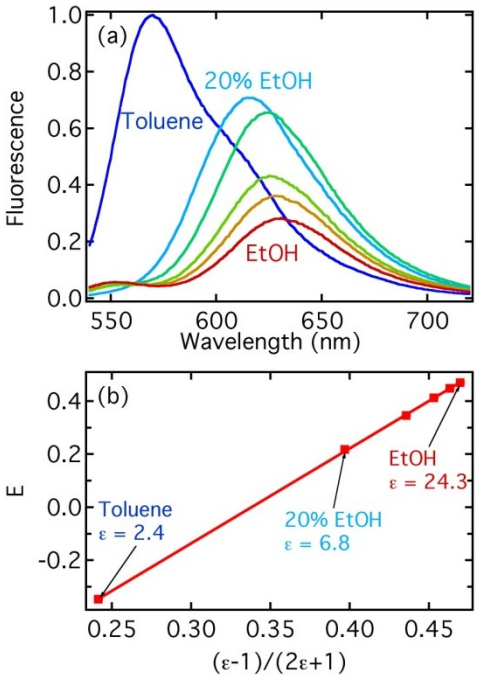

Figure 5.3 a) Fluorescence spectra obtained from Nile Red (100 nM) in different solvent mixtures with toluene:ethanol ratios of 100:0, 80:20, 60:40, 40:60, 20:80, 0:100 (vol%). The fluorescence was excited at 532 nm. **b)** Plot of the Nile Red emission ratio, E, as a function of the Clausius-Mossotti factor for the series of solvent mixtures. The data in **b)** were acquired on the same microscope used to collect the single molecule data.

$$E = \frac{I_{640} - I_{590}}{I_{640} + I_{590}} \qquad (5.1)$$

$$E = K\left(\frac{\varepsilon - 1}{2\varepsilon + 1}\right) + C \qquad (5.2)$$

The emission ratio was subsequently plotted as a function of the Clausius-Mossotti (CM) factor, (ε-1)/(2ε+1), for the solvent mixtures employed, as shown in **Figure 5.3b**. The dielectric constant for each solvent mixture was determined from the known dielectric constants of toluene (2.4) and ethanol (24.3),[108] assuming a linear dependence on the volume fraction of each solvent in each mixture. A nearly perfect linear relationship between E and the CM factor was obtained (see **Figure 5.3b**), as defined in **equation 5.2**. Fitting of the data in **Figure 5.3b** to **equation 5.2** yielded values of 3.57±0.01 and -1.21±0.01 for the constants *K* and *C*, respectively. These constants are employed below for estimation of the polarity (i.e., the CM factor) of the nanoscale environments surrounding each molecule in SMS imaging studies.

5.3.4 Single Molecule Studies of Gradient Polarity.

Environmental polarity was probed on nanometer length scales in gradient and nongradient films by recording two-color SMS videos of the Nile Red doped samples. Videos were acquired from approximately 50 distinct regions along each gradient. These videos revealed the presence of well-separated fluorescent spots. **Figures 5.4 a) &b)** depict a representative pair of images taken from one such video obtained near the high-phenyl end of the gradient analyzed in **Figures 5.1, 5.2**. The fluorescent spots observed were attributed to excitation and detection of emission from single Nile Red molecules. In most instances, pairs of corresponding spots appeared at

identical locations in both the 590 and 640 nm videos (compare **Figures 5.4 a,b**). The relative intensities of the pairs of spots were found to vary from spot to spot, as expected for polarity-dependent variations in the emission spectrum of each molecule.

Automated spot location and tracking software written in-house was used to detect the individual pairs of spots in the video data. Once a given spot was located in either the 590 or 640 nm image, a search was subsequently initiated for its pair in the other image. The intensity profiles produced by each spot were then fit to 2D Gaussian functions to determine their precise locations and their signal levels. The signal level was obtained as the amplitude of the Gaussian fit. The individual spots were then linked into pairs of trajectories, using methods described in the literature.[96] Representative results are shown in **Figure 5.4d**.

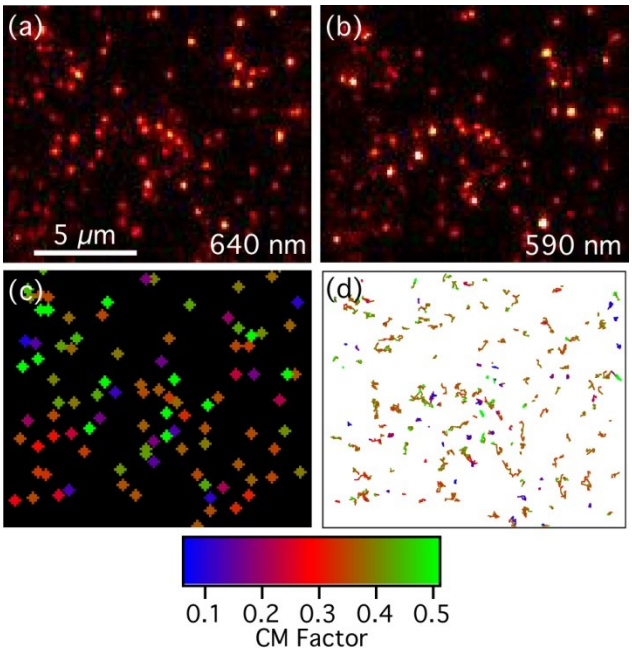

Figure 5.4 a), b) Fluorescence images showing Nile Red single molecule emission near 640 nm and 590 nm, respectively. The two images are of the same region near the high-phenyl end (~ 1 mm from the top) of the PTMOS-TMOS derived gradient. Both images are plotted on identical

intensity scales (350 counts maximum). **c)** Image showing the CM factor (colored diamonds, see color bar) determined by applying **equation. 5.2** in the analysis of the signal from each molecule. **d)** Trajectories (> 6 frames in length, with total signal > 1.5 times the background noise) showing the motions of the individual molecules. The color scale shows the CM factor along each trajectory.

The polarity of each local environment probed by the individual molecules was determined by calculating the emission ratio, E, (see **equation 5.1**) on a spot-by-spot basis, from the two-color SMS image data. The CM factor for each spot was subsequently calculated from **equation 5.2**, using the *K* and *C* parameters given above. **Figure 5.4c** plots an image depicting the CM factors (colored diamonds) obtained from the molecules detected in **Figures 5.4a,b**. The colored trajectories plotted in **Figure 5.4d** show the CM factor for each trajectory along the length of the video data. Only trajectories longer than six frames are shown. These data suggest that the local film polarity is highly variable, with some molecules exhibiting CM factors near 0.5 while others yield values ranging down to near zero. The largest fraction of spots appear to have CM factors near 0.3, consistent with a dielectric constant of ~ 3.3, slightly larger than that of pure toluene.

As is apparent from **Figure 5.4d** a large fraction of the molecules detected are mobile. Unlike our previous studies of methyl-modified silica gradients, in which molecular mobility was found to increase with increasing film organic content,[19] the present materials reveal no clear trend in mobility, possibly due to higher viscosity in the PTMOS-based films.

The mobility of the molecules allows for the polarity to be assessed across short distance scales along the gradient. **Figure 5.5** plots three example trajectories selected from a region 2 mm down the gradient relative to that shown in **Figure 5.4**. **Figure 5.5a** (left panel) plots the trajectory of a mobile molecule, while **Figure 5.5a** (right panel) plots its E value and CM factor

as a function of time. These data appear to show the molecule moving back and forth between two or more regions of relatively low (CM factor ~ 0.4) and relatively high (CM factor ~ 0.6) polarity. Such results may reflect temporal, spatial or simultaneous temporal and spatial variations in the local polarity. Temporal fluctuations in the local polarity may arise from motions of any (organo)silane oligomers contained within the film.[19] In the present case, spatial variations are most likely dominant. Were the observed variations due to temporal fluctuations alone, the polarity values obtained would not show such a clear spatial dependence (see **Figure 5.5a**, left panel). **Figure 5.5b** (left and right) plots similar data for a molecule confined to a smaller region of the gradient. In this case, the polarity remains approximately constant across the trajectory (CM factor ~ 0.35). Very few fluctuations are observed to fall outside the range expected from the measurement error (the error bars represent the standard deviation) for this molecule. Finally, **Figure 5.5c** (left and right) plots data from a molecule that is initially mobile but quickly becomes confined in a small region of the sample. Within this region, the polarity appears to abruptly increase midway through the trajectory and then later decreases to approximately its original value. In this case, it is most important that the nonpolar and polar measurements appear to come from regions that are closely overlapped in the film plane. The two environments associated with these variations may arise from differences in the film properties along the depth dimension, or they may be due to temporal fluctuations in the environmental polarity. Unfortunately, it is not possible to distinguish between these two mechanisms at the present time.

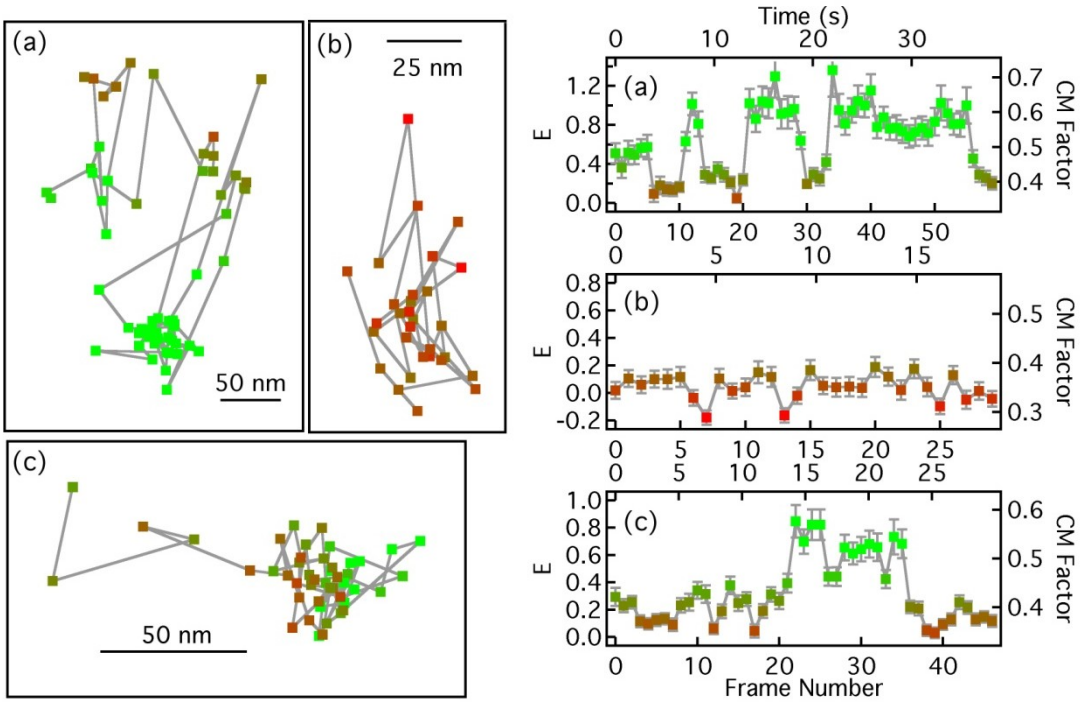

Figure 5.5 a) – c) Representative trajectories (left) and associated polarity data (right) obtained for three single molecules near the high-phenyl end (~ 3 mm from the top) of the polarity gradient. The polarity plots depict the emission ratios, E, and the CM factors for each molecule as a function of frame number (bottom axes) and time (top axes). The data point colors depict the E values and CM factors at each point. The color scale is the same as in Figure **4c,d**. Error bars are included on each of the E and CM factor plots. These were determined from the measured signal levels in each detection channel.

It should be emphasized that the data in **Figures 5.5a,c** depict rare behavior. The majority of trajectories detected exhibit polarity values that remain relatively constant (similar to **Figure 5.5b**) along their lengths, suggesting the molecules spend much of their time in regions of relatively uniform polarity, at least over the tens of seconds they can be followed, prior to photobleaching. In addition, as is also evidenced in **Figures 5.5b,c**, the CM factors occasionally

take on values > 0.5. Such values frequently appear under low signal-to-noise conditions, as reflected by the large error bars on some data points. However, they may also result from specific molecule-matrix interactions (e.g. hydrogen bonding of Nile Red to the matrix[104]). In fact, the CM factor is based on a continuum model and does not allow for the possibility of such interactions.

Polarity data were obtained from several thousand molecules detected along much of the gradient. Unfortunately, physical limitations of the microscope prevented data collection from the very top and bottom of the gradient so that only the middle ~ 10 mm were accessible. The full range of behaviors exhibited by the molecules in the associated trajectories is most efficiently visualized in histogram form. **Figure 5.6** plots these histograms, which depict the distributions of E values and CM factors obtained. Because many of the molecules were found to be mobile, their trajectories were deemed to represent multiple *unique* measurements of film polarity as the molecules explored different film regions. Therefore, in compiling data for these histograms, the individual trajectories were first broken up into segments representing *unique* film regions. Trajectory segments were identified by comparing the frame-to-frame displacement of each molecule to the estimated spot localization precision. As is now well known, the location of each molecule can be determined to much higher precision than expected from the diffraction limited resolution of the microscope.[72,74,109,110] In the present studies, a mean localization precision of 22.5 nm was estimated from the observed signal and noise levels, using the method of Webb, et al.[111] Spot displacements greater than three times this distance from the mean position of one or more other spots along the same trajectory were considered to represent unique measurements of gradient polarity. Each of these *unique* measurements is assumed to

define the polarity properties of one nanoenvironment and makes an independent contribution to the histograms shown in **Figure 5.6**.

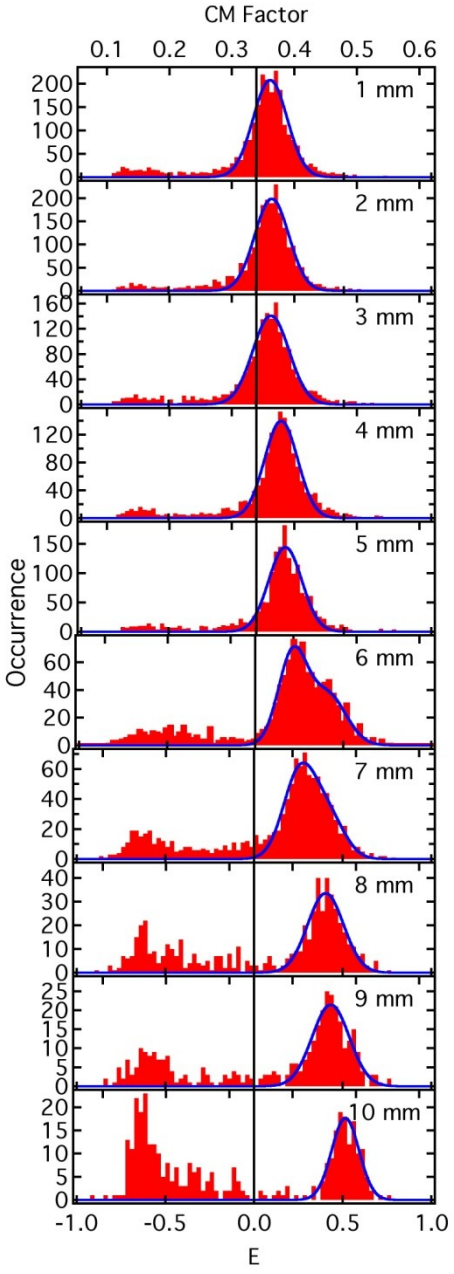

Figure 5.6 Distribution of unique single molecule emission ratios, E (bottom axes), and CM factors (top axes) as a function of position along the gradient, running between the high-phenyl (1 mm) to low-phenyl (10 mm) ends. The solid lines show fits of the data to Gaussian functions.

The peak at E < -0.2 is due to impurities. Emission from Nile Red is very weak in polar TMOS derived films increasing the visibility of the impurity spot distribution. Their contributions to the data are actually invariant across the gradient.

The data employed in preparing these histograms were also selected based on signal-to-noise concerns. Specifically, only those molecules producing spots with a peak signal level (in each image) equivalent to 1.5 times the background noise or larger were included in the analysis. The mean square error was also calculated during fitting of the spots to Gaussian functions. These values were used to eliminate spots that could not be properly fit due to the presence of other nearby spots.

Initial inspection of the histograms shown in **Figure 5.6** reveals they are comprised of at least two distinct distributions, one having mean E < 0, the other, mean E > 0. The peak found at E < 0 is readily attributed to impurity spots. This same distribution appeared when blank gradients (absent Nile Red) were imaged and analyzed as described above (data not shown), while the E > 0 distribution disappeared under these same conditions. As a result, data falling within the low E distribution (specifically, those with E < -0.2) are excluded from further analysis and discussion. The cutoff employed was selected so that the entire distribution with mean E > 0 could be included in the analysis, even at the high-phenyl end of the gradient. Note that the population of unique measurements falling within the E < -0.2 distribution is invariant along the gradient.

The distributions having E > -0.2 represent the polarity-sensitive Nile Red signal. These show a clear monotonic trend towards increasing *average* polarity with decreasing phenyl content along the gradient. Each of these distributions was fit to a Gaussian function to determine its peak position and width. **Figure 5.7** plots these peak positions. At the high-phenyl end of the

gradient, the peak of the distribution is located near CM ~ 0.36 and the full distribution can be fit with a single Gaussian function, suggesting a monomodal distribution of environments is present. However, the standard deviation of the distribution (0.097) is about 30% broader than expected from the measurement error (~ 0.076), based on signal-to-noise issues alone (measurement error calculated as shown in the **Appendix**). The polarity distribution and CM value obtained at the high-phenyl end both closely match those obtained from a uniform PTMOS derived control. A CM factor of ~ 0.36 was also obtained from this control, and the distribution width was somewhat narrower (0.086).

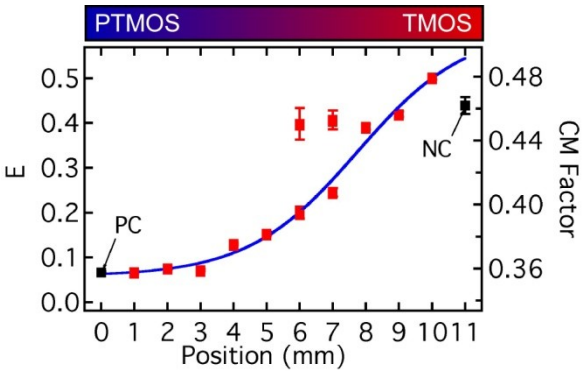

Figure 5.7 Peak positions (symbols) from the Gaussian fits to the histograms shown in Figure 3.6. The histograms at 6 mm and 7 mm were best fit to a two component Gaussian. As a result, two data points are displayed at these positions. Representative values obtained from a uniform PTMOS derived film (positive control, PC) and from a uniform TMOS derived film (negative control, NC) are shown as black squares at 0 mm and 11 mm). The blue line shows a sigmoidal function plotted through the primary series of data points and has been added only to better depict the trend in these data. Deviation of the NC data point from the gradient trend is due to the poor quality of the NC data. Nile Red is very weakly emissive in TMOS derived films.

Proceeding towards the low-phenyl end of the gradient, the peak of the distribution is found to gradually shift to higher CM factors, reaching CM ~ 0.48 at the end of the gradient. Again, this distribution can be fit to a single Gaussian function. The distribution width at the 9 mm position is 0.10, ~ 50% broader than expected (~ 0.068) from the signal-to-noise level. The distribution at the very end of the gradient (10 mm) is much narrower. The data obtained from a uniform TMOS derived control was found to be similar to that at the TMOS end of the gradient, yielding a CM factor of ~ 0.46. However, Nile Red is only very weakly fluorescent in pure TMOS derived films;[75,104] as a result, very few spots were detected in this control and at the low-phenyl end of the gradient. The narrow distribution at the low-phenyl end and the differences between the control and gradient data are attributable to difficulties with single molecule detection in these regions. Nevertheless, the increased breadth of the other distributions, compared to what is expected from measurement noise alone, is consistent with random, nanometer-to-micrometer scale variations in the local polarity along the gradient. As a final caveat, it should be noted that gradient heterogeneity along the depth dimension may also contribute to the observed distribution widths.

In fact, the majority of the distributions shown in **Figure 5.6** could be fit to a single component Gaussian function, consistent with random variation in the local film polarity, such as may arise from random variations in the film composition and/or functional group orientations. However, two key exceptions appear at the 6 mm and 7 mm positions. In these locations, clear evidence of bimodal distributions is found, with two peaks each occurring at CM ~ 0.39 and ~ 0.45 and at ~ 0.41 and ~ 0.45, respectively, as shown in **Figure 5.7**. The data point at 8 mm (see **Figure 5.7**) also appears to deviate slightly from the trend in a manner that is consistent with a small degree of bimodality. These particular distributions reflect non-random variations in the

local polarity and are very likely due to the appearance of TMOS-rich and PTMOS-rich domains in these regions of the gradient. Phase separation has been observed previously by atomic force microscopy[112,113] and by IR microscopy[114] in nongradient organosilane films prepared from binary sol mixtures. In the present studies, the bimodal distributions were manifested as differences in the polarity on lengths scales of several micrometers. Specifically, different distributions were obtained from videos of different (~ 15 μm diameter) film regions. The variations seen in **Figures 5.4, 5.5** suggest some domaining may also occur on much shorter length scales, but these were found to represent minority sites in these other gradient regions and therefore do not make significant contributions to the histograms.

The data and observations presented above yield important new information on gradient composition as a function of position. Along much of the gradient length, the mean polarity varies gradually on a millimeter length scale, suggesting the film composition also changes gradually in a relatively "smooth" manner. The somewhat broadened polarity distributions suggest, however, that the film composition is also variable on nanometer to micrometer distance scales. The appearance of monomodal Gaussian distributions suggests these variations occur by random fluctuations in the film properties, rather than by self-organization (i.e., phase separation) of the film components, although the possibility of phase separation on length scales smaller than the effective spatial resolution (i.e. < ~ 22.5 nm) cannot be discounted. Midway along the gradient, phase separation on longer length scales is suggested by the appearance of bimodal polarity distributions. Since the sol compositions and deposition conditions were selected to avoid visible phase separation in the deposition mixture, it is concluded that any such domain formation likely occurs near the exact time of film deposition. Dip coating has been extensively studied by Brinker and coworkers.[115,116] These studies demonstrate that film

deposition during dip coating occurs in the sol meniscus, due to rapid evaporation of the solvent, along with condensation of the precursor silanes and densification of the gel film. It is in this region where phase separation is most likely to occur. However, domain composition may differ from that expected from well-known models for equilibrium phase separation in binary mixtures.[117] Such differences may arise in sol-gel films because of the rapid, simultaneous occurrence of solvent evaporation and silane condensation. These are expected to trap the domains in distinctly non-equilibrium configurations. Future studies will further address the length scales and compositions of the domains appearing in these and other sol-gel-derived gradients by high-resolution single molecule imaging methods.[72,74,109,110,118]

5.4 Conclusion

In summary, this chapter reports single molecule spectroscopic imaging studies of polarity along a phenyl-modified organosilane thin film gradient. The gradient was prepared by infusion-withdrawal dip-coating using TMOS and PTMOS based silica sols as precursors. The presence of a gradient in the resulting film was verified by water contact angle measurements and by Raman mapping. Two-color single molecule imaging experiments revealed through the observed breadths of the single-molecule-derived polarity distributions that the film polarity varied randomly on nanometer to micrometer distance scales. Quantitative estimates of the local polarity (via the Clausius-Mossotti factor) were obtained from the single molecule results. Ensemble distributions compiled from the single molecule data revealed the presence of a centimeter-scale gradient running down the film that largely exhibited smooth, monotonic variations in polarity. However, bimodal distributions were found midway along the gradient, consistent with phase separation of the polar and nonpolar film components in these regions.

Gradients incorporating phase-separated domains will exhibit properties that differ greatly from those comprised of molecularly-mixed materials. In particular, the presence of such domains will alter both the partitioning and adsorption phenomena important to stationary-phase-gradient chromatography[35] and will also limit gradient utility for guiding the motions of liquid droplets,[12] macromolecules,[119] vesicles and cells.[120]

Chapter 6 - Single Molecule Perspective on Mass Transport in Condensed Water Layers over Gradient Self-Assembled Monolayers

6.1 Introduction

The self-assembly of organosilane monolayers (SAMs) on oxides and other substrates provides a valuable route to the control of surface wettability, lubricity, adhesion and biocompatibility for the design of surfaces with applications in diverse fields such as molecular electronics, optics, bio/chemical sensing and model biological membranes. However, the properties of such surfaces are not entirely defined by the chemical composition of the SAMs alone. For example, when these materials are exposed to the ambient atmosphere, a layer of water rapidly condenses onto their surfaces. This condensed water layer can dramatically alter the surface properties. While a wide variety of organosilanes is now available, allowing for the macroscopic surface wettability to be tuned from hydrophilic to hydrophobic, even hydrophobic surfaces are at least partially covered by a thin (nanometer-thick) water layer under all but the driest conditions.[121-124]

The structure of these thin water layers has been extensively studied by infrared spectroscopy,[121,125-127] X-ray and neutron reflectometry[122,128,129] and by surface selective

nonlinear optical methods.[130,131] Theoretical studies have also contributed valuable insights into water layer coverage, thickness, organization and morphology.[123,132,133] Infrared spectroscopy studies have shown that nanoscale water layers on silica surfaces evolve from ice-like to liquid-like water as the ambient RH increases from low to high values.[125] Atomic force microscopy (AFM) and the surface forces apparatus have been employed to measure the viscosity of water layers on modified and unmodified surfaces.[134,135] The viscosity of the water layer on hydrophilic silica was found to be high by AFM, while values closer to that of bulk water were obtained on a hydrophobic surface.[134] Other studies have reported on the heterogeneity of water layers condensed on SAM surfaces.[124] Generally, water layers are found to be thin and relatively uniform on hydrophilic surfaces but collapse to form tiny droplets on hydrophobic surfaces.[123] The latter are often associated with SAM film defects.

While significant progress has been made towards understanding the structure of condensed water layers on SAM surfaces,[136] much remains to be learned about the diffusion of analytes, reagents, or contaminants within them. Importantly, mass transport mechanisms and rates are expected to vary in a complex fashion with water layer thickness, continuity, structure and viscosity, all of which depend upon the nature of the SAM surface and the ambient RH. Relatively homogeneous water layers formed over hydrophilic surfaces may yield homogeneous diffusion, but the tendency of such layers to form ice-like assemblies[137,138] suggests their viscosities will be high. In contrast, hydrophobic regions, for which the water layers are comprised of tiny droplets of bulk-like water, are expected to allow for fast diffusion, but with motion confined by the spatial extent of the droplets. Reagent/analyte interactions with the SAM surface also play a role in governing mass transport, with polar, hydrogen-bonding species

interacting most strongly with hydrophilic surfaces and nonpolar species interacting most strongly with hydrophobic surfaces.

The investigation of mass transport near SAM surfaces in the presence of just a few monolayers of water requires the use of methods that are sensitive to in-plane (2D) molecular diffusion and surface adsorption/desorption phenomena. These methods must also afford spatial resolution sufficient to resolve any variations in the local molecular mobility caused by heterogeneity in the water layer. Fluorescence recovery after photobleaching[139] is suitable for such studies, but may be difficult to apply in cases where significant spatial heterogeneity exists. Fluorescence correlation spectroscopy, as performed in a confocal (single point) configuration,[140] could also be employed, as could imaging correlation spectroscopy methods,[141] but each requires trade-offs in either time resolution or accessible imaging area.

Single molecule tracking (SMT) represents a viable alternative that is well suited to such studies.[142,143] SMT has been widely employed to explore both the mechanisms and rates of molecular diffusion in gels[144,145] and thin films,[77,146-149] and for a variety of solid-liquid interfaces.[142,143,150-152] In SMT, the sample is broadly illuminated by laser light that excites well-separated fluorescent probe molecules doped into the films at nanomolar (or lower) concentrations. Videos of the molecules moving in/on the sample are then recorded. The individual molecules produce bright round fluorescent spots in each video frame. These spots are subsequently detected and linked into trajectories that are then used to quantify molecular mobility. Single molecule diffusion coefficients are frequently determined by plotting the mean square displacement (MSD) of the molecules as a function of time,[153] or by constructing and fitting the distribution of step sizes taken by the molecules between sequential video frames.[149] Molecules exhibiting homogeneous Fickian diffusion generally produce linear MSD plots where

the slope is proportional to the diffusion coefficient, and step size distributions with Rayleigh-like profiles.[149] Non-Fickian diffusion leads to easily observable deviations from these behaviors.

Investigations of mass transport over SAM surfaces might normally involve preparation of a large number of uniformly modified surfaces having a range of compositions. These SAMs would then be exposed to different environments and the motions of the molecules recorded for each sample. An alternative to such a lengthy series of experiments is to prepare a gradient SAM having a range of compositions along a single substrate.[2-4] In this manner, the effect of SAM composition on wettability, the properties of the condensed water layer and single molecule mobility can be explored in a high-throughput manner.[78] Several recent reviews provide detailed information on the preparation, characterization and utility of synthetic chemical gradients.[2,3,78]

This chapter reports the application of SMT to studies of mass transport rates and mechanisms in nanometer-thick condensed water layers over SAM gradient surfaces. Results were obtained as a function of surface chemical composition and ambient RH. Gradient SAMs were prepared by vapor phase deposition[12] of hydrophilic 3-cyanopropyltrichlorosilane (CN) and hydrophobic octyltrichlorosilane (C8) precursors onto silica and silicon substrates. The CN and C8 precursors were deposited from opposite ends of the substrate, producing "opposed" two-component gradients[5,51,154-156] with variations in the CN and C8 coverages running in opposite directions along the surface. Static water contact angle (WCA) measurements were employed to verify gradient formation, and to obtain quantitative data on their macroscopic wettability as a function of position. Measurements of film thickness along the gradients were acquired by spectroscopic ellipsometry. These data also provided evidence of a spatially variable layer of water condensed on the gradient surface. The microscopic structure of these water layers was assessed by tapping mode atomic force microscopy (AFM). For SMT studies, a fluorescent

perylene diimide dye [N,N'-bis(octyloxypropyl)-perylene-3,4,9,10-tetracarboxylic diimide] (C_{11}OPDI, Figure S1) was used as the probe molecule and was loaded into the films at nanomolar concentrations. The SMT results depict a general trend towards increasing dye mobility with increasing RH and increasing surface wettability. These studies also provide evidence that dye molecule diffusion involves both Fickian and desorption-mediated (Levy) mechanisms and that the relative contributions of these mechanisms depend upon surface wettability and ambient RH.

6.2 Experimental Considerations

6.2.1 Sample Preparation

Deposition of silica base layer. Previous studies have demonstrated that organosilane gradients best adhere to the substrate when deposited on a silica base layer.[8,19] Therefore, both the silica and silicon substrates used in these studies were first coated with a tetramethoxysilane (TMOS) based sol. This base layer also affords similar surface chemistries on both substrates, helping to ensure the gradients obtained are of similar nature. The TMOS sol was prepared by mixing TMOS (99%, Sigma-Aldrich), ethanol (200 proof), high purity water (18 MΩcm, Barnstead B-pure) and HCl (0.1 M) in a 1:125.8:22.1:0.04 (TMOS:ethanol:water:HCl) molar ratio in a clean glass vial. The mixture was stirred for 1 h and stored in a desiccator for 23 h prior to use. Each substrate was cleaned in an air plasma for 5 min. before base-layer deposition. The base layer was formed by spin casting (5000 rpm, 30 s) a 150 µL aliquot of the aforementioned sol onto the substrate. All base layers thus obtained looked optically clear and uniform by eye.

Preparation of gradient self-assembled monolayers. All gradients were prepared by room-temperature vapor-phase deposition (VPD) of polar and nonpolar organosilanes. The organosilanes employed were 3-cyanopropyltrichlorosilane (CN-silane) and octyltrichlorosilane (C8-silane), both obtained from Sigma-Aldrich. Both were of 97% purity and were used as received.

A diagram of the apparatus used for VPD is shown in **Figure 4.3 (a)**. It consists of a substrate supported on a platform, with the substrate positioned midway between two reservoirs designed to hold the precursor organosilanes. These components were all housed inside a plexiglass box. The box allowed for VPD of gradients in the absence of air currents and under controlled humidity. The humidity inside the chamber was maintained at 60 ± 2% RH for all depositions. The two reservoirs each comprised a single 3 mm X 20 mm slit cut into a glass slide. The edge-to-edge separation between each reservoir and the substrate was maintained at an experimentally optimized distance of 5 mm in all depositions.

Each base-layer-coated substrate was treated in an air plasma for 2 min immediately prior to its insertion in the deposition chamber. The two reservoirs were then loaded with a mixture of paraffin oil (200 μL) and one of the two organosilanes (50 μL). The CN-silane was loaded first and was immediately followed by loading of the C8-silane. The inlets were promptly closed and the substrate was exposed to silane vapor for 5 min. This exposure time was determined to yield optimal results after extensive experimentation. The substrate was immediately removed from the chamber after film deposition. The resulting gradient SAM films looked optically clear and clean by eye. Each film was then stored in a desiccator under static vacuum for 12 h. These were subsequently spin coated (5000 rpm, 30 s) with a 150 μL aliquot of 4 nM C_{11}OPDI dye shown in **Figure 4.4** (synthesized in house)[157,158] in HPLC grade ethanol. After coating with dye, each

gradient was stored in a desiccator for an additional 48 h before characterization by SMT and other methods.

6.2.2 Gradient Characterization

Static water contact angle measurements. Sessile drop WCAs were measured using a home built instrument. Droplets of high purity water (1.0 μL) were placed along the gradient using a microliter syringe. Images of the droplets were acquired with a CCD camera attached to a Navitar zoom lens. The images were analyzed using a routine available for the ImageJ software package.[159] WCAs were measured at a separation of 3 mm along each gradient. Each measurement was replicated three times across the gradient at separations of 2 mm. All measurements were made under ambient lab conditions (30 ± 5% RH, 21.1 ± 0.6 ^{o}C).

Film thickness measurements. Film thicknesses were measured by spectroscopic ellipsometry (α-SE, J.A. Woollam). For these measurements, gradient SAMs were prepared on base-layer-coated silicon substrates. For each sample, the base-layer thickness was determined first, prior to deposition of the gradient. The gradient thickness was subsequently measured after deposition and storage in a desiccator, as described above. Both the base-layer and gradient thicknesses were measured under 16% RH. Finally, the gradients were exposed to 65% RH (and 95% RH) and the thicknesses were again measured. All measurements were made at the same series of positions (to within ±1 mm) in each case (base layer alone, gradient at 16% RH, gradient at 65% RH) to allow for determination of the SAM film and water layer thicknesses.

Atomic force microscopy. The surface morphology of the SAM gradients and the condensed water layer were studied using a Veeco Dimension Icon AFM with a NanoScope V controller. Imaging was performed in tapping mode using a microfabricated silicon cantilever

(40 N/m, Veeco, Santa Barbara, CA) in air, under humidity controlled at 25%, 55% and 70% RH. The set point ratio $R_{sp} = A_{fb}/A_0$, where A_0 is the free oscillation amplitude with the tip far from the sample surface and A_{fb} is the oscillation amplitude in feedback, was maintained at a value of 0.95 during imaging. Images were analyzed using the NanoScope software (v1.40). All AFM images reported were acquired on SAM-coated silicon substrates, but gradients on base-layer-coated silica substrates yielded images that were indistinguishable from those on base-layer-coated silicon.

Optical microscopy. All SMT experiments were performed on an inverted wide-field fluorescence microscope as shown in **Figure 4.8b** in **Chapter 4**. In these experiments, each sample was mounted over a high numerical aperture (NA) oil immersion objective (Nikon Apo TIRF, 100X, 1.49 NA) that was used for both sample illumination and collection of the resulting fluorescence. Blue light (488 nm) from a diode laser was used for excitation of the C11OPDI dye doped into the films. The excitation power was maintained at 100-125 μW in all experiments, yielding average excitation intensities of ~56-70 W/cm2. The fluorescence was detected using a CCD camera (Andor iXon DU-897). Fluorescence videos 450 frames in length were recorded for each location on the sample at a rate of 2 frames/s. Videos were acquired from a total of 70 distinct locations along each gradient at 1 mm spacings in each dimension. The fluorescent spots produced by the single molecules in each video frame were detected, fit to 2D Gaussian intensity profiles, and linked into trajectories using a LabView-based particle-tracking program written in-house.

6.3 Results and Discussion

6.3.1 Gradient Wettability. The macroscopic wettability of each gradient was probed by measuring the static WCA as a function of position. **Figure 6.1** shows the average WCA values obtained along one gradient. The WCA was found to increase from the hydrophilic CN end (0 mm) to the hydrophobic C8 end (25 mm), as expected, for all SAM gradients prepared under the conditions specified above. The relatively small error bars, in comparison to those of previous gradient films,[8] reflect the reduced roughness and improved homogeneity of VPD gradients.

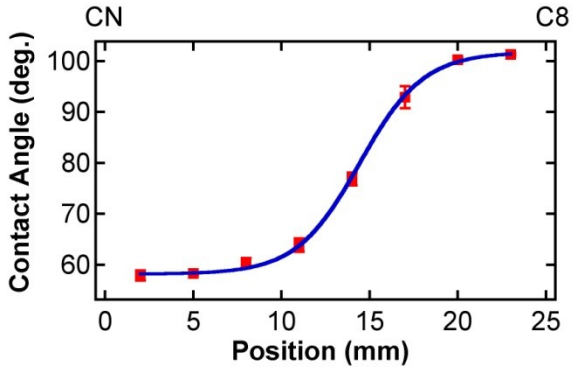

Figure 6.1 Representative static WCA data obtained along a CN-C8 gradient SAM. Each data point on the graph represents the average of three values measured across the film at three different positions. The error bars depict the standard deviation of these measurements. The solid blue line has been added to better show the trend.

6.3.2 Gradient and Condensed Water Layer Thickness. Measurements of film thickness were made along the length of the silica base layer and the gradient SAMs under both dry and humid conditions. The base layer was found to be uniform with a thickness of 25.5 ± 0.5 nm (data not shown), when measured under dry conditions (16% RH). **Figure 6.2** plots the SAM film thickness for dry (16% RH) and humid (65% RH) conditions. Due to instrumental limitations, film thickness data could only be obtained from the central ~20 mm of the gradient length. At 16% RH, the gradient SAM thickness ranged from a maximum of ~3.4 nm at the CN

end to ~1.1 nm at the C8 end. A single monolayer of well-packed C8-silane should yield a thickness of ~1.1 nm, while a CN-silane film should be thinner (~0.8 nm), assuming both are oriented perpendicular to the surface. The film thickness at the C8 end closely matches that expected for a monolayer. The greater thickness at the CN end could be due to the presence of residual water, even under dry conditions (see below). Cross-linking of the trichlorosilane precursors may also lead to formation of a multilayer film.

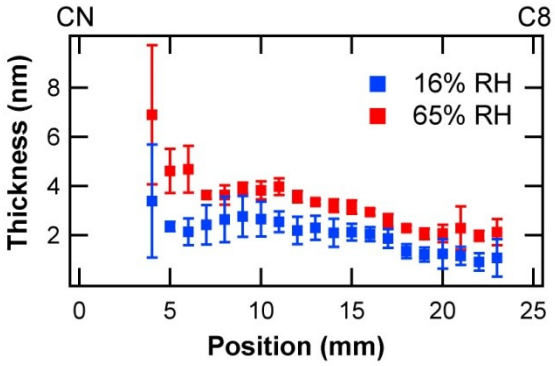

Figure 6.2 Film thickness along a CN-C8 SAM gradient on a base-layer-coated silicon substrate. The measurements were made under dry (16% RH) and humid (65% RH) conditions.

Upon exposure of the SAM gradient to higher humidity (e.g., 65% RH, for ~ 8 h), the apparent thickness of the film was found to increase at all points (see **Figure 6.2**). This increase in film thickness is attributable to condensation of water on the gradient SAM surface and/or swelling of the film. Unfortunately, it is not possible to unequivocally distinguish between these two cases at present. The increase in film thickness upon changing from dry to wet (65% RH) conditions ranged from ~ 3.5 nm near the CN end to ~ 0.7 nm near the C8 end. Similar results were obtained at 95% RH (data not shown). While the C8 end of the gradient is hydrophobic (WCA > 100^{o}), it is relevant that condensation still occurs even in this region, as expected from

previous reports.[121,160] The change in thickness at the C8 end corresponds to ~ 3 molecular layers of water, while the change at the CN end is consistent with > 10 water layers.

6.3.3 Structure of SAMs and Condensed Water Layer. Tapping mode AFM was employed to assess the nanoscale morphology of the gradient films, to confirm the presence of the condensed water layer at high RH, and to characterize its spatial heterogeneity. Previous theoretical[160] and experimental[161] studies have shown that water layers condensed on hydrophobic surfaces are often discontinuous, appearing as wet islands associated with film defects.

Representative height and phase images acquired near the CN end at 25% RH are shown in **Figure 6.3**. These show small raised features ~ 10 nm in height and ~ 500-600 nm in width, along with pinholes exhibiting apparent depths of ~ 12-18 nm. These features are attributed to imperfections in both the base layer and the SAM film and are largely unavoidable. The phase images show much weaker contrast for these same film imperfections. However, associated with these features are relatively larger (~ 0.7-1.5 μm diameter), nominally round regions where the phase angle exhibits a subtle decrease (~ 2-3o) from the surroundings. These regions may reflect the condensation of water to form wet "islands" around certain film defects, even at 25% RH. Associated features in the height images produce changes too small for effective measurement.

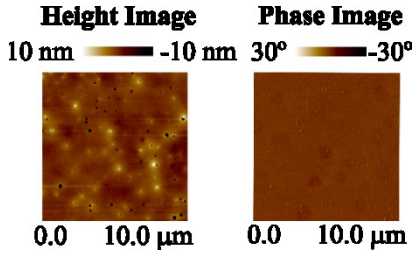

Figure 6.3 Tapping mode AFM images of a gradient sample acquired near the CN end of a gradient, at 25% RH. Height (left) and phase (right) images are shown for identical sample

regions. These data were acquired by Kayesh Ashraf, Virginia Commonwealth University, on sample prepared at Kansas State University.

A series of representative height and phase images acquired along a gradient SAM at 70% RH are shown in **Figure 6.4**. Similar results were obtained at 55% RH (data not shown). While these particular images were acquired from a gradient supported on base-layer-coated silicon, images obtained from gradients on base-layer-coated silica were indistinguishable.

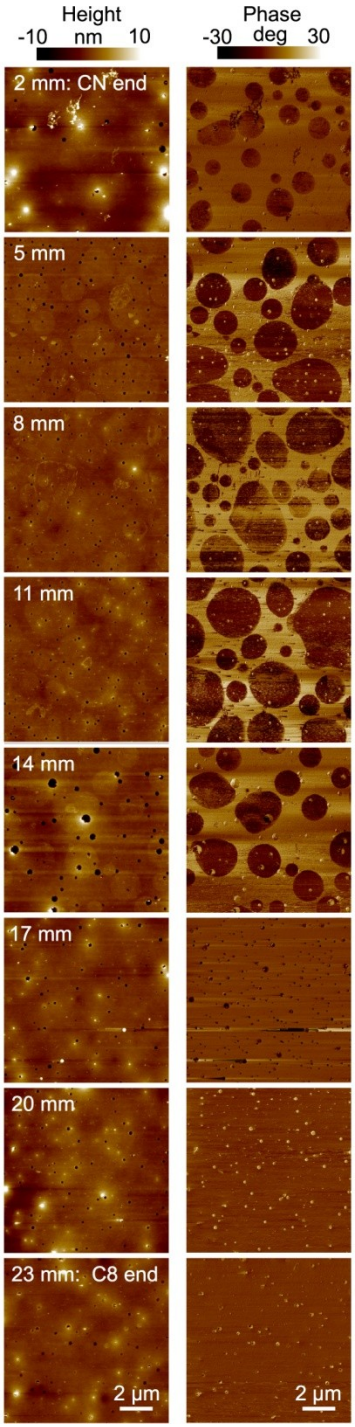

Figure 6.4 Representative tapping mode AFM height (left column) and phase angle (right column) images obtained as a function of position along a CN-C8 SAM gradient at 70% RH. The pairs of height and phase images show identical sample regions. These data were acquired

by Kayesh Ashraf, Virginia Commonwealth University, on sample prepared at Kansas State University.

These images provide additional evidence of the film imperfections described above, and demonstrate they appear along the full length of the gradient. More importantly, they provide clear evidence for the formation of wet "islands" due to water condensation on the gradient surface. These islands appear as nominally round regions of greater topographic height (i.e., < 0.5 nm to ~ 2 nm, from line profiles), and decreased phase angles (i.e., exhibiting a change of 10-20^{o}) from their surroundings as shown in **Figure 6.5**. They were found mainly from near the hydrophilic CN end to the midpoint of each gradient and were conspicuously absent nearest the hydrophobic C8 end. The islands also exhibited a clear increase in contrast[162] and size in the phase images with increasing relative humidity (compare **Figure 6.3** to **Figure 6.4**), when images acquired at similar positions near the CN end of the gradients are compared.

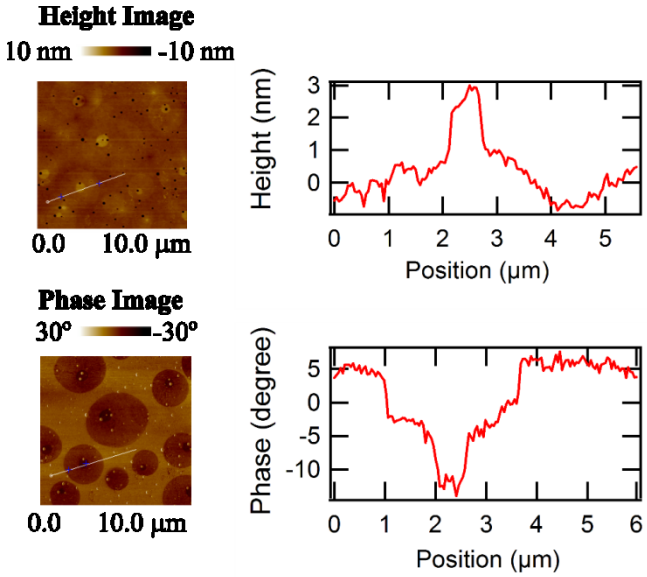

Figure 6.5 Tapping mode AFM images and line profiles acquired ~ 2 mm from the CN end of a gradient sample. The images were acquired at 55% RH. Top) Height image and corresponding line profile, as defined by the white line on the image. Bottom) Phase image and corresponding line profile, as defined by the white line on the image. The two images depict identical sample regions. These data were acquired by Kayesh Ashraf, Virginia Commonwealth University, on sample prepared at Kansas State University.

The absence of wet islands in images recorded near the C8 end likely reflects a change in the morphology of these islands. Again, the ellipsometry data show that water is present at the C8 end of the gradient. Nearer the CN end, they appear to be generally flat, covering relatively large surface areas. Proceeding towards the C8 end, the islands appear to shrink in size prior to disappearing. The latter is consistent with a transition to hemispherical droplets over hydrophobic film regions. These may better wet the AFM tip and/or move around with it over the most hydrophobic regions, making them effectively "invisible". In contrast, the wet islands

found near the hydrophilic CN end were very stable, exhibiting no evidence of movement or changes in size across multiple images acquired over periods of 30 min (data not shown).

6.3.4 Fluorescence Imaging and Single Molecule Tracking. The role of the condensed water layer in governing molecular mobility along the SAM gradients was explored by wide-field fluorescence video microscopy and single molecule tracking (SMT). For this purpose, fluorescence videos were acquired from a total of 70 distinct positions along each gradient under three different ambient humidities (16%, 65% and, 95% RH). **Figure 6.6** presents a pair of static images compiled from representative videos obtained near each end of the gradient and at 16% and 95% RH, respectively. The insets in **Figures 6.6A,B** depict cropped regions of single video frames, while the full size images were compiled by plotting the maximum fluorescence signal detected at each pixel across the full video length.

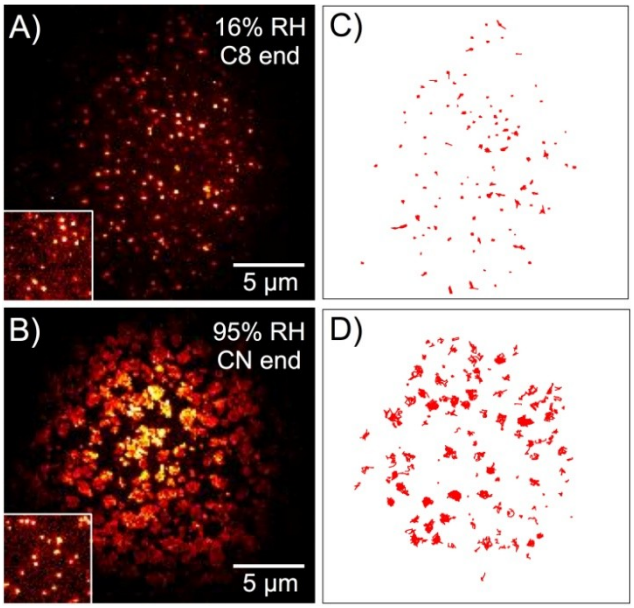

Figure 6.6 A), B) Images and **C)**, **D)** trajectories obtained for C_{11}OPDI dispersed on the SAM gradients at 16% RH (**A and C**) near the C8 end of the gradient and at 95% RH (**B and D**) near the CN end. **A)** and **B)** show the maximum fluorescence signal detected at each pixel across the full 450 frames comprising each video. The insets show single frame data, cropped from the center of each. **C)** and **D)** show the trajectories obtained from the same videos. The scale bars apply to all images, insets and trajectory plots.

Single frame images (insets in **Figure 6.6**) show that the video data are comprised of well-spaced fluorescent spots of diffraction-limited size. These spots depict the emission from single C_{11}OPDI molecules. Although C_{11}OPDI is known to form aggregates (particularly at higher concentrations), any such species would not be detected here as their emission is red-shifted from that of the monomer[163] to wavelengths outside the detection bandwidth (i.e., 535 ± 25 nm) and their luminescence quantum yield is greatly reduced.[157,164] By comparing the single frame images to the compiled maximum-signal images (**Figure 6.6**), it is apparent that some of the molecules are mobile while others remain fixed for long periods of time. Single molecule

mobility is strongly dependent upon position along each gradient, and on ambient RH. The molecules are generally less mobile near the C8 end of each gradient and more mobile near the CN end (see below for details). Likewise, few molecules appear to be mobile under dry (16% RH) conditions, while many more become mobile with increasing humidity.

The compiled maximum signal images provide strong evidence that molecular mobility occurs within the aforementioned wet regions of the gradient (**Figure 6.6B**). Especially at high RH and near the CN end, the mobile molecules appear to be restricted to round "islands" on the surface. However, these islands appear smaller in size than observed by AFM (compare **Figures 6.4 and 6.6B**). This size difference arises partly from the finite length of time over which individual molecules can be tracked prior to photobleaching. The immobile molecules (**Figure 6.6A**) are likely entrapped in the film, associated with film defects or otherwise adsorbed on its surface. The characteristics of molecular mobility are explored in greater depth in the following sections.

6.3.4.1 Populations of mobile and immobile molecules. To gain deeper insights into the phenomena governing molecular mobility, automated SMT software was employed to map the pathways followed by each molecule. For this purpose, the intensity profile of each spot was first fit to a 2D Gaussian function, providing its location with precision better than expected from the diffraction limit,[111] and its width. Subsequent linking of the spots was accomplished using a modified cost-functional method.[96]Trajectories ranging in length from two frames up to approximately the full video length were obtained. However, quantitative results on molecular diffusion can only be gleaned from relatively long trajectories.[165] As a result, only those trajectories $\geq$ 10 frames in length were employed in the analyses described below. All others

were discarded. **Figure 6.6C,D** plot these trajectories for the data shown in Figure **6.6A,B**. Inspection of the trajectory data confirms that the molecules are generally less mobile under dry conditions and near the C8 end of the gradient, and most mobile under high humidity and near the CN end of each film.

Variations in the relative populations of fixed and moving molecules and their mobilities were quantitatively assessed by first categorizing each trajectory as representing either a mobile or an immobile molecule. Separation of the trajectories into these two populations was accomplished by comparing the localization precision, σ_r^2, for each molecule, averaged across its full trajectory length, to its approximate mean-square-displacement (MSD) for single-frame steps.[166] The localization precision was explicitly determined from **equation 6.1**.[96]

$$\sigma_r^2 = \frac{s^2}{N} + \frac{a^2}{12N} + \frac{8\pi s^4 b^2}{a^2 N^2} \qquad (6.1)$$

where s^2 is the variance of each Gaussian spot, N the total fluorescence counts detected, a^2 the pixel area and b the background noise. In the present studies, s ≈ 1.28 pixels (160 nm), b ≈ 11.8 counts, a ≈ 125 nm and N varied between spots and video frames. Common values for σ_r ranged from ~ 20 to ~ 28 nm.

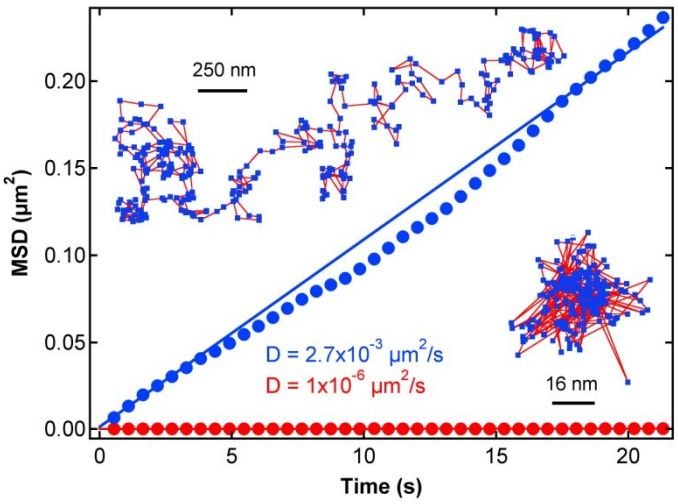

Figure 6.7 Representative single molecule trajectories (insets) and MSD plots for an immobile molecule near the C8 end of a gradient at 16% RH (lower right) and for a mobile molecule near the CN end at 65% RH (upper left), respectively. Their MSD plots are shown in red and blue, respectively. The symbols depict the measured values, the solid lines are fits to the first four points. The apparent diffusion coefficients for the molecules are also given. The scale bars depict distance along each trajectory.

MSD values were determined for each molecule by averaging their frame-to-frame displacements across the full length of each trajectory for different frame delays. These values were then plotted vs. time and the first four points fit to a line to obtain an estimate of the MSD value for single-frame steps. **Figure 6.7** depicts representative trajectories for immobile and mobile molecules, along with their MSD plots. Using data such as these, molecules having MSD $> 3\sigma_r^2$ were classified as mobile, while all others were classified as immobile.

Histograms depicting the full distributions of MSD values from several thousand trajectories, all ≥ 10 frames in length, are plotted as a function of position along each gradient and for the three RH values in **Figure 6.8**. Results from both immobile and mobile molecules are

included. The former are shown in red (near zero) and the latter in blue. The populations are plotted on a log scale to better highlight the behavior of the mobile fraction. Inspection of these plots reveals that the distributions are narrowest at 16% RH and much broader for 65% and 95% RH. The distribution widths change little with position at 16% RH. At higher RH, the distributions are generally broader near the CN end (6-9 mm) and narrower near the C8 end (16-19 mm). Broader histograms are consistent with increased molecular mobility.

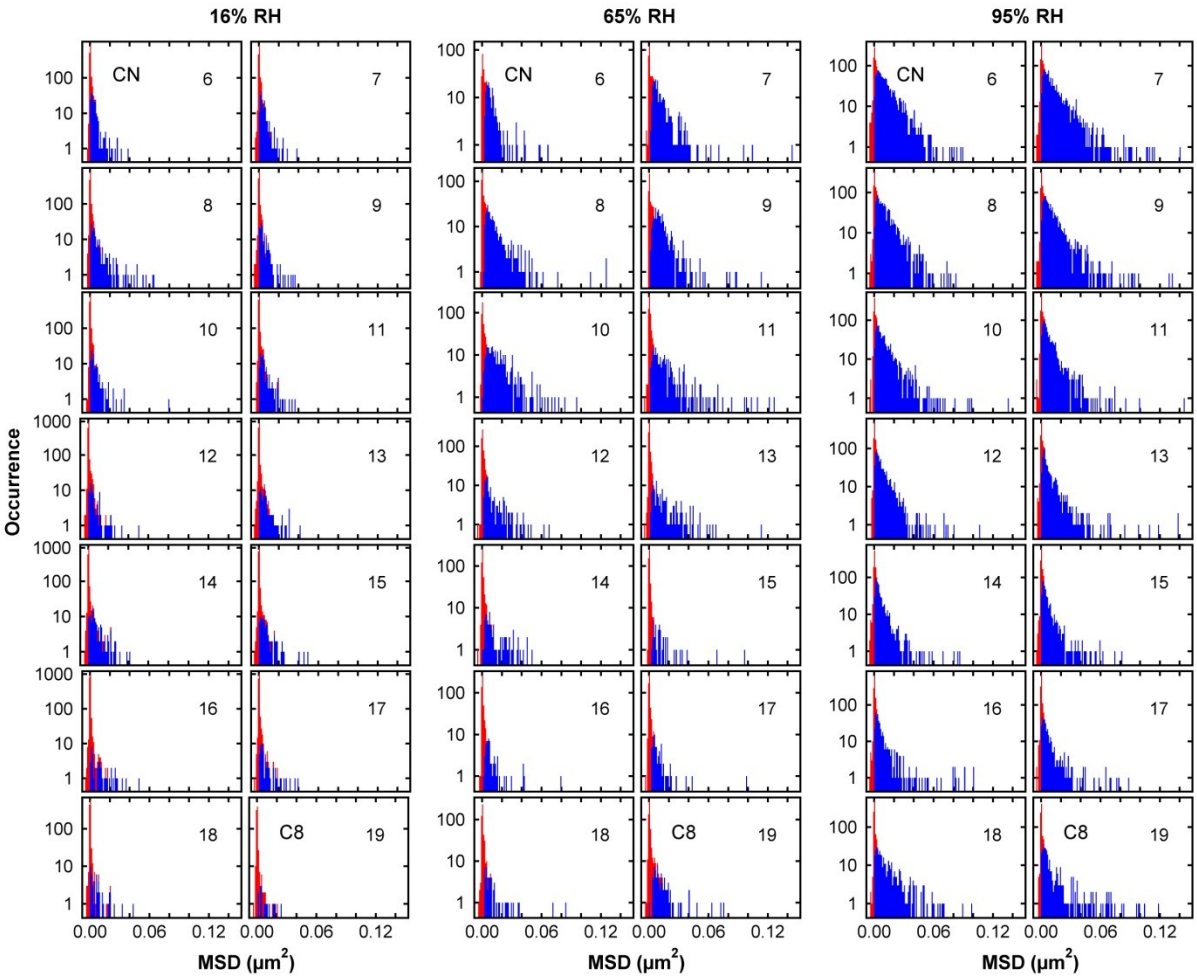

Figure 6.8 Single-frame MSD distributions obtained from the SMT data as a function of both position along the CN-C8 SAM gradients and ambient RH. Each set of distributions depicts results obtained from near the CN end (6 mm) to near the C8 end (19 mm). Images could not be

collected from the first and last ~ 5 mm of each gradient, due to instrument limitations. Each histogram is a compilation of five replicate measurements, with the measurements separated by 1 mm spacing across the sample. The blue bars show the mobile population while the red bars depict immobile molecules. The numbers appended to each distribution designate the position (in mm) along each gradient.

The general increase in molecular mobility along the gradients and with increasing RH may be manifested in different ways, each reflective of the mechanisms that govern molecular motion. For example, greater mobility may result from an increase in the population of mobile molecules. It may also result from an increase in the rate of molecular diffusion. To explore these differences, **Figure 6.9A** plots the fraction of mobile molecules obtained from the data shown in **Figure 6.8**. These results show that < 15% of the C_{11}OPDI molecules are mobile under "dry" (16% RH) conditions at all positions. The greatest population of mobile molecules is found near the CN end, while fewer molecules (< 5%) are mobile near the C8 end. These results demonstrate that, unlike the thicker gradient films investigated in our earlier studies, the SAM films studied here are unlikely to support mass transport on their own, at least under the conditions at which these experiments were performed (16% RH, ~ 21 ^{o}C). The greater population of mobile molecules detected near the CN end of the gradient is attributed to residual water on that end of the gradient (see **Figure 6.3**), even under such dry conditions.

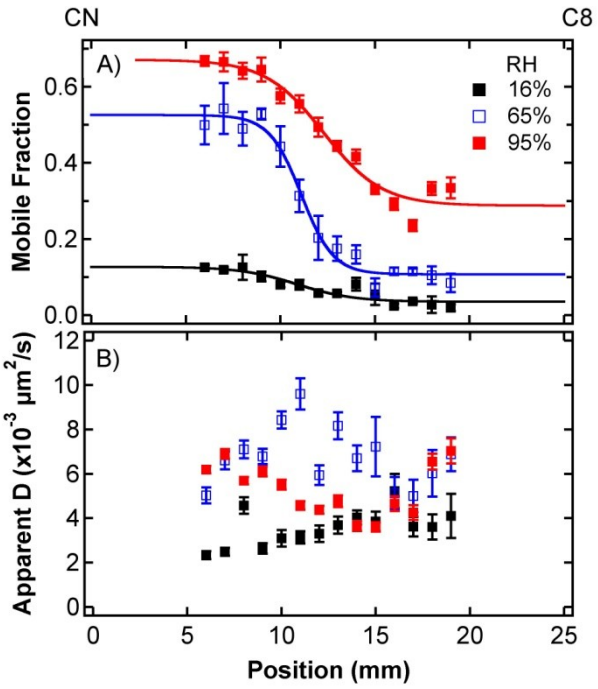

Figure 6.9 A) Mean fraction of molecules classified as mobile as a function of position along each of three distinct CN-C8 SAM gradients under three different RHs. The error bars depict the standard error of the mean from five replicate measurements in each case. The solid lines have been added to better depict the trends in the data. **B)** Mean apparent diffusion coefficient, D, for the mobile fraction as a function of position along each gradient. The error bars depict the pooled standard deviations from five videos in each case. Data are shown for three different ambient RHs, as designated in **A)**.

As the ambient humidity is increased, the population of mobile molecules rapidly increases near the CN end (see **Figure 6.9A**). At 65% RH, > 50% of the detected molecules were found to be mobile near this end of the gradient, while only ~ 10% were deemed mobile near the C8 end. At 95% RH, the fraction of mobile molecules near the CN end further increased to > 65%, while at the C8 end, only ~ 30% were mobile.

The smaller fraction of mobile molecules at the C8 end could reflect enhanced intermolecular interactions between the hydrophobic C_{11}OPDI dye and the hydrophobic C8 alkane tails. It could also be due to differences in the morphology of the water layer covering the surface. Again, the water layer is at least 3 monolayers thick (on average, at 65% RH), even near the C8 end of the gradient. The "flat" wet islands observed at the CN end likely change to hemispherical droplets near the C8 end. The associated reduction in surface area covered by water may be manifested as an equivalent reduction in the population of mobile molecules. Indeed, the AFM phase images (**Figure 6.4**) are consistent with this hypothesis, depicting ~ 56% coverage by water at 70% RH near the CN end and undetectable water (likely present as droplets that wet the AFM tip) near the C8 end. Again, > 50% of the C_{11}OPDI molecules are mobile near the CN end and ~ 10% are found to be mobile near the C8 end at 65% RH.

While many of the immobile molecules found at the C8 end could simply be present outside the water droplets, it is also possible that these molecules are actually mobile but their motions are confined to regions < 2400 nm^2 in size (i.e., MSD < $3\sigma_r^2$ as specified above). In this case, such molecules would be classified as immobile. Unfortunately, we were unable to obtain quantitative information on the spatial extent of confinement from MSD plots. As is well known, nonlinearities in MSD plots derived from relatively short trajectories are difficult to interpret in this manner.[167]

4.3.4.2 Rate of molecular motion. With a change in morphology of the condensed water layer (i.e., from islands to droplets), and expected changes in the interactions of the water and dye molecules with the SAM surface, the rates of C_{11}OPDI molecule motions are also expected to vary with position and humidity. The rate of molecular mobility along each gradient is best

quantified by the apparent diffusion coefficient, D, for each molecule. For simple two dimensional Fickian diffusion, D is directly related to the measured MSD, as given in **equation 6.2.**

$$MSD = 4Dt \qquad (6.2)$$

where t is time. In these studies, D was determined in the short-time limit (see **Figure 6.7**). D values measured from molecules that move over the course of individual video frames must generally be corrected for dynamic positional uncertainties.[168,169] In the present studies, the aforementioned mean spot widths (~ 1.28 pixels) were found to differ by < ~ 1% between immobile and mobile molecules. Therefore, any molecular motions during individual frames were considered to be minimal and no such corrections were applied.

Figure 6.9B plots the arithmetic mean of the D values obtained from the mobile population of molecules in **Figure 6.8**. These results depict a seemingly very complex dependence of D on both gradient position and ambient RH. The 16% RH data yields the smallest D values along much of the gradient. However, these same data also exhibit a clear increase in D running from the CN end to the C8 end (black squares in **Figure 6.9B**). Note that this trend is in opposition to that observed for the population of mobile molecules, which was smaller at the C8 end (**Figure 6.9A**). While the origins of this difference are uncertain at present, it may reflect a gradual reduction in the viscosity of the water layer condensed over hydrophobic regions of the gradient.[134] It may also arise from increased confinement of the molecular motions to smaller wet regions towards the C8 end.

As the humidity is increased to 65% RH, the *D* values along the full length of the gradient are generally larger, as might be expected from literature reports of transitions from ice-like to liquid-like water on hydrophilic surfaces, with increasing RH.[125,142] However, the spatial dependence in *D* is no longer monotonic and instead exhibits an initial increase with distance from the CN end, followed by a subsequent decrease towards the C8 end (blue squares in **Figure 6.9B**). When the humidity is further increased to 95%, the *D* values obtained are somewhat smaller (on average) than those at 65% RH and also appear to exhibit a different trend with position. While these trends are difficult to explain, they may arise from a variety of effects including variations in 1) the nature of the condensed water layer from ice-like (or structured) to liquid-like,[125,137,138,142] 2) the spatial extent of confinement due to changes in wet-island morphology, and 3) the mechanisms governing mass transport at different positions and RH values. The latter possibility is explored in more detail, below.

6.3.4.3 Mechanistic insights into single molecule diffusion. In the majority of SMT studies of diffusion in thin films reported to date, the data have been analyzed under the assumption that molecular motion follows a Fickian mechanism, with the MSD increasing linearly in time (see **equation 6.2**). However, molecular motion at interfaces and on surfaces may also (or instead) involve a desorption-mediated diffusion mechanism that mimics Levy processes.[142,170-173] The desorption-mediated diffusion mechanism differs from Fickian diffusion in that the molecules are largely immobile on the sample surface and only become mobile when they briefly desorb into the neighboring solution. The molecules then quickly readsorb to the surface. The diffusion time steps in this case are exponentially distributed, producing clear changes in certain characteristics of molecular motion.

Evidence for the participation of both Fickian and desorption-mediated diffusion mechanisms was obtained by further analysis of the SMT data. While MSD plots (see **Figure 6.7**) are expected to be linear in time for Fickian diffusion, they exhibit a super-diffusive $t^{3/2}$ dependence for desorption-mediated diffusion.[170-172] Unfortunately, such behavior is often masked by nonidealities in the MSD plots due to statistical uncertainties brought about by finite trajectory lengths or the history of molecular motion along each trajectory.[149,167] **Figure 6.7** depicts some of this complexity as the MSD plot for the mobile molecule deviates from linearity at longer times.

More clear evidence for Fickian and desorption-mediated diffusion was obtained by plotting single-frame step size distributions for the individual trajectories. Fickian diffusion is expected to produce step sizes with a Rayleigh-like population distribution.[149]

$$P(r,t) = A\left(\frac{r}{2Dt}\right) exp\left(-\frac{1}{2}\left(\frac{r^2}{2Dt}\right)\right) \quad \textit{(Fickian Diffusion)} \qquad (6.3)$$

Here, A is a fitting constant, t is the measurement time (in this case, the frame time was 0.547 s), and r is the step size (absolute value). In contrast, desorption-mediated diffusion produces a population distribution characterized by a Cauchy-like function (in two dimensions)[170-172]

$$P(r,t) = \frac{Actr}{(r^2+(ct)^2)^{3/2}} \qquad \textit{(Desorption-Mediated Diffusion)} \qquad (6.4)$$

with $c = \sqrt{D/\tau}$, in which τ is the "retention time" of molecules on the surface, A is a fitting constant and r is again the step size.

Figure 6.10 plots trajectories and step-size distributions for three representative mobile molecules. Molecules following a desorption-mediated diffusion mechanism are expected to exhibit a characteristic tail to large step sizes that is absent for Fickian diffusion.[170-172] Comparison of the three data sets shown in **Figure 6.10** reveals that the distributions in **Figures 6.10B,C** incorporate these long tails, while **Figure 6.10A** does not. Note that it is not possible to track C_{11}OPDI molecules diffusing through bulk water (D > 100 $\mu m^2/s$) under the present conditions. However, for very thin (a few nm thick) films of water, the long step sizes are believed to be produced by brief excursions into the water layer, followed by rapid readsorption to the SAM surface.[170-172] The very short time spent in the water makes the step sizes sufficiently short such that tracking of the molecule is still possible. In regions with thicker water layers, particularly long excursions may lead to termination of certain trajectories and a corresponding reduction in the population of long steps. A less commonly noted characteristic of desorption-mediated diffusion is that it should also produce a much greater population of short step sizes, leading to a shift in the peak of the distribution to smaller values. Again, comparison of the three data sets in **Figure 6.10** shows that panels **B** and **C** also incorporate relatively more short steps, as expected. As a caveat, it should be noted that both short and long steps might also be produced by molecules exchanging between ice-like and liquid-like layers of water.[125,142] It is not possible at present to conclusively discount this possibility. However, as the hydrophobic dye appears to interact more strongly with the hydrophobic end of the gradient, the desorption-mediated mechanism is concluded to be most likely.

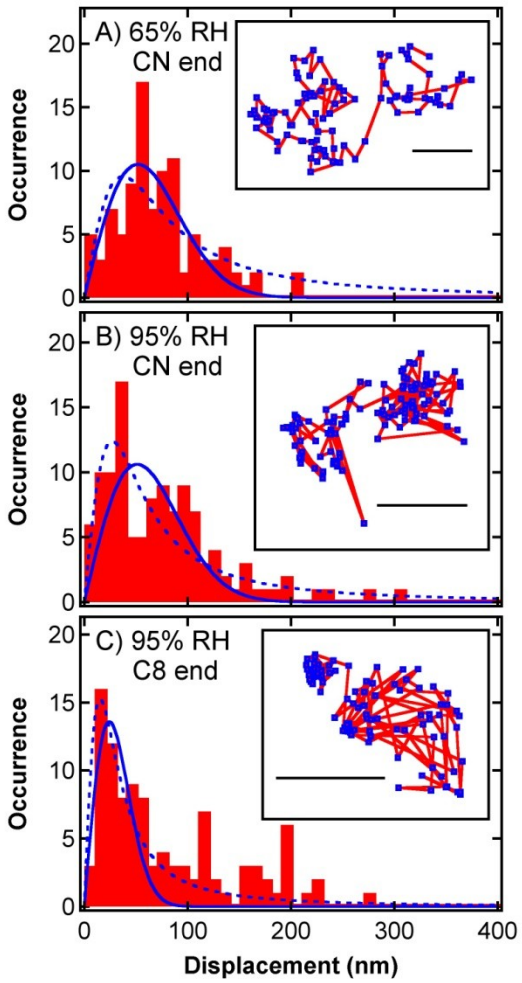

Figure 6.10 Representative single molecule trajectories (insets) and step size distributions obtained from these trajectories for **A)** a single molecule near the CN end of a gradient at 65% RH, **B)** another near the CN end at 95% RH and **C)** a third near the C8 end at 95% RH. All scale bars are 250 nm in length. The blue lines depict fits to **equations 6.3** and **6.4** in each case as solid and dashed lines, respectively. The results are attributed to Fickian diffusion in **A)** and desorption mediated diffusion in **B), C)**.

For a more quantitative assessment of the diffusion mechanism, each step-size distribution was fit to both **equations 6.3** and **6.4** and the best fitting model was used to assign the dominant mechanism (either Fickian or desorption-mediated diffusion). Specifically, the fitting equation

that produced the smallest χ^2 was chosen as the most appropriate model. In this case, only those trajectories ≥ 30 frames in length were analyzed as shorter trajectories contained too few steps. From this analysis, **Figure 6.10A** is assigned to Fickian diffusion while **Figures 6.10B,C** are classified as desorption-mediated diffusion. It is noteworthy that Ag nanoclusters have also recently been reported to exhibit desorption-mediated (i.e., "stick-and-slide") diffusion in thin water layers on silica surfaces.[142] In fact, a significant population of molecules in the present studies shows only relatively small differences in χ^2 for the two fitting equations, making the assignment unclear in many cases and possibly consistent with hybrid behavior.

The observation of desorption-mediated diffusion in these studies points to the important role played by dye-surface interactions in governing molecular motion. Hydrophobic interactions between the dye and SAM film are expected to be most prevalent near the C8 end of the gradient, and at high RH, where there is appreciable water on the gradient surface. Therefore, desorption-mediated diffusion is expected to be more common under these conditions. Indeed a clear trend towards increased contributions from the latter (at > 99.99% confidence) is found near the C8 end of the gradient at 95% RH. **Figure 6.11** plots these results. Unfortunately, the population of mobile molecules was too small to obtain detectable trends at 16% and 65% RH, particularly towards the C8 end of the gradient (data not shown). Due to broadening of the ensemble distributions (data not shown), no attempt was made to use these results to quantitatively assess the contributions from each mechanism.

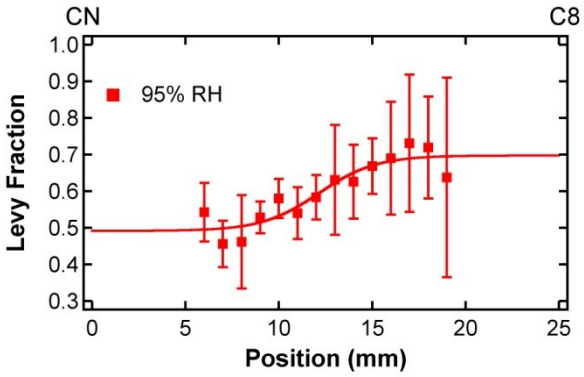

Figure 6.11 Mean fraction of mobile molecules classified as exhibiting desorption-mediated (Levy) diffusion as a function of position along a CN-C8 SAM gradient at 95% RH. The error bars depict the standard deviation from five replicate videos in each case. The solid line was added to better depict the trends in the data.

The change in mechanism from Fickian to desorption-mediated diffusion provides a possible explanation for at least some of the complex, non-monotonic trends in apparent *D* values shown in **Figure 6.9B**, as a function of position and ambient RH. Specifically, the increased and variable contributions of short and long step sizes for desorption-mediated diffusion makes it difficult to assign a meaningful mean *D* value to the associated molecular motions. With respect to the anomalous reduction in *D* between 65% and 95% RH, this observation is explained by the greater population of short step sizes brought about by increased contributions from desorption-mediated diffusion at 95% RH.

6.4 Conclusion

In summary, this chapter repots the single molecule tracking studies of mass transport in water layers condensed from the ambient atmosphere onto opposed two-component gradient

self-assembled monolayers. The gradient SAMs were prepared by controlled vapor phase deposition of CN- and C8-silane precursors. Ellipsometric measurements showed that the condensed water layer was present along the entire length of the gradient, including at the hydrophobic C8 end. Tapping mode AFM data revealed that the water layer was heterogeneous, being comprised of micrometer-sized wet islands surrounded by "dry" regions near the CN end. The presence of water could not be detected by AFM at the C8 end, possibly indicating a transition from wet islands to hemispherical droplets of water.

Single molecule tracking experiments were used to investigate the diffusion of a hydrophobic C_{11}OPDI probe dye on the gradient surface, in the presence of the condensed water layer. These results demonstrated that the water layer facilitated dye diffusion. The population of mobile molecules was found to increase with increasing ambient RH and with increasing hydrophilicity along each gradient. The apparent probe molecule diffusion coefficients obtained from the SMT data exhibited complex, non-monotonic trends with position and humidity. Careful analysis of the trajectory data and single-frame step size distributions revealed that both Fickian and desorption-mediated (Levy) diffusion mechanisms contribute to the molecular motions. Desorption-mediated diffusion generally became more prevalent with increasing hydrophobicity along the gradient surface at high RH.

An improved understanding of the mechanisms by which molecules move about on SAM-coated substrates, especially when they are exposed to the ambient atmosphere will facilitate their development for use in molecular electronics, optics, bio/chemical sensors, as models for biological membranes, and as a means to control corrosion, friction and surface wear.

Chapter 7 - Molecular Combing of λ-DNA using Self-Propelled Water Droplets on Wettability Gradient Surfaces

Reproduced from Giri, D.; Li, Z.; Ashraf, K.M.; Collinson, M.M.; Higgins, D.A. Molecular Combing of λ-DNA using Self-Propelled Water Droplets on Wettability Gradient Surfaces. Manuscript submitted for publication in ACS Appl. Mater. Interfaces

7.1 Introduction

Surface immobilization, elongation and alignment of DNA are required for a wide variety of genomic and biophysical investigations. Included are optical mapping and DNA barcoding,[174,175] biophysical studies of DNA stability[175,176] and replication,[175,177] and investigations of DNA-protein interactions.[178-180] A number of methods have been developed for manipulating DNA in this manner. These include the use of optical tweezers,[181,182] microfluidic devices,[183] and electrical,[184] magnetic[185] and shear flow[186,187] forces. Of these methods, those based on solution flow are the most easily implemented under general circumstances. Many such procedures build upon the original description of molecular combing,[188] in which DNA molecules are elongated by the receding meniscus of a water film. In the closely related method of dynamic molecular combing,[189] DNA elongation is induced by withdrawing a substrate from a DNA solution. Alternative procedures based on the mechanical manipulation of DNA-containing liquid droplets have also been reported.[190,191] The simplest such method involves depositing a droplet of DNA solution on a hydrophobic surface and allowing the droplet to evaporate.[192] In this case, DNA elongation and alignment occur in the radial direction during droplet evaporation. When alignment of the DNA along a particular direction is required, the surface can be tilted to

induce directional droplet motion and DNA elongation.[193] To date, such methods have largely required the application of an external stimulus (i.e., dipping or tilting of the substrate, or pumping of the solution) to drive solution motion.

In this chapter, the manipulation of DNA molecules using water droplets that move spontaneously along surface wettability gradients is demonstrated. Chemical gradients comprise surfaces or films that incorporate gradually changing chemical and/or physical properties in one or more directions. Comprehensive accounts describing the preparation, characterization and general utility of such gradients can be found in recent reviews.[1-3] Chemical gradients find broad utility in combinatorial materials chemistry,[194] high-throughput screening of surface-molecule interactions,[195,196] and for inducing and controlling the motion of liquid droplets,[12,197,198] cells,[33,199] vesicles[31] and nanoparticles.[27]

Here, wettability gradients are prepared by vapor phase deposition of octyltrichlorosilane and fluorinated octytrichlorosilane.[12] Small droplets of water placed on the hydrophobic end of these gradients spontaneously move towards the hydrophilic end. DNA molecules contained within these droplets are adsorbed on the hydrophobic gradient surface and are also elongated and aligned during droplet motion. The mechanism behind DNA elongation and alignment, the position dependence of adsorbed DNA density, the length of the elongated DNA molecules and their orientations in the film plane are all explored.

The implementation of chemical gradients for the elongation and alignment of DNA may aid in the development of inexpensive, disposable and automated microfluidic[183,200,201] and nanofluidic[202] DNA barcoding devices with applications in the rapid detection and identification of biological contamination. With spontaneous, gradient-driven liquid motion, the pumps usually required to drive solution motion in fluidic devices could be eliminated. Motivation for the

present work comes from previous demonstrations of spontaneous droplet motion on gradient surfaces. Early examples include work by Chaudhury and Whitesides,[12] in which a drop of water was shown to move a few millimeters along a wettability gradient. In later work,[203] a fluorinated silane gradient was used to reduce surface friction and enhance droplet motion.

7.2 Experimental Considerations

7.2.1 Sample Preparation. Surface wettability gradients were prepared by vapor phase deposition (VPD)[12] of appropriate organochlorosilane precursors. VPD was performed under controlled relative humidity (RH ~ 60%), with the precursors deposited onto silica-base-layer coated glass and silicon substrates.[8,43] The details of base-layer coating and gradient preparation are described in **Chapter 4**. Two precursor silanes were used for gradient preparation. These were *n*-octyltrichlorosilane (C8-silane) and a fluorinated *n*-octytrichlorosilane (trichloro-[1H,1H,2H,2H-perfluoro-octyl]silane, F-silane). The C8-silane and F-silane were diluted 1:11 and 1:21, respectively, by volume, in paraffin oil prior to use. VPD involved directional exposure of the substrates to vapor from the C8- and F-silane for 4 min and 3 min, respectively. All depositions were performed in a closed Plexiglas chamber that allowed for VPD in the absence of air currents.

The λ-DNA employed in these studies (48,502 base pairs) was obtained from New England BioLabs. Elongation and alignment of the DNA molecules was explored by wide-field fluorescence microscopy. For this purpose, the λ-DNA was labeled with YOYO-1 (Invitrogen), a fluorescent DNA intercalator.[204] The dye:base-pair ratio in the labeled DNA was 1:15 and was kept low to avoid changes in DNA length caused by the dye.[186] Adsorption of the DNA to the

gradient surface was accomplished by placing 2 μL droplets of 40 pM λ-DNA in 1 mM phosphate buffered saline (PBS) solution (pH = 5.6) on each gradient, near its hydrophobic end. The droplet spontaneously moved towards the hydrophilic end immediately after coming into contact with the gradient surface.

7.2.2 Gradient Characterization. Evidence of film deposition was obtained from sessile drop water contact angle measurements. In these studies, 1.0 μL droplets of high purity water were placed at approximately equally spaced intervals along each gradient. Digital images of the droplets were recorded using a CCD camera attached to a Navitar zoom lens. An ImageJ software routine[159] was used to measure the water contact angle from the images. Previous reports of spontaneous water droplet motion along wettability gradients have demonstrated that a contact-angle hysteresis of $\leq 10^{o}$ is required to achieve droplet motion.[12] Evidence that this condition was met in the present studies was obtained from Wilhelmy plate based measurements of the dynamic water contact angle made on substrates coated with gradients on both sides. Spectroscopic ellipsometry was used to determine gradient film thickness. Gradient films in this case were prepared on silica-base-layer coated silicon substrates. The use of silicon substrates afforded the signal levels necessary for detection of monolayer and submonolayer films.

The microscope employed to record fluorescence images of the surface-bound YOYO-1 labeled DNA molecules has been described previously, in detail.[43] Briefly, wide-field images of the DNA molecules were acquired using blue laser light (488 nm, ~ 1 mW) for fluorescence excitation. The laser light was first directed through a spinning optical diffuser, reflected from an appropriate dichroic mirror, and then focused into the back aperture of the water immersion objective (Nikon, 40X, 1.15 numerical aperture) used for sample illumination. Fluorescence

from the sample was collected using the same objective, in the epi-illumination geometry. The fluorescence was separated from residual laser light by passage back through the dichroic mirror and through an appropriate bandpass filter. After additional optical magnification of ~ 2.3X, fluorescence images were recorded on an electron-multiplying CCD camera, operated in conventional gain mode. The image pixel size was calibrated using fluorescent polystyrene beads. By this method, the 2 X 2-binned pixels in the images were determined to be 330 X 330 nm^2 in size. The fluorescence images obtained were all background subtracted and flattened using a rolling ball method (25 pixel ball radius) and subsequently subjected to a Gaussian smoothing routine (σ = 1 pixel width), using software written in house. All DNA analysis was performed using the ImageJ software package.

7.3 Results and Discussion

7.3.1 Gradient Characterization. Sessile drop water contact angle measurements were used to verify that a wettability gradient was obtained after VPD of each silane. **Figure 7.1A** depicts representative results. Contact angle measurements could not be obtained from the initial steep portion of each gradient, because the droplets spontaneously moved down the surface in this region. Dynamic contact angle data were also obtained from the gradients, by the Wilhelmy plate method. An example of the results obtained is depicted in **Figure 7.1B**. These data yield contact angles that are similar to those of the sessile drop measurements, although they were obtained from a different gradient. Most importantly, they reveal that the contact angle hysteresis was $\leq 10^o$ over a distance of ~ 6 mm from the high C8-silane end.[12] This distance corresponds well with the distance over which the droplets were observed to move.

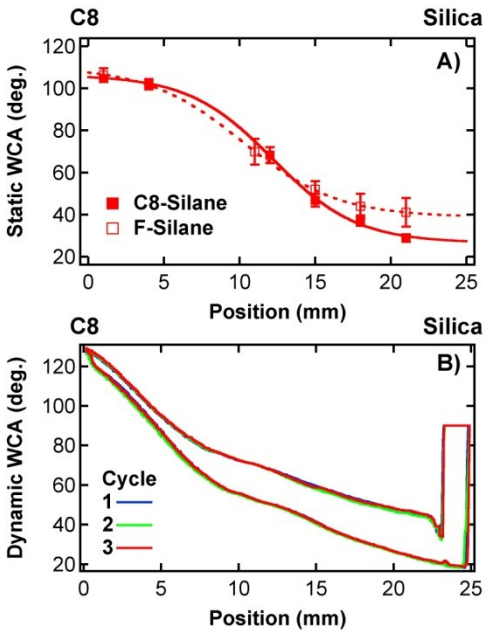

Figure 7.1 A) Representative sessile drop water contact angle (WCA) data obtained along C8- and F-silane gradients. Each data point shows the average of three measurements made across the film at three different locations. The error bars depict the standard deviation of these measurements. **B**) Representative dynamic WCA results along a different C8-silane gradient, coated on both sides of the substrate. The upper and lower traces represent advancing and receding contact angles, respectively, for three consecutive cycles. The dynamic WCA data were acquired by Kayesh Ashraf, Virginia Commonwealth University, on sample prepared at Kansas State University.

Figure 7.2 shows the displacement of droplet (2 μL) over time extracted from the video of droplet motion. In the video, the droplet once deposited on hydrophobic end, spontaneously moved toward the hydrophilic end.

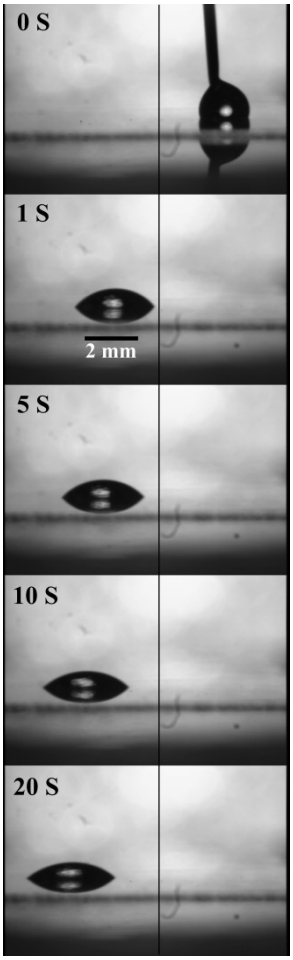

Figure 7.2 Displacement of a 2μL droplet of DNA containing solution as it moved from hydrophobic (C8) end toward the hydrophilic (silica) end. Each images was acquired from the video recorded during the droplet motion.

Figure 7.3 represents the Ellipsometric measurements of thickness along the gradients. The data revealed that the average film thickness near the hydrophobic end of a C8-silane gradient was ~ 1.3 nm. The film thickness gradually decreased down the gradient and became negligible at a distance of ~ 10 mm from the C8-silane end. The 1.3 nm film thickness is similar to the 1.1 nm thickness expected for a monolayer of well-packed C8 chains oriented perpendicular to the film surface.

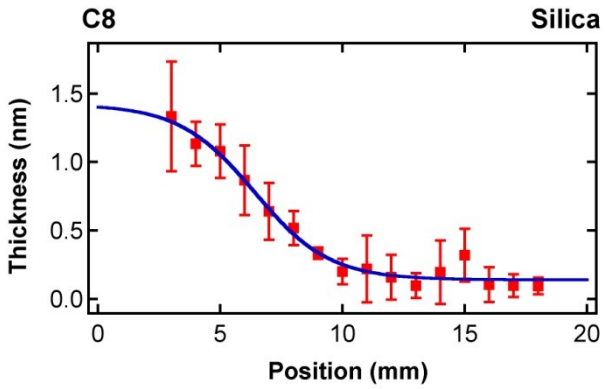

Figure 7.3 Ellipsometric film thickness along a C8-silane gradient, demonstrating transformation of surface coverage from approximately one monolayer on the left to the uncoated silica base layer on the right.

7.3.2 DNA Imaging Studies. In studies of DNA adsorption, elongation and alignment, 2 μL droplets of 40 pM λ-DNA in PBS solution were placed ~ 5 mm from the substrate edge, on the C8-silane end of the gradient. The droplets placed at this position initially moved rapidly (~ 4 mm/s) down the gradient before slowing to lower velocity (~ 0.1 mm/s) and subsequently stopping. The droplets moved a total distance of ~ 4 mm after first contacting the gradient surface. Similar droplet motion was also observed along the F-silane gradient. Replicate data sets were acquired from each of the gradients by depositing three droplets at separations of 4 mm along a line running perpendicular to the gradient axis.

Wide-field fluorescence images of surface-adsorbed YOYO-1 labeled DNA molecules were acquired along the gradients beginning from the position where the droplet was first deposited. Subsequent images were obtained by moving down the droplet path, towards the point where the droplet stopped. Several hundred images were acquired from five C8- and F-silane

gradients. Images were not acquired from the final droplet position, because a large quantity of DNA was deposited at this location, as the droplet evaporated.

Figure 7.4 depicts representative images of YOYO-1 labeled λ-DNA on the gradients investigated. Shown are images acquired near the hydrophobic end (**Figure 7.4A**) and near the hydrophilic end (**Figure 7.4B**) of a C8-silane gradient. Also shown are images from a F-silane gradient at the hydrophobic end (**Figure 7.4C**) and another from a C8-silane gradient in the absence of λ-DNA (**Figure 7.4D**). Based on the microscope calibration described in Experimental Considerations, the size of the region depicted in each fluorescence image was ~ 73 x 73 μm^2. In all cases, the gradients were oriented from right (hydrophobic end) to left (hydrophilic end) on the images. Linear fluorescent features ascribed to elongated λ-DNA molecules were observed in images of all samples on which dye-labeled DNA-containing droplets had been deposited. The blank shown in **Figure 7.4D** demonstrates that no elongated fluorescent features were found in the absence of λ-DNA.

The imaging results show that DNA molecules deposited on the C8-silane gradient (**Figures 7.4A,B**) were generally elongated in the expected direction (right to left). DNA alignment in this direction was most frequently observed in central regions of the gradient (i.e., nearest its center line) and nearest the center of each droplet as it moved down the gradient. Deviations from this orientation were commonly observed off the gradient central axis and as a function of distance from the droplet center (see **Figures 7.4B,C**). These issues are addressed further, below, as they provide evidence for the mechanism of DNA elongation and alignment.

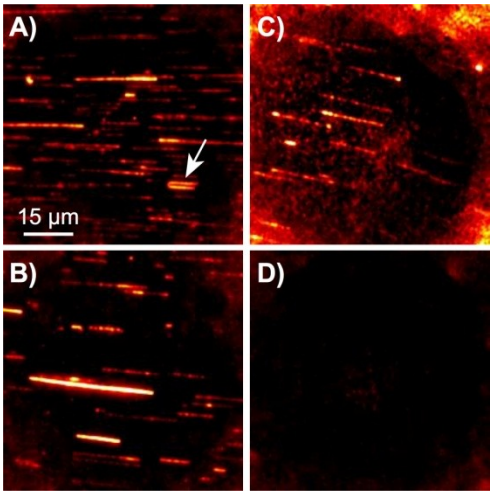

Figure 7.4 A), B) Representative fluorescence images of elongated λ-DNA from near the hydrophobic and hydrophilic ends, respectively, on a C8-silane gradient. **C**) Image of λ-DNA on a F-silane gradient. The DNA in panels **A**) - **C**) was deposited by a spontaneously moving droplet. The original droplet motion was from right to left along the horizontal axis on each image. **D**) Fluorescence image from a region traversed by a YOYO-1 doped droplet in the absence of λ-DNA. A scale bar is shown in panel A, this same scale bar applies to all images. The color scale depicts fluorescence counts. In panels **A**), **C**), and **D**), the signal ranges from 50 - 1250 counts (black - white), while in panel **B**) the maximum value is 2000 counts. The white arrow shown in **A**) points to a "hairpin-like" molecule. All images were background subtracted and flattened to compensate for the Gaussian profile in the fluorescence signal caused by sample illumination through the water immersion objective. The background visible around the edges of panel **C**) is an artifact due to image flattening. A Gaussian smooth (σ = 1 pixel width) was also applied to enhance the signal-to-noise ratio of the images.

The density of λ-DNA adsorbed to the gradient surface was quantitatively assessed by manually counting the number of DNA molecules found in each image. The mean number of

DNA molecules in each image is plotted as a function of position along representative C8- and F-silane gradients in **Figure 7.5A**. The results show a significant, approximately eight-fold reduction in the density of DNA on the F-silane gradient, compared to that observed on the C8-silane gradient. This difference between the C8- and F-silane gradients is likely due to the omniphobic character of perfluorinated films,[205] and demonstrates that the F-silane surface is not well suited to combing of DNA.

In addition to its dependence on the silane precursor employed, the density of adsorbed DNA also exhibits a clear dependence on position along each gradient (see **Figure 7.5A**). These results indicate that hydrophobic interactions between the DNA molecules and gradient surface play an important role in governing DNA adsorption. Towards the hydrophilic end, fewer hydrocarbon groups are available to interact with the DNA and fewer molecules attach to the surface as a result. Such effects are well known, as has been reported in the literature.[206,207] Because of the dramatically lower density of adsorbed DNA on the F-silane gradients, no further analysis of the data from these surfaces is reported here.

The extent of DNA elongation and alignment along the C8-silane gradients were quantified by manually measuring the length and orientation of each molecule in the film plane. **Figure 7.4B** provides histograms showing the distribution of DNA lengths as a function of position along a representative C8-silane gradient. The full contour length of the λ-DNA employed is 16.5 μm,[186] while its persistence length and radius of gyration are only ~ 50 nm and ~ 0.8 μm, respectively.[208] The distributions shown in **Figure 7.4B** are all peaked near ~ 6 μm, indicating that the most common DNA molecules are elongated to ~ 40% of their full length, under the present conditions. These same data yield an arithmetic mean DNA length of ~ 11 μm (see **Figure 7.4A**), corresponding to ~ 70% of the full contour length.

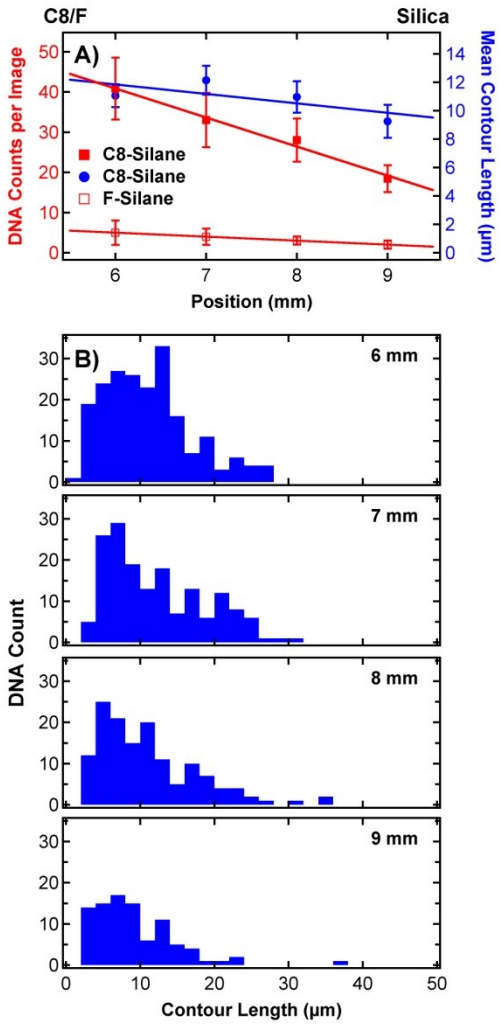

Figure 7.5 A) Mean DNA counts (per image, 73 X 73 μm^2) from five replicate images as a function of position along C8-silane and F-silane gradients. Also shown is the mean DNA contour length along the C8-silane gradient. The error bars depict the 95% confidence intervals. The solid lines have been appended to better depict the trends. The DNA density is observed to decrease with decreasing surface hydrophobicity at > 99.9% confidence, while the trend towards shorter DNA molecules is only detected at 95% confidence. **B**) Histograms showing DNA length distributions as a function of position along a C8-silane gradient.

The histograms depicted in **Figure 7.5B** demonstrate that the DNA length distributions are relatively broad. Many molecules appear to be much shorter than the most common length, while some appear to be longer than the full contour length. The appearance of relatively short DNA molecules has at least two possible origins. First, it is clear that as the DNA solutions age, fragmentation of the DNA leads to a shortening of the molecules. To help avoid these contributions, fresh DNA solutions were used in the present studies and all DNA solutions were stored in a refrigerator prior to use. Unfortunately, fragmentation of the DNA could not be completely avoided and some of the DNA molecules appeared shorter, even when fresh solutions prepared from new DNA samples were employed. The presence of these shorter molecules has previously been attributed to their fragmentation during handling.[188] Second, the images obtained reveal that some DNA molecules attach to the gradient surface at both ends. In this case, the DNA folds back on itself while it is being elongated, forming "hairpin-like" strands exhibiting a clear "loop" at the down-gradient end of the DNA molecule. Such "hairpin-like" structures have been reported previously[209] and were also observed in the fluorescence images acquired for the present studies (see white arrow in **Figure 7.4A**). When easily detected, these molecules have been removed from the data and are not included in **Figure 7.5**. However, in situations where the folded arms of the DNA strand are too close together to be resolved, no "loop" is observed. Instead, the close proximity of the two arms leads to an image that is brighter than that of the fully unfolded strand. Two DNA strands that have been shortened by fragmentation and are fortuitously found near each other produce a similar effect. Because of the reliance on human judgment in distinguishing such molecules, they have not been removed from the data set and are included in the histograms shown in **Figure 7.5**. Their presence leads to an apparent shortening of the overall population of elongated DNA molecules.

The appearance of DNA molecules that are longer than the maximum expected length (16.5 μm) is also easily explained and has been reported widely in the literature.[186,188,192] For example, it is known that DNA molecules can be overstretched, resulting in a change in their conformation, and in their maximum length.[210] Indeed, the forces acting on the DNA during its elongation in the present studies are expected to be relatively strong[188] compared to those needed to "overstretch" λ-DNA.[181] Furthermore, as noted above, two or more individual DNA molecules may adsorb to the gradient surface in close proximity so that their images cannot be resolved. Again, such overlapped DNA strands produce an image that is brighter than expected for an isolated molecule. While the occurrence of these overlapped strands is often easily identified in the fluorescence images (i.e., the brightest strands in **Figure 7.4**), nonuniformity in the fluorescence intensity resulting from the use of epi-illumination methods and imperfections in the incident laser field preclude their quantitative removal. As a result, none of these have been removed from the histograms shown in **Figure 7.5B**.

Figure 7.5A plots the mean length of the DNA molecules in the histograms shown in **Figure 7.5B**. As with the DNA density data, the mean length of the DNA molecules is also found to decrease from the hydrophobic to hydrophilic ends of the gradient. A statistical test performed on the slope of the trend line indicates that it is significant at the 95% confidence level. The observed trend has two likely origins. First, it is possible that the aforementioned overlapped DNA molecules bias the results to larger values at the hydrophobic end. As the density of adsorbed DNA decreases, their occurrence becomes less common and the average molecular length becomes shorter. Second, the relatively longer DNA molecules found near the hydrophobic end of the gradient suggest a shear-force mechanism for DNA elongation. In this case, the forces active during elongation are defined by the velocity profile (or gradient) within

the liquid droplet, near the solution-surface interface. As the droplet slows, the velocity gradient becomes less significant, the forces acting upon the DNA become smaller, and the molecules are less elongated as a result. For reasons discussed below, it is believed the position-dependent decrease in DNA length in **Figure 7.5A** is dominated by the decrease in DNA density, rather than by a change in droplet velocity.

The alignment of the DNA molecules observed along a line running perpendicular to the gradient axis also exhibits a monotonic trend with position. **Figure 7.6** depicts representative images and histograms showing the observed trend. With a volume of 2 μL and a contact angle of ~ 70^{o} (estimated from the receding contact angle in **Figure 7.1B**) the radius of the circular contact line formed between a hemispherical water droplet and the gradient surface would be 0.54 mm, as described in **Appendix**. The data in **Figure 7.6** were acquired at 0.2 (± 0.1) mm intervals across the gradient width, beneath the pathway of a single droplet. The same trend was found at all other positions investigated along the length of this gradient, as well as in replicate measurements made on different gradients prepared in the same manner. The results show that DNA alignment depends upon the lateral distance of each location from the center of the droplet, as it moved down the gradient. DNA alignment was found to be parallel to the direction of droplet motion for central droplet regions. Towards the outer edges of the droplet, substantial characteristic deviations in the DNA orientation were observed. The top and bottom histograms shown in **Figure 7.6** provide relevant examples of the latter. The top and bottom histograms were derived from images acquired at ± 0.4 mm from the droplet center. In contrast, the images acquired at ± 0.2 mm show markedly smaller deviations from the DNA alignment near the center of the droplet (0.0 mm in **Figure 7.6**). This behavior is very similar to that reported in previous publications on non-gradient materials.[183,188]

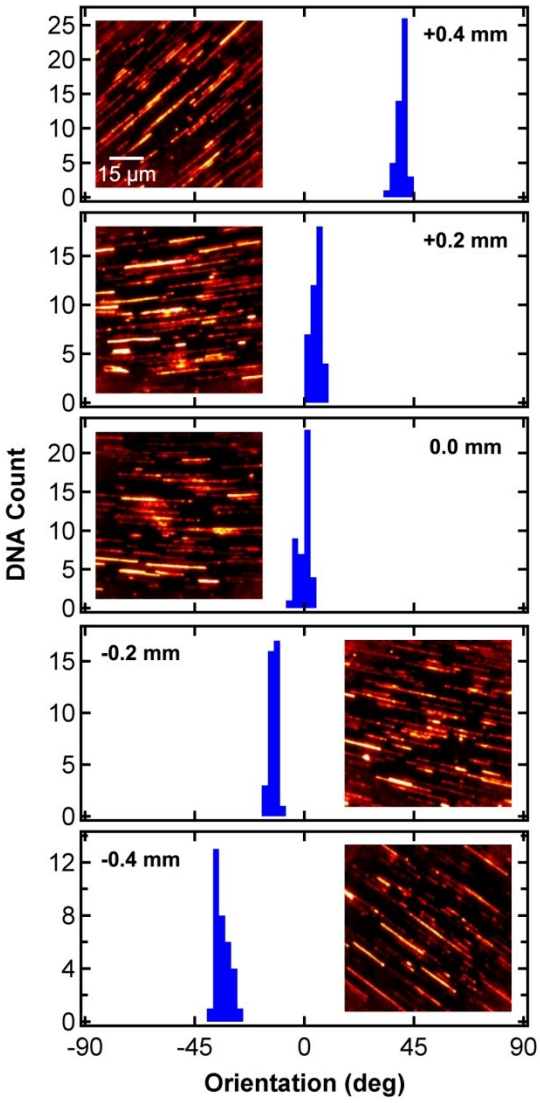

Figure 7.6 Histograms showing DNA alignment in the film plane, as a function of position across the droplet pathway. These data were acquired at the high C8-silane end of a gradient. The insets show the images from which each histogram is derived and were acquired at 0.2 mm spacings for one droplet placed near the gradient centerline. A scale bar is shown in the top panel. This same scale bar applies to all images. The color scale depicts fluorescence counts ranging from zero to 10^3 counts per pixel in each image.

The results shown in **Figure 7.6** are consistent with alignment of the DNA molecules perpendicular to the contact line at the trailing edge of the water droplet as it moved down the gradient. Under the circumstances mentioned above, the DNA molecules should be aligned at angles of ± 47.8^{o} at a distance of ± 0.4 mm from the droplet center (see Appendix), while mean angles of + 39.9^{o} and -33.8^{o} are obtained from the data in **Figure 7.6**. Likewise, at ± 0.2 mm, the expected DNA alignment angles are ± 21.7^{o}. The data in **Figure 7.6** give mean values of + 4.6^{o} and - 12.5^{o} in this case. The differences between the measured and expected values are readily explained by both experimental and theoretical challenges. For example, the error in determining the exact location of each image is estimated to be ± 0.1 mm, giving up to ~ 10^{o} to 15^{o} errors in the expected DNA orientation at ± 0.2 mm and ± 0.4 mm distances, respectively. Furthermore, the DNA is elongated by a moving droplet, while a model for a static hemispherical droplet was used to estimate DNA alignment. Deviations from a hemispherical droplet shape also arise from the presence of the gradient itself, which causes the contact angle to vary with position.

The results described above nevertheless provide clear evidence for the mechanism of DNA adsorption, alignment and elongation as the droplet moves down the gradient. **Figure 7.7A** provides a pictorial model for this mechanism. Briefly, the first step in DNA elongation and alignment involves attachment of (at least) one of the strand ends to the hydrophobic surface.[206] As the droplet moves down the gradient, the remainder of the DNA strand is pulled through the water-air interface. The force imparted on the DNA by the surface tension at this interface leads to its elongation. Alignment of the DNA along the direction perpendicular to the droplet-surface contact line arises because the net force on the DNA is oriented in this direction.[188] Were the molecules elongated by shear forces due to droplet motion alone, all the DNA molecules would instead align parallel to the direction of droplet motion, regardless of position within the droplet.

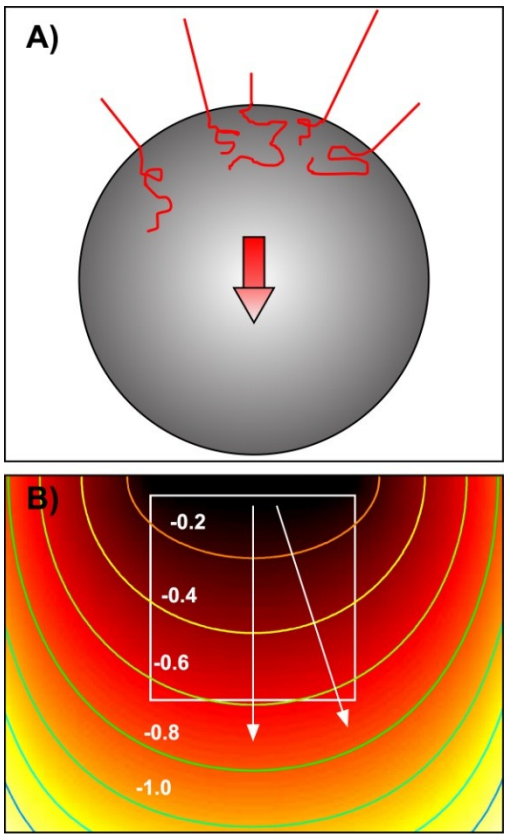

Figure 7.7 A) Model for deposition of aligned DNA (red lines, not drawn to scale) from the trailing edge of a moving droplet (gray circle, ~ 1 mm diameter). DNA adsorbed to the surface at one of its ends is elongated and aligned by surface tension forces imparted on the molecule as it is pulled through the water-air interface. **B**) Model for vapor diffusion during gradient deposition. The contour lines depict log(concentration), in arbitrary units, for the precursor. The white square shows the location of the substrate and its size (25.4 mm x 25.4 mm). The white arrows depict the steepest direction (perpendicular to the contour lines) along the gradient at different positions. The reservoir is at the top of the simulated region, above the white square.

As a caveat to the above discussion, it should be noted that some deviation in the direction of droplet motion was also observed across the gradient surface, particularly when droplets were

placed off the gradient centerline. Deviations in the droplet direction with distance from the gradient central axis that result from curvature in the gradient profile produced by the curved vapor diffusion front emanating from the precursor reservoir during film formation. To demonstrate this effect, finite difference time domain methods were employed to solve Fick's Second Law in two dimensions, using a model of the deposition apparatus. Details are given in the **Appendix**. The results are shown in **Figure 7.7B**. The contour lines shown depict the aforementioned curvature. The water droplets were found to move along the steepest wettability gradient, i.e. perpendicular to the contour lines (see white arrows) at different positions across the gradient.

The surface-tension mechanism for DNA alignment produces elongated DNA that is very well oriented in the film plane, with the vast majority of molecules in each image aligning parallel to one another. Assessment of the degree of DNA alignment was performed by calculating a 2D order parameter for the DNA molecules in each image. The order parameter in this case is defined by $\langle P \rangle = (2\langle \cos^2 \Delta\theta \rangle - 1)$,[211] where $\Delta\theta$ represents the tilt of each DNA molecule from the local mean angle, $\bar{\theta}$, and the brackets ($\langle \rangle$) indicate that the average across all observed DNA molecules is calculated. Perfect alignment of the molecules would give $\langle P \rangle = 1$, while randomly oriented molecules would yield $\langle P \rangle = 0$. The results shown in **Figure 7.6** all yield $\langle P \rangle > 0.99$. These results indicate that the DNA molecules are all very well aligned with little distribution in their in-plane orientation angles, exactly as would be expected when the results of DNA deposition by a macroscopic droplet are observed locally under a microscope.

7.4 Conclusion

In conclusion, the use of wettability gradients for molecular combing has been demonstrated. Unlike in more common methods where the sample is tilted or withdrawn from a solution to produce a moving meniscus that elongates the DNA, the DNA-containing water droplets in the present studies moved spontaneously along the gradient surface from hydrophobic to hydrophilic regions, leaving elongated DNA molecules in their path. DNA elongation and alignment were shown to occur by a previously reported surface-tension-driven mechanism.[188] The DNA was elongated to ~ 70% of its full contour length, on average, and DNA alignment was found to be perpendicular to the droplet-gradient contact line. The preparation of surfaces that can be used to manipulate DNA and other biomolecules in the absence of external stimuli promise to facilitate the development of fully automated, inexpensive, disposable devices for the analysis of genetic rearrangements and instabilities associated with cancer, in studies of protein-DNA interactions[175] and in detection and identification of microbial hazards.

Chapter 8 - General Conclusion and Future Direction

8.1 General Conclusion

This dissertation presents applications of SMS to quantitatively measure the nanoscale polarity of sol-gel derived thin film gradients. SMT is also used to examine the mass transport dynamics of probe molecules on gradient SAM films under ambient humidity conditions. Both single-molecule techniques (SMS & SMT) have emerged as powerful means to study the nanoscale properties and the transport dynamics associated with thin-film chemical gradients. These properties would be otherwise obscured by conventional ensemble-based techniques. The use of highly sensitive fluorescent dyes, laser excitation sources, a highly sensitive detector, selective optics and high-throughput data analysis all come together to allow for single molecules to be detected with spatial resolution well beyond the diffraction limit of light, allowing for super-resolution characterization of the samples by single-molecule techniques. In particular, the ability to locate fluorescent molecules with very high precision, and to study their emission characteristics from the localized molecules allow for both the properties and transport dynamics associated with thin- film gradient materials to be studied at the nanoscale.

In **Chapter 5**, sol-gel based IWDC was employed to prepare a macroscopic thin-film gradient in polarity by using polar and nonpolar organosilane precursors. An empirical relation between the fluorescence of solvatochromic Nile Red and the solvent polarity was established by calibration of the wide-field microscope. This relationship was extended to obtain the microscopic polarity in the form of the CM factor from the fluorescence of individual Nile Red molecules doped into the thin-film gradients. SMS characterization indicates the polarity of the gradient film is highly variable, changing on length scales of a few nanometers to a few micrometers. Compilation of microscopic polarity data in the form of histograms further

provided the polarity distribution along the gradient film. The technique also revealed evidence of phase-separation in the mid-region along the gradient. Some of the polarity data determined outside the range of CM factor showed evidence of specific film-dye interactions, possibly through H-bonding.

In **Chapter 6**, macroscopic wettability gradients derived from SAM films were prepared by vapor-phase deposition of hydrophobic and hydrophilic organochlorosilane precursors. Ellipsometric thickness measurements and AFM images acquired along the gradient films under different humidity conditions confirmed the condensation of nanoscale water on their surfaces. Mass transport of a hydrophobic PDI dye in the water layer condensed over the gradient SAM was studied by employing SMT. Trajectories for each of the PDI molecules were generated by linking the single molecule positions frame to frame. Further analyses of the trajectories were carried out in order to calculate the step-size, mean square displacement and diffusion coefficient. The results indicate an increase in population of mobile molecules with an increase in both the SAM wettability and the RH of the environment. Furthermore, molecules found in the hydrophilic region were shown to follow a Fickian (Brownian) diffusion mechanism while those at the hydrophobic end exhibited desorption-mediated Levy diffusion. A complex trend in the evolution of the diffusion coefficient along the gradient was also found under each humidity condition.

In **Chapter 7**, the ability of steep wettability gradients to drive the motions of water droplets was utilized, for the first time, in the spontaneous combing of DNA molecules. For this purpose wettability gradients prepared by using C8-silane and fluorinated C8-silane were employed. The DNA molecules were found to stretch in the direction of droplet motion from the hydrophobic end toward the hydrophilic end along both gradients. A decreasing density of

elongated DNA was found toward the regions of higher wettability in both gradients. However, the density of elongated DNA on gradient from fluorinated C8-silane was much smaller compared to that from C8-silane. In addition, DNA molecule were aligned perpendicular to the gradient-droplet contact line. The results on DNA alignment reveal the surface tension forces mainly responsible for the DNA elongation with negligible effect of shear forces.

This dissertation also reports different methods for the preparation of macroscale thin-film chemical gradients. The research work was also directed towards understanding the effects of various processing conditions on the overall quality and reproducibility of the thin-film gradient materials, and their optimization. The use of thin-film chemical gradients in combinatorial materials research was clearly demonstrated in this dissertation. Here, thin-film gradients served as combinatorial libraries to measure the properties of materials having a wide range of chemical compositions along a single sample in a high-throughput manner.

8.2 Future Direction

Thin-film chemical gradients have provided more convenient and practical ways to carry out combinatorial material research in addition to their ability to drive mass transport relevant in many applications. Current research is mostly focused on controlling gradient properties at the macroscale. However, the use of gradients as functional materials in many applications depends upon their molecular properties at the nanoscale. Therefore, future effort needs to be directed towards controlling the nanoscale properties of thin-film chemical gradients.

In the first study of this dissertation, the rate of infusion of TMOS and that of withdrawal of waste were increased in five minute intervals during IWDC. As a result, the degree of continuous change in composition of the binary sol also increased in a stepwise manner. This, in

turn, is likely to cause the gradient steepness to change in a stepwise (distinct) fashion. In order to produce a smooth change in properties along a gradient that has a single steepness, the rates of infusion and withdrawal during IWDC could instead be programmed in ramps. This would produce a binary sol whose composition changes in a continuous and smooth manner.

The SMS characterization of nanoscale properties of gradient SAM films could assist in the designing of better molecularly engineered surfaces. However, the monolayer thickness of these SAM films make their characterization difficult as the fluorescent probes need to be incorporated within the film in order to respond to the film properties. There is limited knowledge regarding the effects of SAM film thickness on the emissive response of the fluorescent probes. Therefore, a systematic study in which the fluorescence is measured as a function of SAM film thickness would be very useful in determining the optimum thickness of such films for SMS characterization.

In sol-gel based dip coating techniques such as IWDC, the rates of infusion and withdrawal can be programmed so as to produce a gradient of desired steepness. Such control over the gradient steepness is very difficult in VPD of the gradient SAMs. However, experiments aimed at exploring the effect of two key parameters on gradient steepness, the silane to substrate separation and the exposure time during VPD would be highly useful.

Chapter 9 - References

(1) Morgenthaler, S.; Zink, C.; Spencer, N. D. Surface-chemical and -morphological gradients. *Soft Matter* **2008**, *4*, 419-434.

(2) Genzer, J.; Bhat, R. R. Surface-bound soft matter gradients. *Langmuir* **2008**, *24*, 2294-2317.

(3) Genzer, J. Surface-Bound Gradients for Studies of Soft Materials Behavior. *Annual Review of Materials Research, Vol 42* **2012**, *42*, 435-468.

(4) Elwing, H.; Welin, S.; Askendal, A.; Nilsson, U.; Lundstrom, I. A Wettability Gradient-Method for Studies of Macromolecular Interactions at the Liquid Solid Interface. *Journal of Colloid and Interface Science* **1987**, *119*, 203-210.

(5) Morgenthaler, S.; Lee, S. W.; Zurcher, S.; Spencer, N. D. A simple, reproducible approach to the preparation of surface-chemical gradients. *Langmuir* **2003**, *19*, 10459-10462.

(6) Kannan, B.; Dong, D.; Higgins, D. A.; Collinson, M. M. Profile Control in Surface Amine Gradients Prepared by Controlled-Rate Infusion. *Langmuir* **2011**, *27*, 1867-1873.

(7) Faustini, M.; Ceratti, D. R.; Louis, B.; Boudot, M.; Albouy, P.-A.; Boissiere, C.; Grosso, D. Engineering Functionality Gradients by Dip Coating Process in Acceleration Mode. *Acs Applied Materials & Interfaces* **2014**, *6*, 17102-17110.

(8) Giri, D.; Hanks, C. N.; Collinson, M. M.; Higgins, D. A. Single-Molecule Spectroscopic Imaging Studies of Polarity Gradients Prepared by Infusion-Withdrawal Dip-Coating. *Journal of Physical Chemistry C* **2014**, *118*, 6423-6432.

(9) Kraus, T.; Stutz, R.; Balmer, T. E.; Schmid, H.; Malaquin, L.; Spencer, N. D.; Wolf, H. Printing chemical gradients. *Langmuir* **2005**, *21*, 7796-7804.

(10) Sankhe, A. Y.; Booth, B. D.; Wiker, N. J.; Kilbey, S. M. Inkjet-printed monolayers as platforms for tethered polymers. *Langmuir* **2005**, *21*, 5332-5336.

(11) Krabbenborg, S. O.; Huskens, J. Electrochemically Generated Gradients. *Angewandte Chemie-International Edition* **2014**, *53*, 9152-9167.

(12) Chaudhury, M. K.; Whitesides, G. M. How to Make Water Run Uphill. *Science* **1992**, *256*, 1539-1541.

(13) Gunawan, R. C.; Silvestre, J.; Gaskins, H. R.; Kenis, P. J. A.; Leckband, D. E. Cell migration and polarity on microfabricated gradients of extracellular matrix proteins. *Langmuir* **2006**, *22*, 4250-4258.

(14) Uedayukoshi, T.; Matsuda, T. Cellular-Responses on a Wettability Gradient Surface with Continuous Variations in Surface Compositions of Carbonate and Hydroxyl-Groups. *Langmuir* **1995**, *11*, 4135-4140.

(15) Lee, J. H.; Kim, H. G.; Khang, G. S.; Lee, H. B.; Jhon, M. S. Characterization of Wettability Gradient Surfaces Prepared by Corona Discharge Treatment. *Journal of Colloid and Interface Science* **1992**, *151*, 563-570.

(16)Ye, F. M.; Cui, C. C.; Kirkeminde, A.; Dong, D.; Collinson, M. M.; Higgins, D. A. Fluorescence Spectroscopy Studies of Silica Film Polarity Gradients Prepared by Infusion-Withdrawal Dip-Coating. *Chemistry of Materials* **2010**, *22*, 2970-2977.

(17) Kannan, B.; Nokura, K.; Alvarez, J. C.; Higgins, D. A.; Collinson, M. M. Fabrication of Surface Charge Gradients in Open-Tubular Capillaries and Their Characterization by Spatially Resolved Pulsed Streaming Potential Measurements. *Langmuir* **2013**, *29*, 15260-15265.

(18) Bhat, R. R.; Tomlinson, M. R.; Genzer, J. Assembly of nanoparticles using surface-grafted

orthogonal polymer gradients. *Macromolecular Rapid Communications* **2004**, *25*, 270-274.

(19) Cui, C.; Kirkeminde, A.; Kannan, B.; Collinson, M. M.; Higgins, D. A. Spatiotemporal Evolution of Fixed and Mobile Dopant Populations in Silica Thin-Film Gradients as Revealed by Single Molecule Tracking. *Journal of Physical Chemistry C* **2011**, *115*, 728-735.

(20) Balss, K. M.; Kuo, T. C.; Bohn, P. W. Direct chemical mapping of electrochemically generated spatial composition gradients on thin gold films with surface-enhanced Raman spectroscopy. *Journal of Physical Chemistry B* **2003**, *107*, 994-1000.

(21) Bhat, R. R.; Fischer, D. A.; Genzer, J. Fabricating planar nanoparticle assemblies with number density gradients. *Langmuir* **2002**, *18*, 5640-5643.

(22) Potyrailo, R. A.; Wroczynski, R. J.; Pickett, J. E.; Rubinsztajn, M. High-throughput fabrication, performance testing, and characterization of one-dimensional libraries of polymeric compositions. *Macromolecular Rapid Communications* **2003**, *24*, 124-130.

(23) Jayaraman, S.; Hillier, A. C. Construction and reactivity mapping of a platinum catalyst gradient using the scanning electrochemical microscope. *Langmuir* **2001**, *17*, 196101.

(24) Singh, M.; Berkland, C.; Detamore, M. S. Strategies and Applications for Incorporating Physical and Chemical Signal Gradients in Tissue Engineering. *Tissue Engineering Part B-Reviews* **2008**, *14*, 341-366.

(25) Harris, B. P.; Kutty, J. K.; Fritz, E. W.; Webb, C. K.; Burg, K. J. L.; Metters, A. T. Photopatterned polymer brushes promoting cell adhesion gradients. *Langmuir* **2006**, *22*, 4467-4471.

(26) Beurer, E.; Venkataraman, N. V.; Sommer, M.; Spencer, N. D. Protein and Nanoparticle Adsorption on Orthogonal, Charge-Density-Versus-Net-Charge Surface-Chemical

Gradients. *Langmuir* **2012**, *28*, 3159-3166.

(27) Walder, R.; Honciuc, A.; Schwartz, D. K. Directed Nanoparticle Motion on an Interfacial Free Energy Gradient. *Langmuir* **2010**, *26*, 1501-1503.

(28) Sitt, A.; Hess, H. Directed Transport by Surface Chemical Potential Gradients for Enhancing Analyte Collection in Nanoscale Sensors. *Nano Letters* **2015**, *15*, 3341-3350.

(29) Chang, T.; Rozkiewicz, D. I.; Ravoo, B. J.; Meijer, E. W.; Reinhoudt, D. N. Directional movement of dendritic macromolecules on gradient surfaces. *Nano Letters* **2007**, *7*, 978-980.

(30) Burgos, P.; Zhang, Z.; Golestanian, R.; Leggett, G. J.; Geoghegan, M. Directed Single Molecule Diffusion Triggered by Surface Energy Gradients. *Acs Nano* **2009**, *3*, 3235-3243.

(31) Solon, J.; Streicher, P.; Richter, R.; Brochard-Wyart, F.; Bassereau, P. Vesicles surfing on a lipid bilayer: Self-induced haptotactic motion. *Proceedings of the National Academy of Sciences of the United States of America* **2006**, *103*, 12382-12387.

(32) Smith, J. T.; Tomfohr, J. K.; Wells, M. C.; Beebe, T. P.; Kepler, T. B.; Reichert, W. M. Measurement of cell migration on surface-bound fibronectin gradients. *Langmuir* **2004**, *20*, 8279-8286.

(33) Smith, J. T.; Elkin, J. T.; Reichert, W. M. Directed cell migration on fibronectin gradients: Effect of gradient slope. *Experimental Cell Research* **2006**, *312*, 2424-2432.

(34) Ren, T.; Mao, Z.; Guo, J.; Gao, C. Directional Migration of Vascular Smooth Muscle Cells Guided by a Molecule Weight Gradient of Poly(2-hydroxyethyl methacrylate) Brushes. *Langmuir* **2013**, *29*, 6386-6395.

(35) Kannan, B.; Marin, M. A.; Shrestha, K.; Higgins, D. A.; Collinson, M. M. Continuous stationary phase gradients for planar chromatographic media. *Journal of Chromatography A*

2011, *1218*, 9406-9413.

(36) Dewoolkar, V. C.; Kannan, B.; Ashraf, K. M.; Higgins, D. A.; Collinson, M. M. Amine-phenyl multi-component gradient stationary phases. *Journal of Chromatography A* **2015**, *1410*, 190-199.

(37) Venkataraman, N. V.; Zurcher, S.; Spencer, N. D. Order and composition of methyl-carboxyl and methyl-hydroxyl surface-chemical gradients. *Langmuir* **2006**, *22*, 4184-4189.

(38) Chaudhury, M. K.; Chakrabarti, A.; Daniel, S. Generation of Motion of Drops with Interfacial Contact. *Langmuir* **2015**, *31*, 9266-9281.

(39) Longley, J. E.; Dooley, E.; Givler, D. M.; Napier, W. J., III; Chaudhury, M. K.; Daniel, S. Drop Motion Induced by Repeated Stretching and Relaxation on a Gradient Surface with Hysteresis. *Langmuir* **2012**, *28*, 13912-13918.

(40) Daniel, S.; Sircar, S.; Gliem, J.; Chaudhury, M. K. Ratcheting motion of liquid drops on gradient surfaces. *Langmuir* **2004**, *20*, 4085-4092.

(41) Wu, T.; Efimenko, K.; Genzer, J. Combinatorial study of the mushroom-to-brush crossover in surface anchored polyacrylamide. *Journal of the American Chemical Society* **2002**, *124*, 9394-9395.

(42) Wu, T.; Efimenko, K.; Vlcek, P.; Subr, V.; Genzer, J. Formation and properties of anchored polymers with a gradual variation of grafting densities on flat substrates. *Macromolecules* **2003**, *36*, 2448-2453.

(43) Giri, D.; Ashraf, K. M.; Collinson, M. M.; Higgins, D. A. Single-Molecule Perspective on Mass Transport in Condensed Water Layers over Gradient Self-Assembled Monolayers. *Journal of Physical Chemistry C* **2015**, *119*, 9418-9428.

(44) Albert, J. N. L.; Kim, J. D.; Stafford, C. M.; Epps, T. H., III. Controlled vapor deposition

approach to generating substrate surface energy/chemistry gradients. *Review of Scientific Instruments* **2011**, *82*.

(45) Genzer, J.; Efimenko, K.; Fischer, D. A. Formation mechanisms and properties of semifluorinated molecular gradients on silica surfaces. *Langmuir* **2006**, *22*, 8532-8541.

(46) Xia, Y. N.; Whitesides, G. M. Soft lithography. *Annual Review of Materials Science* **1998**, *28*, 153-184.

(47) Choi, S. H.; Newby, B. M. Z. Micrometer-scaled gradient surfaces generated using contact printing of octadecyltrichlorosilane. *Langmuir* **2003**, *19*, 7427-7435.

(48) Jeon, N. L.; Dertinger, S. K. W.; Chiu, D. T.; Choi, I. S.; Stroock, A. D.; Whitesides, G. M. Generation of solution and surface gradients using microfluidic systems. *Langmuir* **2000**, *16*, 8311-8316.

(49) Gunawan, R. C.; Choban, E. R.; Conour, J. E.; Silvestre, J.; Schook, L. B.; Gaskins, H. R.; Leckband, D. E.; Kenis, P. J. A. Regiospecific control of protein expression in cells cultured on two-component counter gradients of extracellular matrix proteins. *Langmuir* **2005**, *21*, 3061-3068.

(50) Shi, X.; Ostrovidov, S.; Shu, Y.; Liang, X.; Nakajima, K.; Wu, H.; Khademhosseini, A. Microfluidic Generation of Polydopamine Gradients on Hydrophobic Surfaces. *Langmuir* **2014**, *30*, 832-838.

(51) Terrill, R. H.; Balss, K. M.; Zhang, Y. M.; Bohn, P. W. Dynamic monolayer gradients: Active spatiotemporal control of alkanethiol coatings on thin gold films. *Journal of the American Chemical Society* **2000**, *122*, 988-989.

(52) Yamada, R.; Tada, H. Manipulation of droplets by dynamically controlled wetting gradients. *Langmuir* **2005**, *21*, 4254-4256.

(53) Kennedy, S. B.; Washburn, N. R.; Simon, C. G.; Amis, E. J. Combinatorial screen of the effect of surface energy on fibronectin-mediated osteoblast adhesion, spreading and proliferation. *Biomaterials* **2006**, *27*, 3817-3824.

(54) Roberson, S. V.; Fahey, A. J.; Sehgal, A.; Karim, A. Multifunctional ToF-SIMS: combinatorial mapping of gradient energy substrates. *Applied Surface Science* **2002**, *200*, 150-164.

(55) Harris, B. P.; Metters, A. T. Generation and characterization of photopolymerized polymer brush gradients. *Macromolecules* **2006**, *39*, 2764-2772.

(56) Caelen, I.; Gao, H.; Sigrist, H. Protein density gradients on surfaces. *Langmuir* **2002**, *18*, 2463-2467.

(57) Yu, X.; Wang, Z. Q.; Jiang, Y. G.; Zhang, X. Surface gradient material: From superhydrophobicity to superhydrophilicity. *Langmuir* **2006**, *22*, 4483-4486.

(58) Daniel, S.; Chaudhury, M. K.; de Gennes, P. G. Vibration-actuated drop motion on surfaces for batch microfluidic processes. *Langmuir* **2005**, *21*, 4240-4248.

(59) Venkataraman, N. V.; Zuercher, S.; Rossi, A.; Lee, S.; Naujoks, N.; Spencer, N. D. Spatial Tuning of the Metal Work Function by Means of Alkanethiol and Fluorinated Alkanethiol Gradients. *Journal of Physical Chemistry C* **2009**, *113*, 5620-5628.

(60) Beurer, E.; Venkataraman, N. V.; Rossi, A.; Bachmann, F.; Engeli, R.; Spencer, N. D. Orthogonal, Three-Component, Alkanethiol-Based Surface-Chemical Gradients on Gold. *Langmuir* **2010**, *26*, 8392-8399.

(61) Ashraf, K. M.; Giri, D.; Wynne, K. J.; Higgins, D. A.; Collinson, M. M. Cooperative Effects in Aligned and Opposed Multicomponent Charge Gradients Containing Strongly Acidic, Weakly Acidic, and Basic Functional Groups. *Langmuir* **2016**, *32*, 3836-3847.

(62) Keeling-Tucker, T.; Brennan, J. D. Fluorescent probes as reporters on the local structure and dynamics in sol-gel-derived nanocomposite materials. *Chemistry of Materials* **2001**, *13*, 3331-3350.

(63) Dunn, B.; Zink, J. I. Probes of pore environment and molecule-matrix interactions in sol-gel materials. *Chemistry of Materials* **1997**, *9*, 2280-2291.

(64) Brennan, J. D.; Hartman, J. S.; Ilnicki, E. I.; Rakic, M. Fluorescence and NMR characterization and biomolecule entrapment studies of sol-gel-derived organic-inorganic composite materials formed by sonication of precursors. *Chemistry of Materials* **1999**, *11*, 1853-1864.

(65) Flora, K. K.; Brennan, J. D. Characterization of the microenvironments of PRODAN entrapped in tetraethyl orthosilicate derived glasses. *Journal of Physical Chemistry B* **2001**, *105*, 12003-12010.

(66) Kaufman, V. R.; Avnir, D. Structural-Changes along the Sol-Gel-Xerogel Transition in Silica as Probed by Pyrene Excited-State Emission. *Langmuir* **1986**, *2*, 717-722.

(67) Nishida, F.; McKiernan, J. M.; Dunn, B.; Zink, J. I.; Brinker, C. J.; Hurd, A. J. In-Situ Fluorescence Probing of the Chemical-Changes During Sol-Gel Thin-Film Formation. *Journal of the American Ceramic Society* **1995**, *78*, 1640-1648.

(68) Moerner, W. E.; Kador, L. Optical Detection and Spectroscopy of Single Molecules in a Solid. *Physical Review Letters* **1989**, *62*, 2535-2538.

(69) Orrit, M.; Bernard, J. Single Pentacene Molecules Detected by Fluorescence Excitation in a Para-Terphenyl Crystal. *Physical Review Letters* **1990**, *65*, 2716-2719.

(70) Betzig, E.; Chichester, R. J. Single Molecules Observed by Near-Field Scanning Optical Microscopy. *Science* **1993**, *262*, 1422-1425.

(71) Hell, S. W.; Wichmann, J. Breaking the Diffraction Resolution Limit by Stimulated-Emission - Stimulated-Emission-Depletion Fluorescence Microscopy. *Optics Letters* **1994**, *19*, 780-782.

(72) Betzig, E.; Patterson, G. H.; Sougrat, R.; Lindwasser, O. W.; Olenych, S.; Bonifacino, J. S.; Davidson, M. W.; Lippincott-Schwartz, J.; Hess, H. F. Imaging intracellular fluorescent proteins at nanometer resolution. *Science* **2006**, *313*, 1642-1645.

(73) Hess, S. T.; Girirajan, T. P. K.; Mason, M. D. Ultra-high resolution imaging by fluorescence photoactivation localization microscopy. *Biophysical Journal* **2006**, *91*, 4258-4272.

(74) Rust, M. J.; Bates, M.; Zhuang, X. Sub-diffraction-limit imaging by stochastic optical reconstruction microscopy (STORM). *Nature Methods* **2006**, *3*, 793-795.

(75) Higgins, D. A.; Collinson, M. M.; Saroja, G.; Bardo, A. M. Single-molecule spectroscopic studies of nanoscale heterogeneity in organically modified silicate thin films. *Chemistry of Materials* **2002**, *14*, 3734-3744.

(76) Fu, Y.; Collinson, M. M.; Higgins, D. A. Single-molecule spectroscopy studies of microenvironmental acidity in silicate thin films. *Journal of the American Chemical Society* **2004**, *126*, 13838-13844.

(77) Fu, Y.; Ye, F. M.; Sanders, W. G.; Collinson, M. M.; Higgins, D. A. Single molecule spectroscopy studies of diffusion in mesoporous silica thin films. *Journal of Physical Chemistry B* **2006**, *110*, 9164-9170.

(78) Fasolka, M. J.; Stafford, C. M.; Beers, K. L. Gradient and Microfluidic Library Approaches to Polymer Interfaces. *Polymer Libraries* **2010**, *225*, 63-105.

(79) Meredith, J. C.; Karim, A.; Amis, E. J. High-throughput measurement of polymer blend phase behavior. *Macromolecules* **2000**, *33*, 5760-5762.

(80) Meredith, J. C.; Smith, A. P.; Karim, A.; Amis, E. J. Combinatorial materials science for polymer thin-film dewetting. *Macromolecules* **2000**, *33*, 9747-9756.

(81) Fischer, D. A.; Efimenko, K.; Bhat, R. R.; Sambasivan, S.; Genzer, J. Mapping surface chemistry and molecular orientation with combinatorial near-edge X-ray absorption fine structure spectroscopy. *Macromolecular Rapid Communications* **2004**, *25*, 141-149.

(82) Liedberg, B.; Tengvall, P. Molecular Gradients of Omega-Substituted Alkanethiols on Gold - Preparation and Characterization. *Langmuir* **1995**, *11*, 3821-3827.

(83) Liu, Y.; Klep, V.; Zdyrko, B.; Luzinov, I. Synthesis of high-density grafted polymer layers with thickness and grafting density gradients. *Langmuir* **2005**, *21*, 11806-11813.

(84) Xu, C.; Wu, T.; Mei, Y.; Drain, C. M.; Batteas, J. D.; Beers, K. L. Synthesis and characterization of tapered copolymer brushes via surface-initiated atom transfer radical copolymerization. *Langmuir* **2005**, *21*, 11136-11140.

(85) Wang, X. J.; Tu, H. L.; Braun, P. V.; Bohn, P. W. Length scale heterogeneity in lateral gradients of poly(N-isopropylacrylamide) polymer brushes prepared by surface-initiated atom transfer radical polymerization coupled with in-plane electrochemical potential gradients. *Langmuir* **2006**, *22*, 817-823.

(86) Fuierer, R. R.; Carroll, R. L.; Feldheim, D. L.; Gorman, C. B. Patterning mesoscale gradient structures with self-assembled monolayers and scanning tunneling microscopy based replacement lithography. *Advanced Materials* **2002**, *14*, 154-+.

(87) Ishiguro, Y.; Inagi, S.; Fuchigami, T. Gradient Doping of Conducting Polymer Films by Means of Bipolar Electrochemistry. *Langmuir* **2011**, *27*, 7158-7162.

(88) Xu, C.; Barnes, S. E.; Wu, T.; Fischer, D. A.; DeLongchamp, D. M.; Batteas, J. D.; Beers, K. L. Solution and surface composition gradients via microfluidic confinement: Fabrication

of a statistical-copolymer-brush composition gradient. *Advanced Materials* **2006**, *18*, 1427-1430

(89) Kannan, B.; Higgins, D. A.; Collinson, M. M. Aminoalkoxysilane Reactivity in Surface Amine Gradients Prepared by Controlled-Rate Infusion. *Langmuir* **2012**, *28*, 16091-16098.

(90) Brinker, C. J.; Scherer, G. W.: *Sol-Gel Science: The Physics and Chemistry of Sol-Gel Processing* Academic Press, Boston, MA, 1990.

(91) Iler, R. K.: *The Chemistry of Silica*. John Wiley and Sons: New York, 1979.

(92) Avnir, D.: Organic Chemistry within Ceramic Matrices: Doped Sol-Gel Materials. *Acc. Chem. Res.*, 1995; Vol. 28; pp 328-324.

(93) Ye, F.; Collinson, M. M.; Higgins, D. A. What can be learned from single molecule spectroscopy? Applications to sol-gel-derived silica materials. *Physical Chemistry Chemical Physics* **2009**, *11*, 66-82.

(94) Hess, C. M.; Riley, E. A.; Palos-Chavez, J.; Reid, P. J. Measuring the Spatial Distribution of Dielectric Constants in Polymers through Quasi-Single Molecule Microscopy. *Journal of Physical Chemistry B* **2013**, *117*, 7106-7112.

(95) Ba, K. H. T.; Everett, T. A.; Ito, T.; Higgins, D. A. Trajectory angle determination in one dimensional single molecule tracking data by orthogonal regression analysis. *Physical chemistry chemical physics : PCCP* **2011**, *13*, 1827-1835.

(96) Sbalzarini, I. F.; Koumoutsakos, P. Feature point tracking and trajectory analysis for video imaging in cell biology. *Journal of Structural Biology* **2005**, *151*, 182-195.

(97) Drelich, J.; Miller, J. D. MODIFICATION OF THE CASSIE EQUATION. *Langmuir* **1993**, *9*, 619-621.

(98) Drelich, J.; Wilbur, J. L.; Miller, J. D.; Whitesides, G. M. Contact angles for liquid drops at

a model heterogeneous surface consisting of alternating and parallel hydrophobic hydrophilic strips. *Langmuir* **1996**, *12*, 1913-1922.

(99) Li, Y.-S.; Wang, Y.; Ceesay, S. Vibrational spectra of phenyltriethoxysilane, phenyltrimethoxysilane and their sol-gels. *Spectrochimica Acta Part a-Molecular and Biomolecular Spectroscopy* **2009**, *71*, 1819-1824.

(100) Deye, J. F.; Berger, T. A.; Anderson, A. G. Nile red as a Solvatochromic Dye for Measuring Solvent Strength in Normal Liquids and Mixtures of Normal Liquids with Supercritical and Near Critical Fluids. *Analytical Chemistry* **1990**, *62*, 615-622.

(101) Lobnik, A.; Wolfbeis, O. S. Probing the polarity of sol-gels and ormosils via the absorption of Nile Red. *Journal of Sol-Gel Science and Technology* **2001**, *20*, 303-311.

(102) Dickson, R. M.; Norris, D. J.; Tzeng, Y. L.; Sakowicz, R.; Goldstein, L. S. B.; Moerner, W. E. Single molecules solvated in pores of polyacrylamide gels. *Molecular Crystals and Liquid Crystals Science and Technology Section a-Molecular Crystals and Liquid Crystals* **1996**, *291*, 31-39.

(103) Hou, Y. W.; Bardo, A. M.; Martinez, C.; Higgins, D. A. Characterization of molecular scale environments in polymer films by single molecule spectroscopy. *Journal of Physical Chemistry B* **2000**, *104*, 106601.

(104) Bardo, A. M.; Collinson, M. M.; Higgins, D. A. Nanoscale properties and matrix-dopant interactions in dye-doped organically modified silicate thin films (vol 13, pg 2713, 2001). *Chemistry of Materials* **2001**, *13*, 3058-3058.

(105) Dutta, A. K.; Kamada, K.; Ohta, K. Spectroscopic studies of nile red in organic solvents and polymers. *Journal of Photochemistry and Photobiology a-Chemistry* **1996**, *93*, 57-64.

(106) Dutta, A. K.; Kamada, K.; Ohta, K. Langmuir-Blodgett films of nile red: A steady-state

and time-resolved fluorescence study. *Chemical Physics Letters* **1996**, *258*, 369-375.

(107) Jose, J.; Burgess, K. Benzophenoxazine-based fluorescent dyes for labeling biomolecules. *Tetrahedron* **2006**, *62*, 11021-11037.

(108) CRC Handbook of Chemistry and Physics, 66th ed
Weast, R.C., Ed.;. CRC Press Inc. Boca Raton, FL,, 1985-1986.

(109) Selvin, P. R.; Lougheed, T.; Tonks Hoffman, M.; Park, H.; Balci, H.; Blehm, B. H.; Toprak, E. Fluorescence Imaging with One-Nanometer Accuracy (FIONA). *CSH protocols* **2007**, *2007*, pdb.top27-pdb.top27.

(110) Moerner, W. E. Microscopy beyond the diffraction limit using actively controlled single molecules. *Journal of Microscopy* **2012**, *246*, 213-220.

(111) Thompson, R. E.; Larson, D. R.; Webb, W. W. Precise nanometer localization analysis for individual fluorescent probes. *Biophysical Journal* **2002**, *82*, 2775-2783.

(112) Striova, J.; Higgins, D. A.; Collinson, M. M. Phase separation in class II organically modified silicate films as probed by phase-imaging atomic force microscopy. *Langmuir* **2005**, *21*, 6137-6141.

(113) Goring, G. L. G.; Brennan, J. D. Effect of ormosil and polymer doping on the morphology of separately and co-hydrolyzed silica films formed by a two-step aqueous processing method. *Chemistry of Materials* **2007**, *19*, 5336-5346.

(114) Wetzel, D. L.; Striova, J.; Higgins, D. A.; Collinson, M. M. Synchrotron infrared micro spectroscopy reveals localized heterogeneities in an organically modified silicate film. *Vibrational Spectroscopy* **2004**, *35*, 153-158.

(115) Brinker, C. J.; Frye, G. C.; Hurd, A. J.; Ashley, C. S. Fundamentals of Sol-Gel Dip Coating. *Thin Solid Films* **1991**, *201*, 97-108.

(116) Brinker, C. J.; Hurd, A. J. Fundamentals of Sol-Gel Dip-Coating. *Journal De Physique Iii* **1994**, *4*, 1231-1242.

(117) Flory, P. J.: Principles of Polymer Chemistry. Cornell University Press: Ithaca, NY, 1953.

(118) Walder, R.; Nelson, N.; Schwartz, D. K. Super-resolution surface mapping using the trajectories of molecular probes. *Nature Communications* **2011**, *2*.

(119) Ding, Y.-X.; Streitmatter, S.; Wright, B. E.; Hlady, V. Spatial Variation of the Charge and Sulfur Oxidation State in a Surface Gradient Affects Plasma Protein Adsorption. *Langmuir* **2010**, *26*, 12140-12146.

(120) Mei, Y.; Wu, T.; Xu, C.; Langenbach, K. J.; Elliott, J. T.; Vogt, B. D.; Beers, K. L.; Amis, E. J.; Washburn, N. R. Tuning cell adhesion on gradient poly(2-hydroxyethyl methacrylate)-grafted surfaces. *Langmuir* **2005**, *21*, 12309-12314.

(121) Moussa, S. G.; McIntire, T. M.; Szori, M.; Roeselova, M.; Tobias, D. J.; Grimm, R. L.; Hemminger, J. C.; Finlayson-Pitts, B. J. Experimental and Theoretical Characterization of Adsorbed Water on Self-Assembled Monolayers: Understanding the Interaction of Water with Atmospherically Relevant Surfaces. *Journal of Physical Chemistry A* **2009**, *113*, 2060-2069.

(122) James, M.; Darwish, T. A.; Ciampi, S.; Sylvester, S. O.; Zhang, Z.; Ng, A.; Gooding, J. J.; Hanley, T. L. Nanoscale condensation of water on self-assembled monolayers. *Soft Matter* **2011**, *7*, 5309-5318.

(123) Szori, M.; Tobias, D. J.; Roeselova, M. Microscopic Wetting of Mixed Self-assembled Monolayers: A Molecular Dynamics Study. *Journal of Physical Chemistry B* **2009**, *113*, 4161-4169.

(124) Gil, A.; Colchero, J.; Luna, M.; Gomez-Herrero, J.; Baro, A. M. Adsorption of water on

solid surfaces studied by scanning force microscopy. *Langmuir* **2000**, *16*, 5086-5092.

(125) Asay, D. B.; Kim, S. H. Evolution of the adsorbed water layer structure on silicon oxide at room temperature. *Journal of Physical Chemistry B* **2005**, *109*, 16760-16763.

(126) Tu, A.; Kwag, H. R.; Barnette, A. L.; Kim, S. H. Water Adsorption Isotherms on CH3-, OH-, and COOH-Terminated Organic Surfaces at Ambient Conditions Measured with PM-RAIRS. *Langmuir* **2012**, *28*, 15263-15269.

(127) Wang, Z.; Nania, S. L.; Shaw, S. K. Structure of Aqueous Water Films on Textured -OH-Terminated Self-Assembled Monolayers. *Langmuir* **2015**, *31*, 2382-2389.

(128) James, M.; Ciampi, S.; Darwish, T. A.; Hanley, T. L.; Sylvester, S. O.; Gooding, J. J. Nanoscale Water Condensation on Click-Functionalized Self-Assembled Monolayers. *Langmuir* **2011**, *27*, 10753-10762.

(129) Verdaguer, A.; Weis, C.; Oncins, G.; Ketteler, G.; Bluhm, H.; Salmeron, M. Growth and structure of water on SiO2 films on Si investigated by Kelvin probe microscopy and in situ x-ray spectroscopies. *Langmuir* **2007**, *23*, 9699-9703.

(130) Miranda, P. B.; Xu, L.; Shen, Y. R.; Salmeron, M. Icelike water monolayer adsorbed on mica at room temperature. *Physical Review Letters* **1998**, *81*, 5876-5879.

(131) Ye, S.; Nihonyanagi, S.; Uosaki, K. Sum frequency generation (SFG) study of the pH-dependent water structure on a fused quartz surface modified by an octadecyltrichlorosilane (OTS) monolayer. *Physical Chemistry Chemical Physics* **2001**, *3*, 3463-3469.

(132) Ismail, A. E.; Grest, G. S.; Stevens, M. J. Structure and dynamics of water near the interface with oligo(ethylene oxide) self-assembled monolayers. *Langmuir* **2007**, *23*, 8508-8514.

(133) Yang, A.-C.; Weng, C.-I. Influence of alkanethiol self-assembled monolayers with various tail groups on structural and dynamic properties of water films. *Journal of Chemical Physics* **2008**, *129*.

(134) Goertz, M. P.; Houston, J. E.; Zhu, X. Y. Hydrophilicity and the viscosity of interfacial water. *Langmuir* **2007**, *23*, 5491-5497.

(135) Israelachvili, J. N. Measurement of the Viscosity of Liquids in Very Thin-Films. *Journal of Colloid and Interface Science* **1986**, *110*, 263-271.

(136) Verdaguer, A.; Sacha, G. M.; Bluhm, H.; Salmeron, M. Molecular structure of water at interfaces: Wetting at the nanometer scale. *Chemical Reviews* **2006**, *106*, 1478-1510.

(137) Odelius, M.; Bernasconi, M.; Parrinello, M. Two dimensional ice adsorbed on mica surface. *Physical Review Letters* **1997**, *78*, 2855-2858.

(138) Teschke, O.; Valente Filho, J. F.; de Souza, E. F. Imaging two-dimensional ice-like structures at room temperature. *Chemical Physics Letters* **2010**, *485*, 133-136.

(139) Axelrod, D.; Koppel, D. E.; Schlessinger, J.; Elson, E.; Webb, W. W. Mobility Measurement by Analysis of Fluorescence Photobleaching Recovery Kinetics. *Biophysical Journal* **1976**, *16*, 1055-1069.

(140) Wirth, M. J.; Swinton, D. J. Single-molecule probing of mixed-mode adsorption at a chromatographic interface. *Analytical Chemistry* **1998**, *70*, 5264-5271.

(141) Bag, N.; Wohland, T. Imaging Fluorescence Fluctuation Spectroscopy: New Tools for Quantitative Bioimaging. *Annual Review of Physical Chemistry, Vol 65* **2014**, *65*, 225-248.

(142) Krause, S.; Hartmann, M.; Kahle, I.; Neumann, M.; Heidernaetsch, M.; Spange, S.; von Borczyskowski, C. Optical Tracking of Single Ag Clusters in Nanostructured Water Films. *Journal of Physical Chemistry C* **2013**, *117*, 24822-24829.

(143) Taeuber, D.; Trenkmann, I.; von Borczyskowski, C. Influence of van der Waals Interactions on Morphology and Dynamics in Ultrathin Liquid Films at Silicon Oxide Interfaces. *Langmuir* **2013**, *29*, 3583-3593.

(144) Dickson, R. M.; Norris, D. J.; Tzeng, Y. L.; Moerner, W. E. Three-dimensional imaging of single molecules solvated in pores of poly(acrylamide) gels. *Science* **1996**, *274*, 966-969.

(145) Kirkeminde, A. W.; Torres, T.; Ito, T.; Higgins, D. A. Multiple Diffusion Pathways in Pluronic F127 Mesophases Revealed by Single Molecule Tracking and Fluorescence Correlation Spectroscopy. *Journal of Physical Chemistry B* **2011**, *115*, 12736-12743.

(146) Martin-Brown, S. A.; Fu, Y.; Saroja, G.; Collinson, M. M.; Higgins, D. A. Single-molecule studies of diffusion by oligomer-bound dyes in organically modified sol-gel-derived silicate films. *Analytical Chemistry* **2005**, *77*, 486-494.

(147) Elliott, L. C. C.; Barhoum, M.; Harris, J. M.; Bohn, P. W. Single Molecule Tracking Studies of Lower Critical Solution Temperature Transition Behavior in Poly(N-isopropylacrylamide). *Langmuir* **2011**, *27*, 11037-11043.

(148) Tran-Ba, K.-H.; Finley, J. J.; Higgins, D. A.; Ito, T. Single-Molecule Tracking Studies of Millimeter-Scale Cylindrical Domain Alignment in Polystyrene-Poly(ethylene oxide) Diblock Copolymer Films Induced by Solvent Vapor Penetration. *Journal of Physical Chemistry Letters* **2012**, *3*, 1968-1973.

(149) McCain, K. S.; Hanley, D. C.; Harris, J. M. Single-molecule fluorescence trajectories for investigating molecular transport in thin silica sol-gel films. *Analytical Chemistry* **2003**, *75*, 4351-4359.

(150) Monserud, J. H.; Schwartz, D. K. Effects of Molecular Size and Surface Hydrophobicity on Oligonucleotide Interfacial Dynamics. *Biomacromolecules* **2012**, *13*, 4002-4011.

(151) Skaug, M. J.; Mabry, J. N.; Schwartz, D. K. Single-Molecule Tracking of Polymer Surface Diffusion. *Journal of the American Chemical Society* **2014**, *136*, 1327-1332.

(152) Cooper, J. T.; Peterson, E. M.; Harris, J. M. Fluorescence Imaging of Single-Molecule Retention Trajectories in Reversed-Phase Chromatographic Particles. *Analytical Chemistry* **2013**, *85*, 9363-9370.

(153) Schmidt, T.; Schutz, G. J.; Baumgartner, W.; Gruber, H. J.; Schindler, H. Imaging of single molecule diffusion. *Proceedings of the National Academy of Sciences of the United States of America* **1996**, *93*, 2926-2929.

(154) Balss, K. M.; Coleman, B. D.; Lansford, C. H.; Haasch, R. T.; Bohn, P. W. Active spatiotemporal control of electrochemical reactions by coupling to in-plane potential gradients. *Journal of Physical Chemistry B* **2001**, *105*, 8970-8978.

(155) Zhao, B. A combinatorial approach to study solvent-induced self-assembly of mixed poly(methyl methacrylate)/polystyrene brushes on planar silica substrates: Effect of relative grafting density. *Langmuir* **2004**, *20*, 11748-11755.

(156) Riepl, M.; Ostblom, M.; Lundstrom, I.; Svensson, S. C. T.; van der Gon, A. W. D.; Schaferling, M.; Liedberg, B. Molecular gradients: An efficient approach for optimizing the surface properties of biomaterials and biochips. *Langmuir* **2005**, *21*, 1042-1050.

(157) Everett, T. A.; Twite, A. A.; Xie, A.; Battina, S. K.; Hua, D. H.; Higgins, D. A. Preparation and characterization of nanofibrous perylene-diimide - Polyelectrolyte composite thin films. *Chemistry of Materials* **2006**, *18*, 5937-5943.

(158) Lange, J. J.; Culbertson, C. T.; Higgins, D. A. Single Molecule Studies of Solvent-Dependent Diffusion and Entrapment in Poly(dimethylsiloxane) Thin Films. *Analytical Chemistry* **2008**, *80*, 9726-9734.

(159) Stalder, A. F.; Melchior, T.; Mueller, M.; Sage, D.; Blu, T.; Unser, M. Low-bond axisymmetric drop shape analysis for surface tension and contact angle measurements of sessile drops. *Colloids and Surfaces a-Physicochemical and Engineering Aspects* **2010**, *364*, 72-81.

(160) Rudich, Y.; Benjamin, I.; Naaman, R.; Thomas, E.; Trakhtenberg, S.; Ussyshkin, R. Wetting of hydrophobic organic surfaces and its implications to organic aerosols in the atmosphere. *Journal of Physical Chemistry A* **2000**, *104*, 5238-5245.

(161) Diez-Perez, I.; Luna, M.; Teheran, F.; Ogletree, D. F.; Sanz, F.; Salmeron, M. Interaction of water with self-assembled monolayers of alkylsilanes on mica. *Langmuir* **2004**, *20*, 1284-1290.

(162) Chen, L.; Gu, X.; Fasolka, M. J.; Martin, J. W.; Nguyen, T. Effects of Humidity and Sample Surface Free Energy on AFM Probe-Sample Interactions and Lateral Force Microscopy Image Contrast. *Langmuir* **2009**, *25*, 3494-3503.

(163) Ford, W. E.; Kamat, P. V. Photochemistry of 3,4,9,10-perylenetetracarboxylic dianhydride dyes .3. Singlet and triplet excited-state properties of the bis(2,5-di-tert-butylphenyl)imide derivative. *Journal of Physical Chemistry* **1987**, *91*, 6373-6380.

(164) Zhang, Y.; Zhang, L.; Liu, H.; Sun, D.; Li, X. Synthesis and aggregation properties of a series of dumbbell polyhedral oligosilsesquioxane-perylene diimide triads. *Crystengcomm* **2015**, *17*, 1453-1463.

(165) Saxton, M. J. Single-particle tracking: The distribution of diffusion coefficients. *Biophysical Journal* **1997**, *72*, 1744-1753.

(166) Michalet, X. Mean square displacement analysis of single-particle trajectories with localization error: Brownian motion in an isotropic medium (vol 82, 041914, 2010).

Physical Review E **2011**, *83*.

(167) Saxton, M. J. Lateral diffusion in an archipelago: Chemically limited reactions. *Biophysical Journal* **1998**, *74*, A223-A223.

(168) Savin, T.; Doyle, P. S. Static and dynamic errors in particle tracking microrheology. *Biophysical Journal* **2005**, *88*, 623-638.

(169) Montiel, D.; Cang, H.; Yang, H. Quantitative characterization of changes in dynamical behavior for single-particle tracking studies. *Journal of Physical Chemistry B* **2006**, *110*, 19763-19770.

(170) Bychuk, O. V.; Oshaughnessy, B. Anomalous Surface-Diffusion - a Numerical Study. *Journal of Chemical Physics* **1994**, *101*, 772-780.

(171) Bychuk, O. V.; Oshaughnessy, B. Anomalous Diffusion at Liquid Surfaces. *Physical Review Letters* **1995**, *74*, 1795-1798.

(172) Chechkin, A. V.; Zaid, I. M.; Lomholt, M. A.; Sokolov, I. M.; Metzler, R. Bulk-mediated diffusion on a planar surface: Full solution. *Physical Review E* **2012**, *86*.

(173) Walder, R.; Nelson, N.; Schwartz, D. K. Single Molecule Observations of Desorption-Mediated Diffusion at the Solid-Liquid Interface. *Physical Review Letters* **2011**, *107*.

(174) Levy-Sakin, M.; Ebenstein, Y. Beyond Sequencing: Optical Mapping of DNA in the Age of Nanotechnology and Nanoscopy. *Curr. Opin. Biotechnol.* **2013**, *24*, 690-698.

(175) Herrick, J.; Bensimon, A.: Introduction to Molecular Combing: Genomics, DNA Replication, and Cancer. In *Methods in Molecular Biology, DNA Replication*; Vengrova, S., Dalgaard, J. Z., Eds.; Humana Press: New York, 2009; Vol. 521; pp 71-101.

(176) Caburet, S.; Conti, C.; Bensimon, A. Combing the genome for genomic instability. *Trends in Biotechnology* **2002**, *20*, 344-350.

(177) Herrick, J.; Bensimon, A.: Single molecule analysis of DNA replication. Biochimie, 1999; Vol. 81; pp 859-871.

(178) Kim, J. H.; Dukkipati, V. R.; Pang, S. W.; Larson, R. G. Stretching and immobilization of DNA for studies of protein-DNA interactions at the single-molecule level. *Nanoscale Research Letters* **2007**, *2*, 185-201.

(179) Gueroui, Z.; Place, C.; Freyssingeas, E.; Berge, B. Observation by fluorescence microscopy of transcription on single combed DNA. *Proceedings of the National Academy of Sciences of the United States of America* **2002**, *99*, 6005-6010.

(180) Harada, Y.; Funatsu, T.; Murakami, K.; Nonoyama, Y.; Ishihama, A.; Yanagida, T. Single-molecule imaging of RNA polymerase-DNA interactions in real time. *Biophysical Journal* **1999**, *76*, 709-715.

(181) Smith, S. B.; Cui, Y. J.; Bustamante, C. Overstretching B-DNA: The elastic response of individual double-stranded and single-stranded DNA molecules. *Science* **1996**, *271*, 795-799.

(182) Wang, M. D.; Yin, H.; Landick, R.; Gelles, J.; Block, S. M. Stretching DNA with optical tweezers. *Biophysical Journal* **1997**, *72*, 1335-1346.

(183) Petit, C. A. P.; Carbeck, J. D. Combing of Molecules in Microchannels (COMMIC): A Method for Micropatterning and Orienting Stretched Molecules of DNA on a Surface. *Nano Lett.* **2003**, *3*, 1141-1146.

(184) Namasivayam, V.; Larson, R. G.; Burke, D. T.; Burns, M. A. Electrostretching DNA molecules using polymer-enhanced media within microfabricated devices. *Analytical Chemistry* **2002**, *74*, 3378-3385.

(185) Strick, T. R.; Allemand, J. F.; Bensimon, D.; Bensimon, A.; Croquette, V. The elasticity of

a single supercoiled DNA molecule. *Science* **1996**, *271*, 1835-1837.

(186) Kim, J. H.; Shi, W.-X.; Larson, R. G. Methods of stretching DNA molecules using flow fields. *Langmuir* **2007**, *23*, 755-764.

(187) Chan, T.-F.; Ha, C.; Phong, A.; Cai, D.; Wan, E.; Leung, L.; Kwok, P.-Y.; Xiao, M. A simple DNA stretching method for fluorescence imaging of single DNA molecules. *Nucleic Acids Research* **2006**, *34*.

(188) Bensimon, A.; Simon, A.; Chiffaudel, A.; Croquette, V.; Heslot, F.; Bensimon, D. Alignment and Sensitive Detection of DNA by a Moving Interface. *Science* **1994**, *265*, 2096-2098.

(189) Michalet, X.; Ekong, R.; Fougerousse, F.; Rousseaux, S.; Schurra, C.; Hornigold, N.; vanSlegtenhorst, M.; Wolfe, J.; Povey, S.; Beckmann, J. S.; Bensimon, A. Dynamic molecular combing: Stretching the whole human genome for high-resolution studies. *Science* **1997**, *277*, 1518-1523.

(190) Yokota, H.; Johnson, F.; Lu, H. B.; Robinson, R. M.; Belu, A. M.; Garrison, M. D.; Ratner, B. D.; Trask, B. J.; Miller, D. L. A new method for straightening DNA molecules for optical restriction mapping. *Nucleic Acids Research* **1997**, *25*, 1064-1070.

(191) Otobe, K.; Ohtani, T. Behavior of DNA fibers stretched by precise meniscus motion control. *Report of National Food Research Institute* **2003**, 100-100.

(192) Liu, R.; Wong, S. T.; Lau, P. P. Z.; Tomczak, N. Stretching and Imaging of Single DNA Chains on a Hydrophobic Polymer Surface Made of Amphiphilic Alternating Comb-Copolymer. *Acs Applied Materials & Interfaces* **2014**, *6*, 2479-2485.

(193) Oshige, M.; Yamaguchi, K.; Matsuura, S.-i.; Kurita, H.; Mizuno, A.; Katsura, S. A new

DNA combing method for biochemical analysis. *Analytical Biochemistry* **2010**, *400*, 145-147.

(194) Fasolka, M. J.; Stafford, C. M.; Beers, K. L.: Gradient and Microfluidic Library Approaches to Polymer Interfaces. In *Adv. Polym. Sci.*; R., M. M. A., Webster, D. C., Eds.; Adv. Polym Sci., 2010; Vol. 225; pp 63-105.

(195) Wheeldon, I.; Farhadi, A.; Bick, A. G.; Jabbari, E.; Khademhosseini, A. Nanoscale tissue engineering: spatial control over cell-materials interactions. *Nanotechnology* **2011**, *22*.

(196) Zelzer, M.; Alexander, M. R.; Russell, N. A. Hippocampal cell response to substrates with surface chemistry gradients. *Acta Biomaterialia* **2011**, *7*, 4120-4130.

(197) Ito, Y.; Heydari, M.; Hashimoto, A.; Konno, T.; Hirasawa, A.; Hori, S.; Kurita, K.; Nakajima, A. The movement of a water droplet on a gradient surface prepared by photodegradation. *Langmuir* **2007**, *23*, 1845-1850.

(198) Hong, D.; Cho, W. K.; Kong, B.; Choi, I. S. Water-Collecting Capability of Radial-Wettability Gradient Surfaces Generated by Controlled Surface Reactions. *Langmuir* **2010**, *26*, 15080-15083.

(199) Wu, J.; Mao, Z.; Tan, H.; Han, L.; Ren, T.; Gao, C. Gradient biomaterials and their influences on cell migration. *Interface Focus* **2012**, *2*, 337-355.

(200) Chan, E. Y.; Goncalves, N. M.; Haeusler, R. A.; Hatch, A. J.; Larson, J. W.; Maletta, A. M.; Yantz, G. R.; Carstea, E. D.; Fuchs, M.; Wong, G. G.; Gullans, S. R.; Gilmanshin, R. DNA mapping using microfluidic stretching and single-molecule detection of fluorescent site-specific tags. *Genome Research* **2004**, *14*, 1137-1146.

(201) Benitez, J. J.; Topolancik, J.; Tian, H. C.; Wallin, C. B.; Latulippe, D. R.; Szeto, K.; Murphy, P. J.; Cipriany, B. R.; Levy, S. L.; Soloway, P. D.; Craighead, H. G. Microfluidic

extraction, stretching and analysis of human chromosomal DNA from single cells. *Lab on Chip* **2012**, *12*, 4848-4854.

(202) Xu, H.; Minter, C. J.; Nagasaka, S.; Ito, T.; Higgins, D. A. Elongation, Alignment, and Guided Electrophoretic Migration of ds-DNA in Flow-Aligned Hexagonal F127 Gels. *Journal of Physical Chemistry B* **2014**, *118*, 4151-4159.

(203) Petrie, R. J.; Bailey, T.; Gorman, C. B.; Genzer, J. Fast directed motion of "Fakir" droplets. *Langmuir* **2004**, *20*, 9893-9896.

(204) Gurrieri, S.; Wells, K. S.; Johnson, I. D.; Bustamante, C. Direct Visualization of Individual DNA Molecules by Fluorescence Microscopy: Characterization of the Factors Affecting Signal/Background and Optimization of Imaging Conditions. *Anal. Biochem.* **1997**, *249*, 44-53.

(205) Butt, H.-J.; Roisman, I. V.; Brinkmann, M.; Papadopoulos, P.; Vollmer, D.; Semprebon, C. Characterization of Super Liquid-Repellent Surfaces. *Curr. Opinion Coll. Interf. Sci.* **2014**, *19*, 343-354.

(206) Allemand, J.-F.; Bensimon, D.; Jullien, L.; Bensimon, A.; Croquette, V. pH-Dependent Specific Binding and Combing of DNA. *Biophys. J.* **1997**, *73*, 2064-2070.

(207) Li, H.-W.; Park, H.-Y.; Porter, M. D.; Yeung, E. S. Single DNA Molecules as Probes of Chromatographic Surfaces. *Anal. Chem.* **2005**, *77*, 3256-3260.

(208) Schmatko, T.; Bozorgui, B.; Geerts, N.; Frenkel, D.; Eiser, E.; Poon, W. C. K. A Finite-Cluster Phase in Lambda-DNA-Coated Colloids. *Soft Matter* **2007**, *3*, 703-706.

(209) Bensimon, D.; Simon, A. J.; Croquette, C.; Bensimon, A. Stretching DNA with a Receding Meniscus: Experiments and Models. *Phys. Rev. Lett.* **1995**, *74*, 4754-4757.

(210) Cluzel, P.; Lebrun, A.; Heller, C.; Lavery, R.; Viovy, J.-L.; Chatenay, D.; Caron, F. DNA: An Extensible Molecule. *Science* **1996**, *271*, 792-794.

(211) Tran Ba, K. H.; Everett, T. A.; Ito, T.; Higgins, D. A. Trajectory angle determination in one dimensional single molecule tracking data by orthogonal regression analysis. *Phys. Chem. Chem. Phys.* **2011**, *13*, 1827-1835.

(212) Hagen, N.; Dereniak, E. L. Gaussian profile estimation in two dimensions. *Appl. Opt.* **2008**, *47*, 6842-6851.

Appendix

1. Error Analysis for Single Molecule Emission Ratio Data.

The individual fluorescent spots produced by single molecule emission are fit to Gaussian intensity profiles to determine the location of each molecule, the spot width, and its peak emission. The fits yield the signal amplitude for each spot and these values are used directly as I_{640} and I_{590} to calculate the emission ratio, E, and the Clausius-Mossotti (CM) factor. The width of the spot is obtained as the standard deviation and is designated as ω, below. Accounting for shot noise in the photon signal and in the background, b, the variance in the fitted amplitude, δ_I^2, can be estimated for each channel as follows-[212]

$$\delta_I^2 \approx \frac{2(I+b)}{\pi\omega^2} \tag{A1}$$

Assuming the noise in the 640 nm and 590 nm channels is uncorrelated, the variance in E value is then estimated as-

$$\delta_E^2 = \frac{4}{\left(I_{640}+I_{590}\right)^4}\left(I_{590}^2\delta_{I_{640}}^2 + I_{640}^2\delta_{I_{590}}^2\right) \tag{A2}$$

The average background, b, was estimated to be 144 counts. The spot width, ω, is ~ 1.2 pixels. Given the above values, the standard deviation in E is estimated to be $\delta_E \sim 0.073$, for

nominal peak signals, I_{640} and I_{590}, of ~100 counts each. Error estimates reported in the manuscript were determined from the experimental data in each case.

2. Finite Difference Time Domain Simulations of Vapor Diffusion Front.

The vapor diffusion front during VPD was simulated by numerically solving Fick's Second Law in two dimensions. The model for the deposition chamber included a 25.4 mm long rectangular reservoir. The simulation cells were 0.254 mm X 0.254 mm in size. The time step employed was 0.01 s and the diffusion coefficient of the precursor silane was estimated to be ~ 0.025 cm^2/s. Periodic boundary conditions were employed at the substrate end (top edge in **Figure 7.7B**, **Chapter 7**), while the vapor concentration was set to zero on the other three sides of the region. The simulation was run out to a time of 60 s. The log of the concentration (arbitrary) units was obtained and is plotted in **Figure 7.7B**.

3. Estimation of Droplet Radius and Expected DNA Orientation.

The radius of the circular contact line for a hemispherical water droplet on the gradient surface was estimated by modeling the droplet as a spherical cap derived from a sphere of radius, *R*, as defined in **equation A3**.

$$R = \left(\frac{3V_{cap}}{\pi(2-3cos\alpha+cos^3\alpha)}\right)^{1/3} \quad \text{(A3)}$$

Here, V_{cap} is the volume of water placed on the surface, and α is the measured water contact angle. For a 2 μL droplet and a contact angle of 70°, *R* = 0.57 mm. The radius, *r*, of the circular contact line on the surface is then obtained by simple trigonometry-

$$r = R\sin\alpha \tag{A4}$$

For the above conditions, $r \sim 0.54$ mm. Finally, the expected orientation, θ, of the DNA (a line perpendicular to the droplet-surface contact line), measured relative to the direction of droplet motion, is determined from **equation A5**.

$$\theta = a\sin\left(\frac{d}{r}\right) \tag{A5}$$

where d is the distance from the droplet centerline. At distances of ± 0.2 mm and ± 0.4 mm, θ = ± 21.7^o and ± 47.8^o, respectively.